1-1-2012

Fresh/Mechanical/Durability Properties and Structural Performance of Enginnered Cementitious Composite (ECC)

Maulin Bipinchandra Mavani
Ryerson University

FRESH/MECHANICAL/DURABILITY PROPERTIES AND STRUCTURAL PERFORMANCE OF ENGINNERED CEMENTITIOUS COMPOSITE (ECC)

By

Maulin Bipinchandra Mavani

B.E. in Civil Engineering, Gujarat University, India, 2005

A thesis

presented to Ryerson University

in partial fulfillment of the

requirements for the degree of

Master of Applied Science

in the program of

Civil Engineering.

Toronto, Ontario, Canada, 2012

AUTHOR'S DECLARATION

I hereby declare that I am the sole author of this thesis. This is a true copy of the thesis, including any required final revisions, as accepted by my examiners.

I authorize Ryerson University to lend this thesis to other institutions or individuals for the purpose of scholarly research

I further authorize Ryerson University to reproduce this thesis by photocopying or by other means, in total or in part, at the request of other institutions or individuals for the purpose of scholarly research.

I understand that my thesis may be made electronically available to the public.

FRESH/MECHANICAL/DURABILITY PROPERTIES AND STRUCTURAL PERFORMANCE OF ENGINEERED CEMENTITIOUS COMPOSITE (ECC)

Maulin Bipinchandra Mavani

2012, MASc., Department of Civil Engineering, Ryerson University

ABSTRACT

Engineered Cementitious Composite (ECC) is an ultra ductile concrete with strain-hardening and multiple-cracking behaviour in tension and flexure. Fresh, mechanical and durability properties of different ECC mixtures are evaluated by incorporating supplementary cementitious materials (class F, CI fly ash and slag) and different aggregate type. Experimental studies demonstrated viability of producing greener, sustainable and cost-effective ECC using locally available aggregates (crushed sand) instead of microsilica sand and fly ash (Class CI or F) of up to 70% cement replacement having similar or better fresh, mechanical and durability properties. Structural validation by small scale tests on bridge decks with ECC link slab and by push out tests to evaluate stud shear connector-ECC interaction compared with self-consolidating concrete (SCC) proved feasibility and advantages of these ECC mixes. Based on research, recommendations are made for ECC mix design and their application in link slab construction in bridge structures.

ACKNOWLEDGEMENTS

I would like to express my deepest gratitude to my supervisors Dr. Mohamed Lachemi and Dr. Khandaker M. Anwar Hossain for their guidance, support and patience during the development of this thesis.

I would like to thank Dr. Hossain for his willingness to always help along with patience, kind words, inspiration and belief in me, which pulled me through this thesis. His countless proof readings, corrections and support made this document possible.

This research investigation was funded by the Ministry of Transportation of Ontario Highway Infrastructure Innovations Funding Program. Their collaboration and financial support are highly appreciated. I would like to thank Hanna Schell, David Rhead and Clifford Lam from the Ministry of Transportation of Ontario,

Thanks and appreciations to industrial partners for their guidance, support and in-kind donations throughout the duration of this research investigation. I would like to specially thank Lafarge Canada and St. Mary's Cement for their support

This research work was conducted at the Concrete Materials Laboratory, Non-destructive Testing Laboratory and Structural Laboratory at Ryerson University. I would like to thank Dr. Ozbay Erdogan, Mohammed Aldardari, Min Yao and Nidal Jaalouk for their assistance and support in conducting lab experiments.

DEDICATIONS

To my wife Jainy and my son Dev

And

To those who support me towards success

TABLE OF CONTENTS

LIST OF TABLES

LIST OF FIGURES

LIST OF NOTATIONS

A	Aggregate
A/B	Aggregate to binder ratio
A_{bar}	Cross sectional area of the selected reinforcing steel bar
A_{sc}	Cross-sectional area of a stud shear connector
ASR	Alkali silica reaction
B	Binder
C	Portland cement
c	Distance from the tensile face of the slab to the centroid of the reinforcing steel
C_{ECC}	Compressive force in the ECC slab per meter
CSH	Calcium silica hydrate
CW	Microcracks width
d	Distance from the neutral axis to the centroid of reinforcing steel
E_c	Elastic modulus of concrete
ECC	Engineered cementitious composites
E_{ECC}	Elastic modulus of ECC
E_m	Elastic modulus of the mortar matrix
ESEM	Environmental scanning electron microscope
ε_u	Uniaxial tensile strain capacity
$\varepsilon_{y\text{-}ECC}$	Yield strain of the elastic-plastic ECC
$\varepsilon_{y\text{-}steel}$	Yield strain of the reinforcing steel.
f'_c	Specified 28-day compressive strength of concrete
FA	Fly ash
FRC	Fiber reinforced concrete
F_u	Ultimate tensile strength of a stud shear connector
$f_{y\text{-}steel}$	Yield strength of the steel
$G_{1\text{-}2}$	Length of any gap between the girders of the two adjacent spans
HPFRCC	High performance fiber reinforced cement concrete
HRWRA	High range water reducing admixture
HVFA	High volume fly ash
I_{ls}	The uncracked moment of inertia
J'_b	Complimentary energy
J_{tip}	Fracture energy of the mortar matrix
K_m	Fracture toughness of the mortar matrix
L_1, L_2	Span lengths of the two adjacent bridge spans
L_{dz}	Length of the link slab debond zone

L_f	Fiber length
L_{ls}	Overall length of the link slab
LVDT	Linear variable displacement transducer
MAS	Maximum aggregate size
M_{ls}	Moment developed in the uncracked concrete link slab
$M_{r\text{-}ls}$	Moment resistance
n_ε	Yield strain ratio
PVA	Poly-vinyl-alcohol
Q_m	Measured strength per stud
Q_n	Computed strength per stud
R/C	Reinforced concrete
R/ECC	Reinforced ECC
RH	Relative humidity
S	Spacing between the bars
Sc	Slip capacity (average slip at peak load)
SCC	Self consolidating concrete
SEM	Scanning electron microscopy
SL	Slag
$T_{ECC\text{-}1}$, $T_{ECC\text{-}2}$	Tension forces in the ECC per meter width of bridge deck
t_s	Deck slab thickness
T_{steel}	Tension force in the reinforcing steel per meter width of bridge deck
UHPC	Ultra high performance concrete
V_f	Fiber volume fraction
w/b	Water to binder ratio
w/c	Water to cement ratio
w_c	Crack width at peak load
δ_0	Crack opening
θ_{max}	Maximum end rotation angle of the adjacent spans
ρ	Steel reinforcement ratio
σ_0	Maximum crack bridging stress
σ_{fc}	First cracking strength of the mortar matrix

CHAPTER ONE

INTRODUCTION

1.1 General

The structural performance is greatly influenced by the materials used and that is the reason why the performance-based design concept is getting more and more attention and gradually replacing the conventional prescriptive approach (SEAOC, 1995). The performance-based design concept allows for greater flexibility, e.g. in dimensioning and reinforcing detailing by structural engineers. It also allows for a larger degree of freedom in construction material choice. Therefore, high performance civil engineering materials with added functions beyond their basic properties are highly desirable.

Concrete has been the predominant construction material during the last century due to low cost and wide availability of raw ingredients along with other advantages (e.g. the ability to be cast and satisfied compressive strength). In fact, concrete is the most used man-made material on the planet. As of 2006, about seven and a half billion cubic meters of concrete are made each year, which is more than one cubic meter for every person on Earth (Wikipedia, 2007). Concrete is a composite material in which aggregates (e.g. gravel and sand) are embedded in a binding medium (e.g. cement or binder) that fills the space between the aggregate particles and glues them together.

One major weakness of concrete is the brittle fracture behaviour in tension, with low tensile strength and ductility. This brittleness has been recognized as a bottleneck hindering structural performances in terms of safety, durability and sustainability. The lack of structural ductility is due to brittle nature of concrete in tension which may lead to loss of structural integrity. Many infrastructure deterioration problems and failures can be traced back to the cracking and brittle nature of concrete. Many attempts have been made in the recent years to overcome these problems.

To effectively solve these severe problems, a new type of composite, called as Engineered Cementitious Composites (ECC), reducing the brittle behaviour of concrete has been developed in recent decades. ECC with its flexible processing has emerged from laboratory testing to field

applications leading to speedy construction, reduced maintenance and a longer life span for the structures (Li and Kanda, 1998; Wang and Li, 2006; Sahmaran et al., 2009). Micromechanical design allows optimization of ECC for high performance, resulting in extreme tensile strain capacity while minimizing the amount of reinforcing fibers, typically less than 2% by volume. Tensile strain capacity exceeding 5% has been demonstrated on ECC reinforced with polyethylene and polyvinyl alcohol fibres (Li, 2003; Li et al., 2002). Unlike ordinary cement-based materials, ECC strain hardens after first cracking, similar to a ductile metal, and demonstrates a strain capacity 300 to 500 times greater than normal concrete. Even at large imposed deformation, crack widths of ECC remain small, less than 60 μm. With intrinsically tight crack width and high tensile ductility, ECC represents a new generation of high-performance concrete material that offers significant potential to naturally resolving the durability problem of reinforced concrete structures (Li and Kanda, 1998; Wang and Li, 2006; Sahmaran et al., 2009; Li, 2003; Li et al., 2002).

ECC, as a special type of high performance fiber-reinforced cementitious composite, features high ductility and damage tolerance under mechanical loading, including tensile and shear (Li, 1997; Li et al., 2001; Li, 2003). By employing micromechanics-based material optimization, tensile strain capacity in excess of 3% under uniaxial tensile loading can be attained with only 2% fiber content by volume (Li, 1997; Lin et al., 1999). The characteristic strain-hardening after matrix first cracking is accompanied by sequential development of multiple micro-cracking and the tensile strain capacity is 300-500 times greater than that of normal concrete. Even at ultimate load, the crack width remains on the order of 50 to 80 μm. This tight crack width is self-controlled and, whether the composite is used in combination with conventional reinforcement or not, it is a material characteristic independent of rebar reinforcement ratio. In contrast, normal concrete and fiber-reinforced concrete rely on steel reinforcement for crack width control. The tight crack width of ECC is important to the durability of ECC structures as the tensile ductility is to the structural safety at ultimate limit state. These properties, together with a relative ease of production including self-consolidation casting (Kong et al., 2003a; Kong et al., 2003b) and shotcreting (Kim et al., 2003), make them suitable for various civil engineering applications. As a result of this, ECC is currently emerging in full scale structural applications (Li et al., 2005; Kunieda and Rokugo, 2006). The ingredients and mix proportions of ECC are optimized through micromechanics-based material design theory to satisfy strength and energy criteria to attain high

composite tensile ductility (Li, 1997; Li et al., 2001; Li, 2003; Yang and Li, 2006). The type, size and amount of fiber, matrix ingredients and interface characteristics are tailored for multiple cracking and controlled crack width in ECCs.

In the past few decades, substitution of mineral admixtures, such as fly ash (FA) and slag (SL), has been of great interest and gradually applied to practical applications of ECC (Kim et al., 2004; Kim et al., 2007; Wang and Li, 2007; Yang et al., 2007; Zhou et al., 2009). FA is a by-product of the coal power plant, whereas slag is a by-product in the manufacture of pig iron. Both of these waste materials from industrial processes are usually available in abundance and at a fraction of the price of cement. The absence of coarse aggregate in ECC results in a higher cement content. Partial replacement of cement using FA or SL reduces the environmental burden. Further, it has been found that incorporating high amount of FA can reduce the matrix toughness and improve the robustness of ECC in terms of tensile ductility. Additionally, unhydrated FA particles with small particle size and smooth spherical shape serve as filler particles resulting in higher compactness of the fiber/matrix interface transition zone that leads to a higher frictional bonding. This aids in reducing the steady-state crack width beneficial for long-term durability of the structure (Lepech and Li, 2005a; Lepech and Li, 2005b; Wang and Li, 2007; Yang et al., 2007). Since the increase in aggregate size and amount leads to an increase in the matrix toughness, locally available aggregate could successfully be used in conjunction with high volume mineral admixture in the production of ECC.

1.2 Statement of Problem

Rehabilitation of bridge structures damaged by continuous wear, as well as time-dependent and environmental effects is a major concern for a large number of reinforced concrete and prestressed concrete bridge structures. Every year, in North America, billions of dollars are spent to repair and maintain bridges. As bridge structures ages, cost of repairs and maintenance magnifies. The poor durability of concrete bridges throughout Canada is an increasingly large concern for highway transportation authorities. With decreasing budget allocations for infrastructure maintenance, rehabilitation, and replacement, the need for greater durability is apparent. The leaking expansion joints are a major source of deterioration of multi-span bridges in Canada. Expansion joints can be replaced by flexible link slabs (Figure 1.1) made with ECC

forming a jointless multi-span bridge and hence, solving the problem of premature deterioration (Caner and Zia, 1998; Kim et al., 2004; Alampalli and Yannotti, 1998).

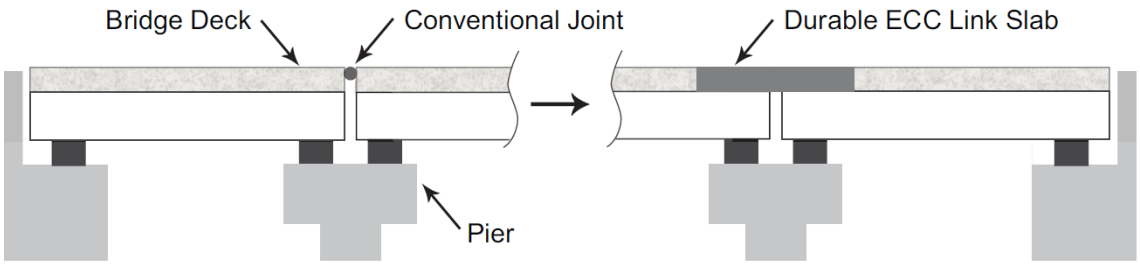

Figure 1.1 Mechanical joint and link slab

The use of ECC and its application to link slab in bridge construction is an emerging technology and until recently, very limited research has been conducted (Caner and Zia, 1998; Kim et al., 2004; Alampalli and Yannotti, 1998). These research studies showed significant enhancement of ductility and crack width control in ECC link slabs confirming that the use of ECC can be effective in extending the service life of bridge deck systems.

Currently, there are many publications available that largely address the ECC mixtures and their properties in fresh and hardened state. However, the lack of published research related to the structural performance of ECC may deter engineers from using ECC in the real structural application. Thus, even though authorities are willing to use the ECC particularly for the link slab application, they are sometimes hesitant because of the apparent lack of supporting data. Moreover, typical ECC mix design involves the use of microsilica sand as an aggregate type which increases the cost of ECC to a large extent and there is a little research done on optimization of ECC mixtures using locally available aggregate type. There is a need for detailed studies on the evaluation and optimization of ECC which is cost effective, greener and sustainable and specifically tailored for the link slab application of bridge structures.

1.3 Objectives

The experimental research program is focussed on achieving more environmental friendly ECC with moderately high compressive strength, high dimensional stability, improved elastic modulus and superior ductility represented by strain-hardening behaviour. The research is conducted to:

- develop and optimize green ECC mixtures containing SCM (Class CI FA, class F FA or SL) with SCM/cement ratio of 1.2 or 2.2, fine aggregate (microsilica sand or crushed sand) with maximum sizes of 0.4 or 1.19 mm and aggregate/binder ratio of 0.36 based on slump flow, flow time, initial and final setting time, heat of hydration, compressive strength, flexural strength, drying shrinkage, rapid chloride ion penetration test, water absorption, water porosity, sorptivity, rapid freeze-thaw resistance and corrosion resistance of steel in concrete. Within the objective of this experimental study, ten ECC mixtures were prepared (six mixtures with microsilica sand and four with crushed sand) keeping the water-to-binder ratio in the range of 0.27 to 0.30.

- study the influence of mix design parameters and materials (such as the use of FA of different types, slag as SCMs and the use local crushed sand as replacement of silica sand) on ECC properties to obtain best mixtures with better strength, ductility and durability.

- evaluate the structural performance of ECC in practical construction specifically to the bridge deck link slab by testing small scale bridge deck specimens. Simultaneously, evaluate the interaction of ECC with stud shear connectors used in bridge decks by conducting push out tests generating load slip curves.

- compare the structural performance of ECC link slabs and push out specimens with those of normal self-consolidating concrete (SCC) counterparts.

- make recommendations for mix design of best ECC mixtures for structural applications especially for the construction of ECC link slab in bridge construction.

1.4 Thesis Outline

Chapter 1 describes the objectives and the scope of the research with brief introduction to the research topics.

In Chapter 2, a literature review on ECC is presented. This includes the use pozzolanic materials such as fly ash and ground granulated blast furnace slag in ECC, ECC hardened and durability properties, application of ECC and introduction to link slab construction with structural design.

Chapter 3 describes the experimental program including material properties and test setup/procedures for fresh, mechanical and durability properties of ECC.

Chapter 4 provides the results of the experimental studies for fresh and mechanical properties and detailed discussions.

Chapter 5 presents the results and discussion of the ECC durability properties.

The structural performance of ECC links slabs compared with SCC counterparts is presented in Chapter 6. The development of experimental setups and specimens for link slab and pushout tests, test procedures and test results are described.

Chapter 7 presents the summary and conclusion of the present study. It also outlines possible implementations and recommendations for further research on ECC.

CHAPTER TWO

LITERATURE REVIEW

2.1 Introduction

The enhanced durability of reinforced concrete structures is typically associated with a dense concrete matrix. A compact microstructure results in lower permeability and reduce transport of corrosives to steel reinforcing (Beeldens and Vandewalle, 2001; Oh et al., 2002). This can be achieved with the use of aggregates with a well-graded particle size distribution (Hwang et al., 1996), slag, fly ash and silica fume (Chang et al., 2001), or low w/c ratios (Mehta, 1986). These concepts, however, rely upon the concrete to remain uncracked within a structure throughout its expected lifetime and resist the transport of water, chloride ions, oxygen, etc. through its dense microstructure. In this presumed uncracked state, numerous concrete materials have shown promising durability in laboratory tests (Weiss and Shah, 2002; Mora et al., 2003).

In practice, however, reinforced concrete members crack due to both applied structural loading and shrinkage and thermal deformations, which are practically inevitable and often anticipated in restrained conditions (Wittmann, 2002; Mihashi and De Leite, 2004). These cracks provide pathways for the penetration of aggressive ions to cause concrete deterioration. Chlorides, oxygen, and carbonation agents can migrate through cracks and ultimately lead to corrosion of reinforcement. Although the uncracked concrete between adjacent cracks can be extremely dense and nearly impermeable, the presence of cracks results in a high overall permeability and unhindered access of corrosives (Bakker, 1988; Gerard et al., 1997 ; Hearn, 1999) to reinforcing steels through the concrete cover. Thus, at the root of this durability problem is the brittle nature of concrete materials. To solve this serious problem, a fundamental solution which reduces the brittle nature of concrete is needed.

Through the use of High Performance Fiber Reinforced Cementitious Composite (HPFRCC), which displays significantly higher ductility than traditional concrete, durability problems resulting from cracking may be solved (Li and Stang, 2004). The use of fibers in the concrete is not a new technology. The early use of fibers to reinforce a brittle material can be traced back to Egyptian times when straws or horsehair were added to mud bricks. Straw mats serving as

reinforcements were also found in early Chinese and Japanese housing construction. Yet to prove acceptable for many applications, HPFRCC must show high ductility without forming large cracks and enhanced material and structural durability by exhibiting such characteristics as excellent protection of steel reinforcement, resistance to freeze thaw cycles, de-icing salt scaling resistance and demonstration of long term mechanical performance. The introduction of materials which provide both ductility and durability can significantly impact the design of future, more durable infrastructure systems.

2.2 Engineered Cementitious Composites (ECC)

2.2.1 Introduction and Mix Design of ECC

Engineered Cementitious Composite (ECC), as a new class of HPFRCC materials, is a ductile fiber reinforced cementitious composite micromechanically designed to achieve high damage tolerance under severe loading and high durability under normal service conditions (Li, 1998; Li et al., 2001; Li, 2003). The most distinctive characteristic separating ECC from conventional concrete and fiber reinforced concrete (FRC) is an ultimate tensile strain capacity in the range of 3% to 5%, depending on the specific ECC mixture. This strain capacity is realized through the formation of many closely spaced microcracks, allowing for a strain capacity over 300 times that of normal concrete. These cracks, which carry increasing load after formation, allow the material to exhibit strain hardening, similar to many ductile metals. While the components of ECC may be similar to FRC, the distinctive ECC characteristic of strain hardening through micro-cracking is achieved through micromechanical tailoring of the components (i.e. cement, aggregate, and fibers) (Li, 1998; Lin et al., 1999; Li et al., 2001; Li, 2003), along with control of the interfacial properties between components. Fracture properties of the cementitious matrix are carefully controlled through mix proportions. Fiber properties, such as strength, modulus of elasticity, and aspect ratio have been customized for use in ECC. The interfacial properties between fiber and matrix have also been optimized in cooperation with the manufacturer for use in this material. Typical mix proportions of ECC using a polyvinyl-alcohol (PVA) fiber are given in Table 2.1.

Table 2.1 Typical mix design of ECC material (Li, 2003)

Cement	Water	Aggregate	Fly Ash	HRWR*	Fiber (%)
1.00	0.58	0.8	1.2	0.013	2.00

*HRWRA = High range water reducing admixture; all ingredients proportion by weight except for fiber

While most HPFRCCs rely on a high fiber volume to achieve high performance, ECC uses low amounts, typically 2% by volume, of short, discontinuous fiber. This low fiber volume, along with the common components allows flexibility in construction execution. To date, ECC materials have been engineered for self-consolidation casting (Kong et al., 2003a), extrusion (Stang, 1999), shotcreting (Kim et al., 2003), and conventional mixing in a gravity mixer or conventional mixing truck (Lepech and Li, 2008)

2.2.2 ECC Mixtures

ECC utilize similar ingredients as FRC. Generally, the materials used in standard ECC are cement, fine aggregate, water, fibers and some common chemical additives to attain desired workability. Discussion of each of these materials has been discussed below.

2.2.2.1 Cement

ECC can be produced using ordinary Portland cement. Compared with conventional concrete, ECC materials contain considerably higher cement content; typically two to three times higher than conventional structural concrete (Wang and Li, 2007b). Table 2.1 shows the mixture proportions of typical (high modulus) PVA-ECC. The high cement content in ECCs is a consequence of rheology control for easy fiber dispersion and, more essentially matrix toughness control for strain-hardening behaviour.

2.2.2.2 Aggregates

Aggregates typically occupy an important volume fraction in conventional concrete, and thus have important effects on different aspects of material properties. In addition to their role as economic filler, aggregates help to control dimensional stability of cement-based materials, which may be considered to consist of a framework of cement paste with relatively large shrinkage movements restrained by aggregates. Moreover, the introduction of aggregates with a particle size larger than the average fiber spacing leads to balling and greater interaction of fibers between the large aggregate particles, and the effect becomes more pronounced as the volume and the maximum size of aggregate particles increase. Therefore, an increase in aggregate size makes it more difficult to achieve a uniform dispersion of fibers. The greater the volume and size of aggregates, the more clumping and interaction of fibers would occur. Therefore, the amount and size of the aggregates is expected to have a significant influence on the properties of

composite. Hence, in spite of positive effects of aggregates on dimensional stability and economy of fiber reinforced cement composites, there are limits on aggregate size and volume content beyond which problems with fiber dispersability, fresh mix workability and matrix toughness may start to damage the composite material performance characteristics. Therefore, instead of coarse aggregate, standard ECC incorporates fine aggregate (microsilica sand) with an aggregate to binder ratio (A/B) of 0.36 to maintain adequate stiffness and volume stability (Li et al., 1995). The binder system is defined as the total amount of cementitious material, i.e. cement and mineral admixture, generally fly ash, in ECC. The microsilica sand has a maximum grain size of 250 μm and a mean size of 110 μm. Another purpose of using fine silica sand is to obtain the optimum gradation of particles to produce good workability (Fischer and Li, 2003).

2.2.2.3 Fibers

Unlike some high performance FRC, ECC does not utilize large amounts of fiber. In general 2% or less by volume of discontinuous fiber is adequate, even though the composite is designed for structural applications. Because of the relatively small amount of fibers, and its chopped nature, the mixing process of ECC is similar to those employed in mixing normal concrete. Also by deliberately limiting the amount of fibers, a number of proprietary studies have concluded economic feasibility of ECC in specific structural applications. (Li, 2003)

2.2.3 Pozzolanic Materials

In order to achieve strain hardening, matrix fracture toughness has to be limited such that multiple cracking could occur before reaching maximum fiber bridging stress. Large aggregates are hence eliminated in the mixture, resulting in a higher cement content compared with normal concrete. In fact, ECC materials use cement paste or mortar with fine sand as a matrix, and typically have cement content at 830 to 1200 kg/m^3 (Lepech et al., 2008). High cement usage results in undesired high hydration heat as well as high material cost. In addition, such matrixes apparently compromise sustainability performance of the material, as cement production is responsible for 3% of global greenhouse gas emissions generated by human activities, and significant levels of nitrogen oxides, particulate matter, and other pollutants (Lepech et al., 2008). One natural approach to address these issues is to substitute cement with industrial by-products. The pozzolanic material has been proved to be one of the best replacements of cement.

According to ACI 116R-90 (1994), pozzolan is "a siliceous or siliceous and aluminous material, which in itself possesses little or no cementitious value but will, in finely divided form and in the presence of moisture, chemically reacts with calcium hydroxide at ordinary temperatures to form compounds possessing cementitious properties." Some of the most used materials are ground granulated blast furnace slag, fly ash, condensed silica fume, volcanic materials, rice husk ash and metakaolin. When properly used as a portion of the cementitious material, these pozzolanic admixtures can improve the properties of the fresh and hardened concrete (Hossain, 2003; Hossain, 2004; Hossain, 2005; Hossain et al., 2012; Hossain, 2012; Karahan et al., 2012)

Although several types of supplementary cementitious materials exist, the focus of this review will be on the two types used in this study, namely slag and fly ash. A brief overview of the history, properties, and usage of granulated blast furnace slag and fly ash in concrete is presented in Sections 2.2.31 and 2.2.3.2.

2.2.3.1 Slag

Slag has been used as partial replacement for Portland cement in concrete for more than 100 years (Glasser, 1991). As a by-product of the pig iron industry, slag is produced in large quantities in many areas around the world. In the United States, slag is most commonly used as base course for roads and other structures. However, in many other countries, most of the available slag is ground to approximately the same fineness as cement and then utilized as a partial replacement for Portland cement in concrete.

The composition of slag can vary considerably between production facilities. The presence of the major oxides are typically found to be within the following ranges: magnesium oxide (MgO), 0 to 21 %; aluminum oxide (Al2O3), 5 to 33 %; silicon dioxide (SiO2), 27 to 42 %; and calcium oxide (CaO), 30 to 50 % (Taylor, 1997).

Although the composition of slag is important, the method used in its production is perhaps more important as air-cooled slag has very limited, if any, cementing properties (Moranville-Regourd, 1998). However, if the slag is cooled rapidly from its liquid state at 1350-1550°C down to about 800°C, crystallization of the material can be avoided and the resulting product often contains over 95% glass which is a latent hydraulic cement (Taylor, 1997).

For any substantial reaction to occur between slag and water, an activator is required. High alkaline environments have proved to be suitable activators. Fortunately, the pore solution of cement paste is basically composed of alkaline hydroxides and as such, provides for an excellent activator. The use of slag in concrete tends to slow down the rate of hydration at early ages at room temperature. However, elevated temperatures help activate the slag and increase the rate of hydration (Roy, 1992). Therefore, slag can be used in steam-cured concrete. In addition, the damaging effects, such as reduced strength and increased permeability, of high early age temperature on concretes containing slag are less pronounced than when slag is not used (Neville, 1996).

The reaction of a blend of cement and slag results in a higher percentage of calcium silicate-hydrate (C-S-H) and less calcium hydroxide than plain cement (Neville, 1996). This alteration in the hydration products is attributable to the higher silicon content of the cement and slag blend when compared with plain cement. The change in the microstructure and the slower rate of hydration when slag is used typically yields denser and less permeable concretes.

In addition to lower permeability, concretes made with slag tend to have better resistance to chloride ion penetration than normal concretes. The freeze-thaw resistance of concrete made with slag is believed to be adequate and not adversely affected when compared with concrete made without slag (Neville, 1996). However, concretes made with slag generally suffer higher degree of de-icing salt scaling than do reference concretes made without slag (Stark and Ludwig, 1997).

Research work has been conducted on ECC incorporating slag as a replacement of cement provided with evidence that slag can improve the greenness of concrete since production of slag needs less energy and causes less CO_2 emission than portland cement. Moreover, use of BFS improved the properties of fresh and hardened concrete, such as workability and durability. As such, beyond certain level of replacement of cement, slag proved to be decreasing flexural properties of slag. (Kim et al., 2007; Lepech et al., 2008; Ozkan and Mehmet, 2009; Zhou et al., 2009; Karahan et al., 2012)

2.2.3.2 Fly Ash

Fly ash is the most widely used mineral admixture for concrete. It is a by-product of burning pulverized coal, in electric power production. During combustion, most of the volatile matter and carbon is burned off leaving the coal's mineral impurities (clay, feldspar, quartz, and shale) behind which then fuse together while in suspension. The fused particles are carried away by the exhaust by electrostatic precipitators or bag filters. During this process the fused material cools and solidifies to form the spherical fly ash particles. Typical particle size is around 20 microns but may range from one micron up to as large as 100 microns. Surface area may range from 200-700 m^2/kg but typically are between 300-500 m^2/kg (Kosmatka and Panarese, 1988).

Fly ash consists primarily of silica, aluminum, iron, and calcium in a silicate glass form. Minor constituents can be found in the form of magnesium, sulfur, sodium, potassium, and carbon. According to American Society for Testing and Materials (ASTM), there are two classes of fly ash (Table 2.2): Class C, which is normally produced from lignite or sub-bituminous coals and Class F, which is normally produced from bituminous coals (ASTM C618, 2012). Class C fly ashes differ from Class F fly ashes in that they are self-hardening even without the presence of cement.

Table 2.2 Specifications for fly ash (ASTM C618, 2012)

Class of Ash	ASTM Specification
Class C	$SiO_2 + Al_2O_3 + Fe_2O_3 > 50\%$
Class F	$SiO_2 + Al_2O_3 + Fe_2O_3 > 70\%$

Use of fly ash in the production of ECC by some researchers provided with favourable results in terms of improved ductility, micro-cracking behaviour, durability properties and sustainability. (Bisaillon et al., 1994; Hussian and Rasheeduzzafar, 1994; Kuroda et al., 2000; Lepech and Li, 2005b ;Karahan et al., 2012;)

2.2.4 Design of Engineered Cementitious Composites and Micro-mechanical Properties

The first priority when designing ECC material is to ensure the formation of multiple cracks and strain-hardening behaviour under load. This allows large deformations to be distributed over multiple micro-cracks. The basis of multiple micro-cracking and strain hardening within ECC is the propagation of steady state cracks which were first characterized by Marshall and Cox (1988), and extended to fiber reinforced cementitious composites by Li and Leung (1992) and Lin et al. (1999). By forming steady state "flat cracks" which maintain a constant crack width while propagating, rather than Griffith-type cracks which widen during propagation as in typical tension-softening fiber reinforced cementitious materials, ECC material exhibits multiple micro-cracks which saturate the specimen while undergoing strain-hardening during extreme tensile deformation. The formation of multiple steady-state cracking is governed by the bridging stress versus crack width opening relation along with the cracking toughness of the mortar matrix. To achieve this phenomenon the inequality shown in Equation 2.1 must be satisfied:

$$J_b' = \sigma_0\delta_0 - \int_0^{\delta_0} \sigma(\delta)d\delta \geq J_{tip} \approx \frac{K_m^2}{E_m} \qquad (2.1)$$

where J_b' is the complimentary energy shown in Figure 2.1, σ_0 and δ_0 are the maximum crack bridging stress and corresponding crack opening, J_{tip} is the fracture energy of the mortar matrix, K_m is the fracture toughness of the mortar matrix, and E_m is the elastic modulus of the mortar matrix. In addition to the fracture energy criterion, a strength criterion expressed in Equation 2.2 must be satisfied:

$$\sigma_0 > \sigma_{fc} \qquad (2.2)$$

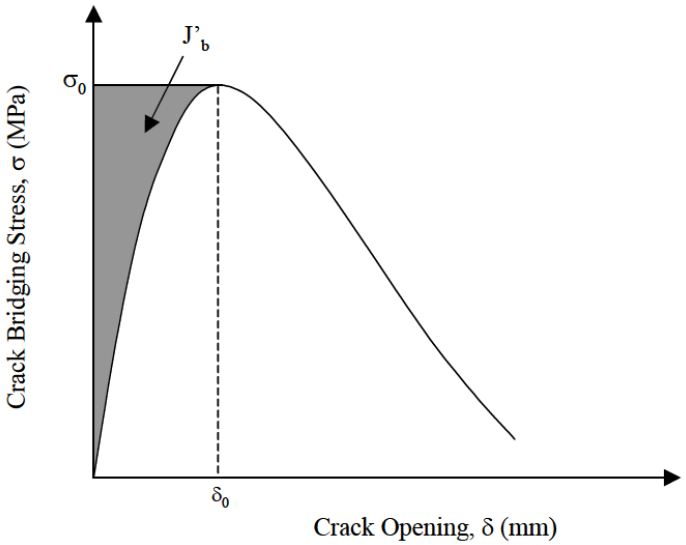

Figure 2.1 Crack bridging stress versus crack opening relation (Li et al., 1992)

Where σ_0 is the maximum crack bridging stress and σ_{fc} is the first cracking strength of the mortar matrix. For saturated multiple cracking, Wang and Li (2004) found that Equation 2.2 must be satisfied at each potential crack plane, where σ_{fc} is understood as the cracking stress on that crack plane.

Once an ECC mixture is selected which sufficiently meets the two above criteria, the formation of multiple steady state cracks, and strain-hardening performance, can be realized. However, in addition to forming these cracks, the material must also be designed to exhibit crack widths below the 100 μm threshold limit (Li et al., 1992). This can be achieved through tailoring of the crack bridging versus crack opening relation referenced in Eq. 2.1. The maximum steady state crack width exhibited during ECC multiple cracking can be assumed to be δ_0, the crack width corresponding to the maximum crack bridging stress σ_0. If the crack width were to grow beyond δ_0, the crack bridging stress would begin to fall, in which case the crack would localize and multiple crack formation would cease. By keeping δ_0 below the 100 μm threshold, the ECC material can exhibit multiple cracking and strain hardening performance.

Using these basic micromechanical models to tailor the ECC material, a composite can be designed to undergo large deformations, up to several percent, without sacrificing low permeability due to large crack widths. The application of material design procedures, such as

those outlined above, allow materials engineers to carefully match material characteristics to specific structural demands, such as strain capacity and low permeability.

2.3 Mechanical and Durability Properties of ECC

2.3.1 Strength, Cracking and Ductility Characteristics

Figure 2.2 shows a typical uniaxial tensile stress-strain curve of ECC material containing 2% poly-vinyl-alcohol (PVA) fiber (Weimann and Li, 2003). As can be seen, the characteristic strain-hardening behaviour after first cracking is accompanied by multiple micro-cracking. The crack width development during inelastic straining is also shown in Figure 2.2. Even at ultimate load, the crack width remains smaller than 80 μm. This tight crack width is self-controlled and, whether the composite is used in combination with conventional reinforcement or not, it is a material characteristic independent of rebar reinforcement ratio. In contrast, normal concrete and fiber reinforced concrete rely on steel reinforcement for crack width control. Under severe bending loads, an ECC beam deforms similar to a ductile metal plate through plastic deformation (Figure 2.3). In compression, ECC materials exhibit compressive strengths similar to high strength concrete (e.g. greater than 60 MPa) (Lepech and Li, 2008).

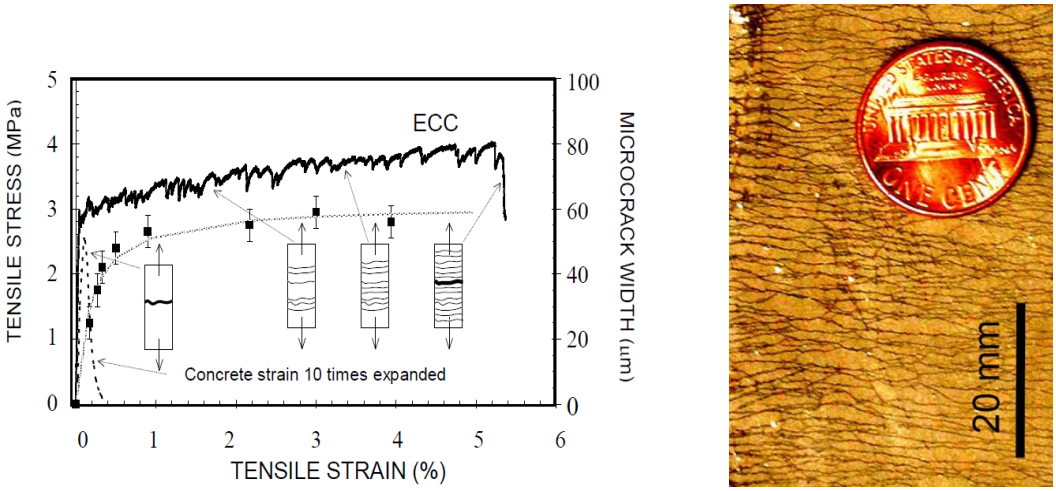

Figure 2.2 Typical tensile stress-strain curve and crack width development of ECC (Weimann and Li, 2003)

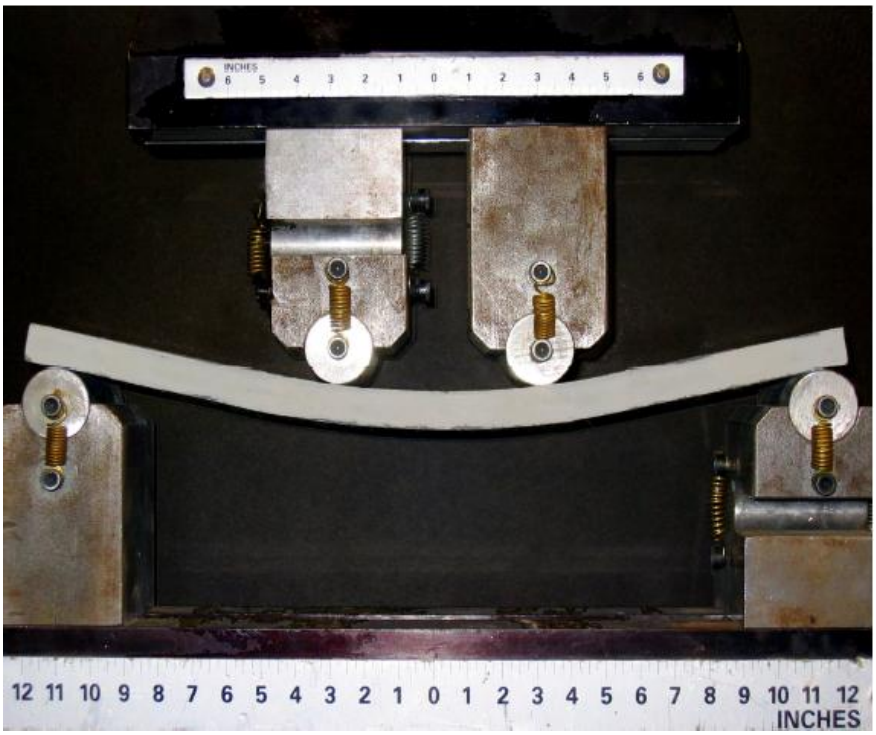

Figure 2.3 Response of ECC under flexural loading (Li, 2003)

2.3.2 Spalling Resistance

Greater resistance to spalling, brought about by reinforcing steel corrosion, can be achieved through the high ductility of ECC material. It is well known that once corrosion of steel reinforcing is initiated, corrosion debris expands against the surrounding concrete, creating a tensile circumferential stress state (i.e. hoop stress) in the cover concrete. This may lead to tensile radial cracking and subsequent spalling of the cover, resulting in a shortening of the structural service life. The spall resistance of ECC was investigated Kanda et al. (2003) and Miyazato and Hiraishi (2005) by pushing a tapered steel rod into a hole cast through an ECC slab in order to simulate the expansive force generated by a corroding rebar. The test results showed that ECC accommodated the simulated expansion by "plastic yielding" through the formation of radial microcracks, while concrete fractured in a brittle nature under the expansive force. Figure 2.4 shows the signature damage and failure modes in ECC and concrete slabs after testing. Even with identical material compressive strengths, a significantly higher load (30 kN) was sustained by the ECC slab as compared to the concrete slab (~7 kN).

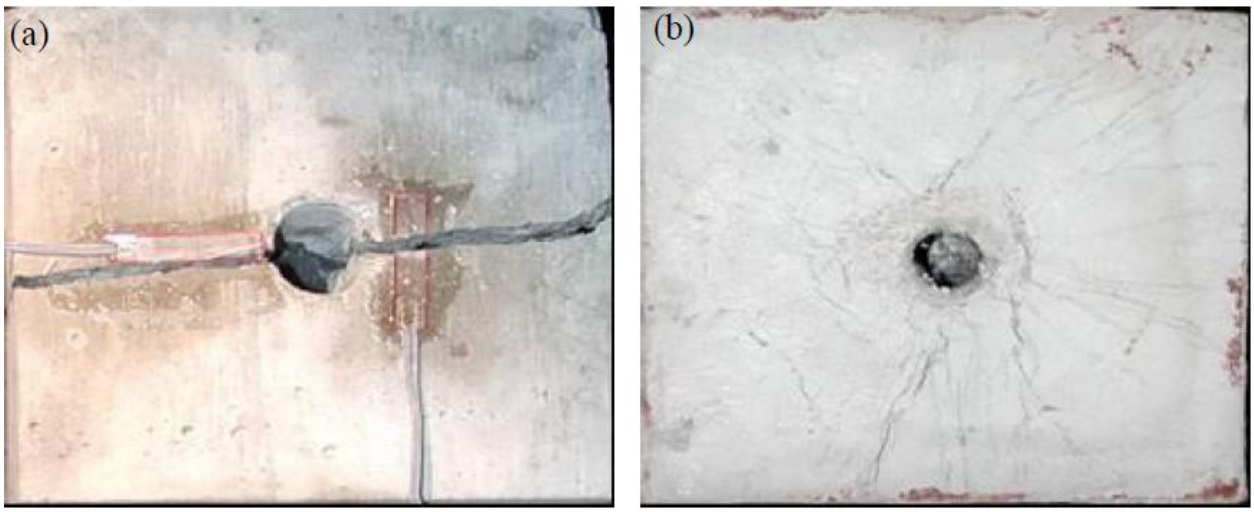

Figure 2.4 Failure modes of the slab (a) concrete, and (b) ECC (Sahmaran and Li, 2010)

2.3.3 Wear Testing and Abrasion

For pavement surface and bridge deck repairs, ECC must provide an adequate surface for driving and braking, while withstanding traffic abrasion (Li et al., 2003). Cured ECC specimens for 28 days and subjected to both static friction testing and wear track testing according to Michigan Test Method 111 (2001). Initial friction forces between vehicle tires operating at 65 kph and the textured ECC specimens were determined using a Michigan Department of Transportation (MDOT) static friction tester. All static friction tests were conducted on a wet pavement surface. Following initial friction testing, ECC specimens were subjected to 4 million tire passes to simulate long term tire wear. After wearing, friction forces were again determined to assess deterioration or surface polishing during wearing. These final friction forces equate to an Aggregate Wear Index (AWI) used for long term evaluation of pavement wear. AWI values for the textured ECC samples tested range from 1.6 kN to 2.3 kN (Li et al., 2003). The established minimum AWI for Michigan truck-line road surfaces is 1.2 kN, significantly lower than all ECC surfaces tested, indicating its suitability for roadway surface repairs subject to heavy traffic volumes.

2.3.4 Transport Properties of ECC

Depending on the driving force, the transportation of liquids, gases and ions through hardened concrete can occur chiefly through three different mechanisms; permeation, absorption, or

diffusion. Depending upon the conditions, transport of liquids, gases and ions may be driven by one or a combination of these three mechanisms. The main driving force behind permeation is the presence of a pressure gradient (Lepech and Li, 2005a; Lepech et al., 2006; Sahmaran and Li, 2008). Permeation is very important for concrete structures under water such as offshore structures or fluid retaining structures such as water tanks. Absorption, driven by capillary pore suction, is the predominant transport process when unsaturated concrete is exposed to liquids. Diffusion is the most commonly studied transport process of ions, such as chloride, which accelerates the initiation of steel corrosion in concrete. When the saturated concrete is exposed to a chloride solution, a chloride concentration gradient is created between the concrete element surface and the pore solution. In this case, diffusion will be the predominant driving mechanism of chloride transport.

2.3.4.1 Permeability

Typically, the formation of cracks increases the transport properties of concrete, allowing water, oxygen and chloride ions to easily penetrate and reach the reinforcing steel and accelerate the initiation of steel corrosion in concrete. Lepech and Li (2005a) studied the water permeability of mechanically loaded ECC and reinforced mortar. In that study, both ECC and reinforced mortar specimens were tensioned to identical 1.5% deformation, resulting in a variety of crack widths and number of cracks among the various specimens. The ECC specimens revealed microcracks less than 60 μm regardless of the imposed deformation level, and the cracked specimens exhibited nearly the same water permeability as sound concrete (Figure 2.5). In contrast, cracks larger than 150 μm were easily produced in the reinforced mortar specimens under the identical imposed uniaxial deformation. The larger crack widths resulted in significant increase in water permeability of the reinforced mortar, despite the smaller number of cracks. Further, when normalized by number of cracks within the specimen, the comparable permeability of cracked ECC with sound material becomes even more apparent (Figure 2.5).

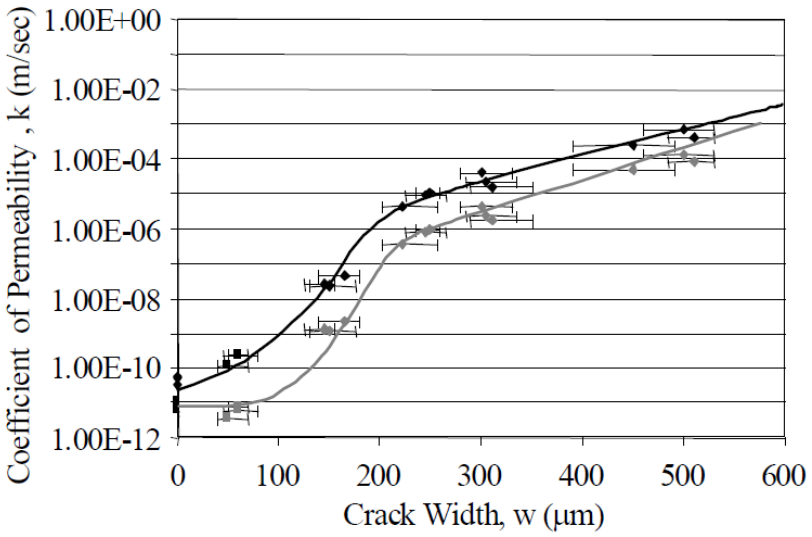

Figure 2.5 Permeability of cracked and uncracked ECC (square symbols) and reinforced mortar specimens (diamond symbols). Grey data points are permeability values normalized by number of cracks in the specimens (Sahmaran and Li, 2009a)

2.3.4.2 Diffusion

The corrosion of steel in concrete is one of the major problems with respect to the durability of reinforced concrete structures, and the penetration of chloride ions into concrete is considered to be the major cause of corrosion. Miyazato and Hiraishi (2005) was probably the first to show that the penetration depth of chloride ions into ECC cover was substantially lower than that in concrete cover, using reinforced concrete (R/C) and reinforced ECC (R/ECC) beams preloaded to the same level of flexural deflection and subjected to identical accelerated chloride exposure. In addition, a relation between flexural deformation levels and the effective chloride diffusion coefficient of ECC and reinforced mortar was examined by Sahmaran et al. (2007). The effective chloride diffusion was computed based on measured chloride ion concentration profiles fitted to Crank's solution to Fick's 2nd Law. Under high imposed bending deformation, the preloaded ECC beam specimens revealed multiple microcracks width less than 50 μm and an effective diffusion coefficient significantly lower than that of the similarly preloaded reinforced mortar beam because of the tight crack width control in ECC (Figure 2.6). In contrast, cracks larger than 150 μm were easily produced in reinforced mortar specimens under the same imposed deformation, producing significant increase in the effective diffusion coefficient. The effective diffusion coefficient of ECC was found to be linearly proportional to the number of cracks, whereas the effective diffusion coefficient of reinforced mortar is proportional to the square of

the crack width. Therefore, the effect of crack width on chloride transport was more pronounced when compared to that of crack number. In addition, tensile performances of ECC cracked and uncracked specimens under marine environment were investigated by Li et al. (2007). Apart from the slight reductions in ultimate tensile strain and strength capacities and higher residual crack width, the test results largely confirm the durability performance of ECC material under accelerated aging, even in cases where the material experiences mechanical loading that deforms it into the strain-hardening stage prior to exposure. Healing of micro-cracks induced by the preload is evident from the recovery of elastic stiffness of the exposed pre-cracked specimens on reloading.

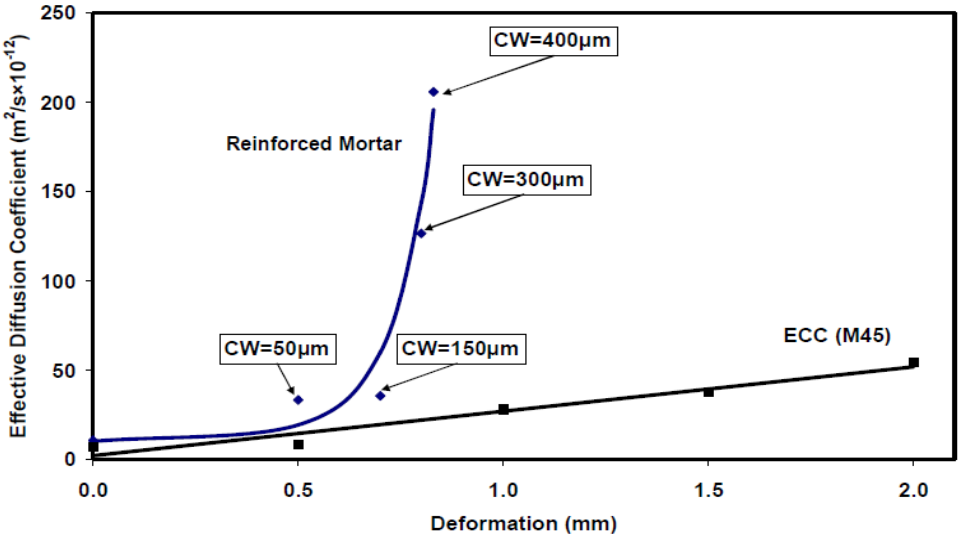

Figure 2.6 Diffusion coefficient versus pre-loading deformation level for ECC and mortar (Sahmaran et al., 2007)

2.3.4.3 Absorption

Since concrete structures in exposed conditions are generally subjected to the drying actions of wind and sun, they are rarely fully saturated when in service. Under this condition, therefore, permeability and diffusion may not be the dominant transport processes in concrete materials. Under dry or partially saturated conditions, the movement of water into concrete is controlled by capillary suction forces existing in the evacuated capillary cavities within the matrix (Martys and Ferraris, 1997). As mentioned above, cracking in ECC is fundamentally different from that which occurs in concrete or reinforced concrete. One of the concerns of ECC is its crack pattern of closely spaced cracks with tight crack width in relation to capillary suction. This concern is

addressed directly in the study conducted by Sahmaran and Li (2009b) by measuring the sorptivity and absorption properties of pre-cracked ECC material. After various numbers of microcracks were introduced by mechanical loading, water absorption and sorptivity tests were performed to develop an understanding of how microcracks accelerated the deterioration process. Figure 2.7 shows the relationship between the sorptivity ($mm/min^{1/2}$) over six hours and the number of cracks, for ECC specimens. Corresponding values for virgin ECC specimens (data points with zero number of cracks) are also included in this plot. As seen from the figure, the presence of micro-cracking in ECC significantly alters the transport properties measured as a function of the number of micro-cracks. The water absorption increase is fairly high as the number of cracks on the surface of the ECC specimens increases. Therefore, the sorptivity test shows that micro-cracked ECC specimens would be more vulnerable to attack than virgin specimens. As the number of cracks along the specimen grows, the sorptivity of ECC increased exponentially. Even so, the sorptivity values of pre-loaded ECC specimens up to a strain representing 1.5% on the exposed tensile face is not particularly high when compared to that of normal concrete, probably due to higher amount of cementitious materials, lower water cementitious materials ratio, high fly ash content and the absence of coarse aggregate. Moreover, in the same study, Sahmaran and Li (2009b) also studied the absorption rate in cracked ECC, and found that the use of water repellent admixture in the production of ECC could easily inhibit the sorptivity even for the mechanically pre-loaded ECC (Figure 2.7).

The reason for the relatively low permeation and diffusion cracked ECC specimens are not only due to the tight crack width but also the presence of self-healing of the microcracks. The self-healing of cracks becomes prominent when crack width is small. Based on experimental results, Evardsen (1999) and Reinhardt and Jooss (2003) proposed that crack widths below 0.10 mm can be closed by a self-healing process (Evardsen, 1999; Reinhardt and Jooss, 2003). In the case of pre-cracked ECC specimens exposed to water or salt solution or under wet and dry cycles, microcracks in ECC were found to close due to self-healing, thus slowing further water intake, reducing the rate of water absorption and diffusion (Lepech and Li, 2005b; Sahmaran et al., 2007). For example, an environmental scanning electron microscope (ESEM) observation of the fractured surface of ECC across a healed crack after exposed to salt solution is shown in Figure 2.8. The ESEM observations show that most of the products seen in the cracks were newly

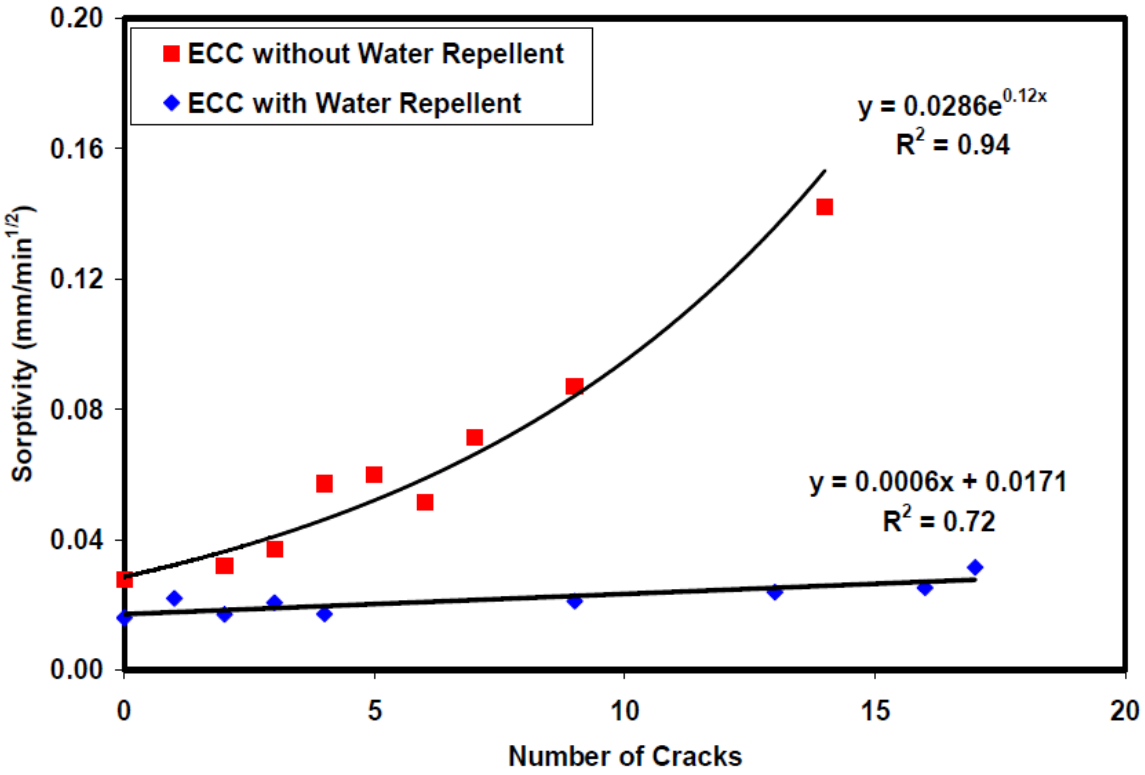

Figure 2.7 Sorptivity versus number of crack for ECC mixtures (Sahmaran and Li, 2009b)

formed calcium-silicate-hydrate (C-S-H) gels, which are the basic cementing compound produced by the hydration reactions. This can be attributed primarily to the large fly ash content and relatively low water to binder ratio within the ECC mixture. The continued pozzolanic activity of fly ash is responsible for the self-healing of the crack which further reduces the ingress of the chloride ions.

2.3.5 Corrosion Resistance

Reinforcing steel bars embedded in concrete are usually well protected against corrosion by the high alkalinity of pore water because the steel surface is passivated in the presence of oxygen. However, reinforcing steel bars in concrete structures are depassivated when the chloride concentration reaches threshold levels on the rebar surface, or when the pH of the concrete cover drops below critical levels due to carbonation (Tuutti, 1982). Some of the most commonly used protection methods for new constructions against steel reinforcement corrosion include high quality (low water to cement (W/C) ratio and good consolidation) concrete, increased concrete

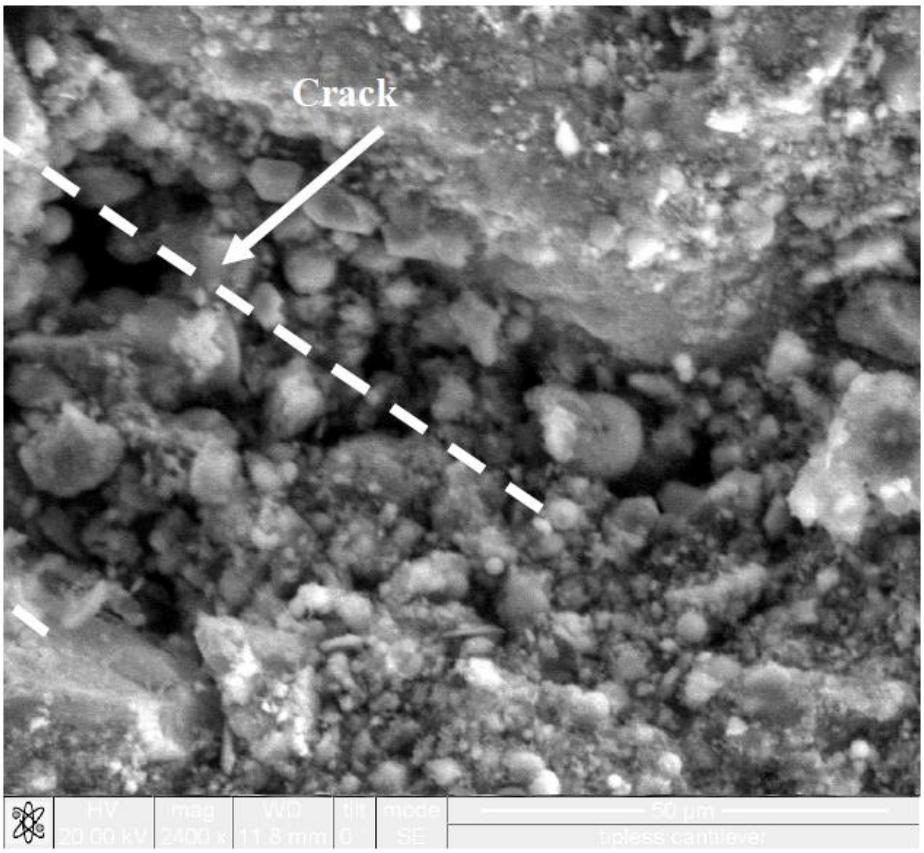

Figure 2.8 ESEM micrograph of rehydration products in a self-healed crack after exposure to salt solution (Sahmaran et al., 2007)

cover thickness, and use of epoxy coated steel reinforcing bars. Generally, low W/C ratio and good consolidation contribute to the reduction in permeability. A higher cover thickness is supposed to provide better physical protection because the concrete acts as a barrier which delays access of chloride ions, carbon dioxide and moisture to the steel reinforcement. However, as a result of restrained shrinkage, thermal deformations, chemical reactions, poor construction practices and mechanical loads, concrete unavoidably cracks and, over time, chlorides, carbon dioxide and moisture can penetrate even high quality concrete or concrete with good cover thickness (ACI Committee 224R, 2001). In addition, a larger cover thickness is known to lead to a greater crack width. Further, epoxy coatings on the surface of steel reinforcing bars are sometimes damaged during handling, or become brittle and delaminate from the steel reinforcing bars under high chloride concentrations, so that the reliability of epoxy coating for steel protection has been called into question (Federal Highway Administration (FHWA), 1992; Sagues et al., 1994; Manning, 1996). Consequently, corrosion of reinforcement occurs which

could lead to cover spalling and steel diameter reduction, and potentially diminishing of load capacity of the reinforced concrete member. At the root of this steel corrosion problem is the brittle nature of concrete materials. The brittleness of concrete inherently results in cracks that allow corrosives to penetrate the cover, and fail to resist the expansive force once corrosion starts.

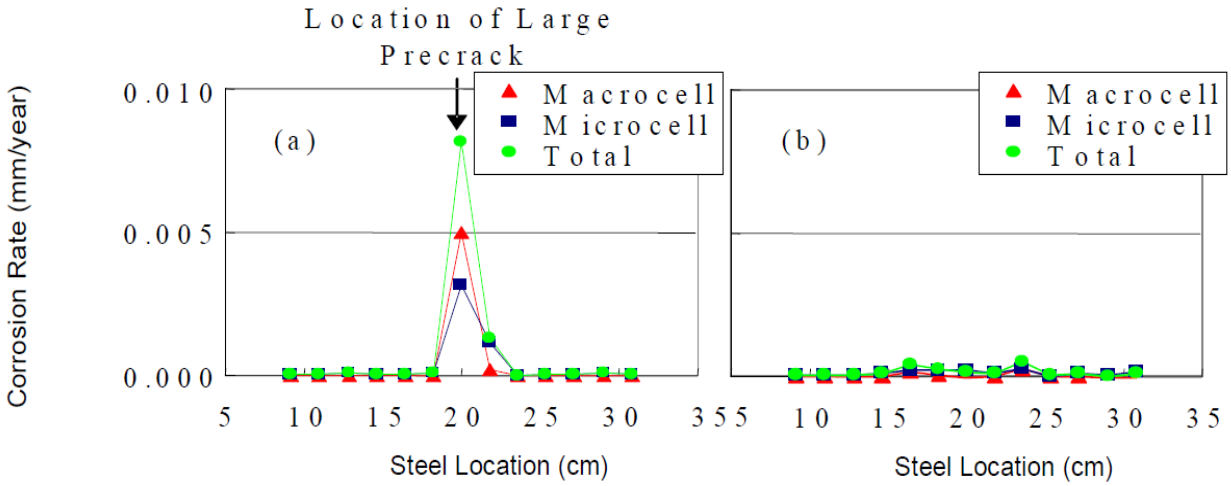

Figure 2.9 Microcell and macrocell corrosion rate measured for (a) R/C, and (b) R/ECC along the reinforcement bar length (Miyazato and Hiraishi, 2005)

With intrinsically tight crack width and high tensile ductility, ECC offers a significant potential to naturally resolving the corrosion related durability problem of reinforced concrete (R/C) structures. Concerned with the large number of microcracks within ECC in comparison to concrete, the rate of corrosion of reinforcing steel within an ECC matrix has been investigated and compared to R/C system (Miyazato and Hiraishi, 2005). Preloaded R/ECC and R/C beams were exposed to a chloride environment to accelerate the corrosion process. To determine the corrosion rate of ECC and concrete, macrocell and microcell corrosion rates were separately determined. The total (macro and micro cell) corrosion rate was measured to be less than 0.0004 mm/year but exceeded 0.008 mm/year in the steel reinforcement in the R/ECC and R/C beams respectively (Figure 2.9).

In another study, Sahmaran et al. (2008) investigated the cracking behaviour and residual flexural load capacities of reinforced ECC (R/ECC) specimens and R/mortar specimens, which have equal compressive strength to the ECC. During accelerated corrosion test at constant

applied voltage, corrosion-induced crack width of the mortar specimens were found to increase with time as corrosion activity progressed. Larger crack widths up to 2.00 mm were observed at higher levels of corrosion (Figure 2.10). Moreover, corrosion of reinforced mortar beam specimens resulted in a marked reduction in stiffness and flexural load capacity. After 25 hours accelerated corrosion exposure, the flexural load reduced to about 34 % of the flexural capacity

Figure 2.10 ECC and mortar specimens after accelerated corrosion test: (a) ECC prismatic specimen after 300 hours accelerated corrosion, (b) Mortar prismatic specimen after 75 hours accelerated corrosion, (c) ECC cylindrical specimen after 350 hours accelerated corrosion, (d) Mortar cylindrical specimen after 95 hours accelerated corrosion (Sahmaran et al., 2008)

of the control mortar beam. On the other hand, crack widths (~ 0.1 mm) of ECC remained nearly constant with time as corrosion activity progresses, while the number of cracks on the surface of the ECC specimens increased. The results of this study also showed that ECC has significant anti-spalling ability compared with conventional mortar (Figure 2.10). In contrast to mortar specimens, the ECC beam specimens after 50 hours accelerated corrosion exposure retained almost 100% of the flexural capacity of the control specimens. Beyond 50 hours, the flexural capacity decreases, but retained over 45% that of the control specimens even after 300 hours of accelerated corrosion exposure.

2.3.6 Freeze Thaw and Salt Scaling Resistance

It is well known that the cyclical freeze-thaw cycles and the use of de-icing salts during winter are two of the major causes of rapid degradation in concrete pavements, bridge decks, parking structures, and similar structures. ECC used for this kind of structures must be resistant to cyclical freezing and thawing, and the effects of de-icing agents. It is known that a proper air-void system is generally needed in normal concrete to avoid internal cracking due to freeze-thaw cycles and scaling due to freezing in the presence of de-icing salts. Durability of non-air-entrained ECC specimens was tested by exposure to cycles of freezing thawing testing, in accordance with ASTM C666 (Li et al., 2003). Non-airentrained concrete specimens were also tested as reference specimens. Non-airentrained specimens were used as control since no air entrainment was added to the ECC mixtures. After 110 cycles, the concrete specimens had severely deteriorated, requiring removal from the freeze-thaw machine, as mandated by the testing standard. However, all ECC specimens survived the test duration of 300 cycles with no degradation of dynamic modulus.

Figure 2.11shows the typical surface condition of the after 300 freeze-thaw cycles and fog room cured prismatic ECC specimens. This performance results in a durability factor of 10 for concrete compared to 100 for ECC, as computed according to ASTM C666 (1991). In uniaxial tension tests performed on wet cured and freeze-thaw exposed ECC tensile coupons at the same age, no significant drop in strain capacity was experienced after 300 cycles. Both wet cured and freeze thaw specimens exhibited a strain capacity of roughly 3%. (a) fog room curing (b) after 300 freeze-thaw cycles

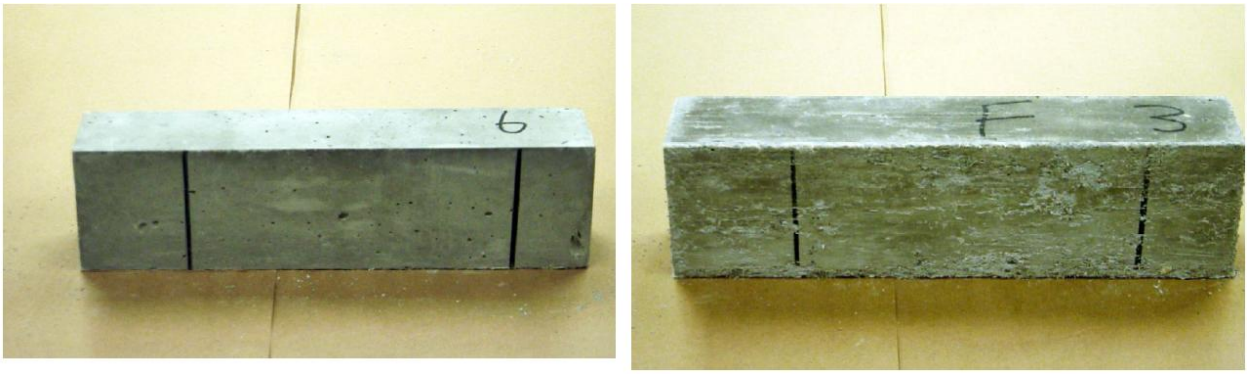

Figure 2.11 ECC specimen surface appearance after (a) normal curing and (b) freeze-thaw cycles (Sahmaran and Li, 2007)

Numerous laboratory test data in accordance with ASTM C 672 (2001) have indicated that air entrained concretes incorporating high volume fly ash often perform unsatisfactorily when exposed to freezing and thawing cycles in the presence of de-icing salts. For the production of ECC, as much as two-thirds of the Portland cement is substituted by fly ash. Due to the high volume fly ash content, it is important to test the performance of ECC exposed to freezing and thawing cycles in the presence of de-icing salt. Salt scaling resistance of non-air-entrained sound (uncracked) and mechanically pre-loaded (cracked) ECC specimens were evaluated by Sahmaran and Li (2007) in accordance with ASTM C672. Non-air-entrained mortar specimens with and without fly ash were also tested as reference specimens. After 50 freeze-thaw cycles in the presence of de-icing salt, the surface condition visual rating and total mass of the scaling residue for ECC specimens, even those with high volume fly ash content, remained within acceptable limits of ASTM C672 (Figure 2.12). This level of durability hold true even for ECC specimens pre-loaded to high deformation levels and exhibiting extensive micro-cracking. In comparison, reference mortar specimens under identical testing conditions deteriorated severely. Moreover, the replacement of fly ash with cement in mortar further exacerbated deterioration due to freezing and thawing cycles in the presence of de-icing salt. In a separate test, both pre-loaded (cracked) and sound ECC coupon specimens were exposed to freeze-thaw cycles in the presence of de-icing salts for 25 and 50 cycles to compare residual tensile strength and ductility of

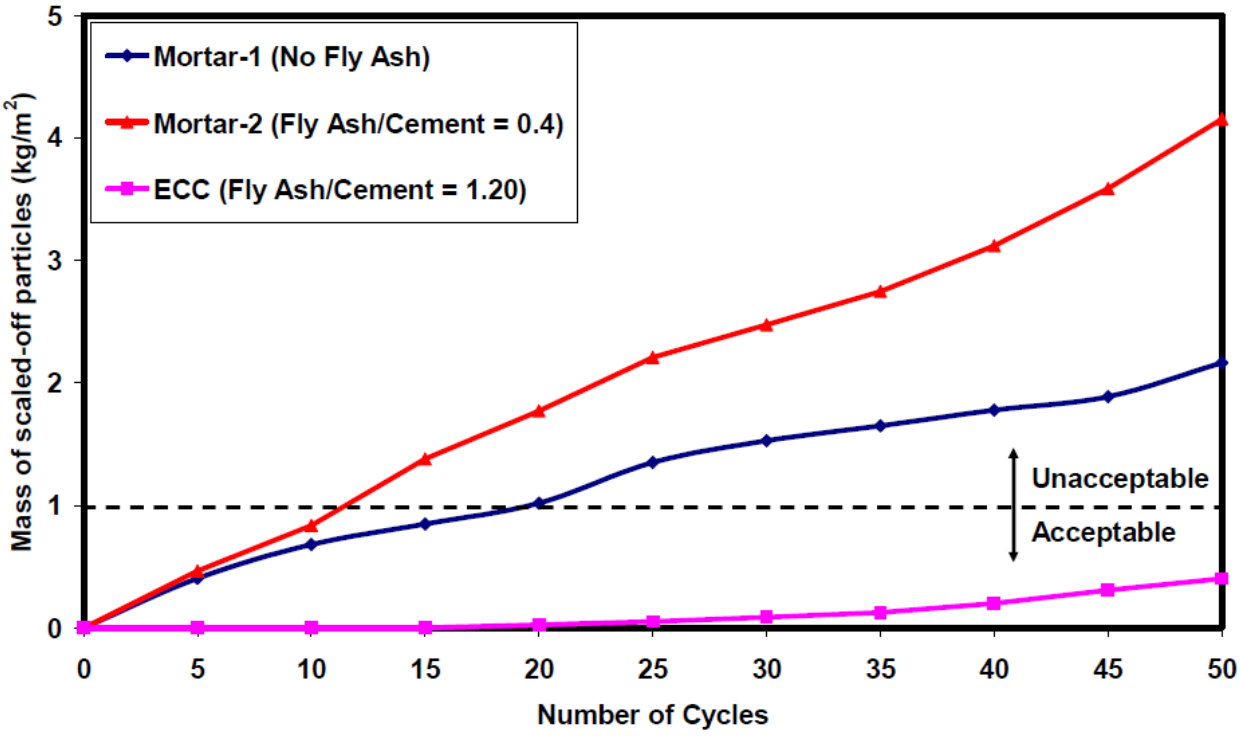

Figure 2.12 Mass of scaled-off particles versus number of freeze thaw cycles for virgin mortar and virgin ECC prisms in presence of de-icing salts (Sahmaran and Li, 2007)

reloaded ECC specimens. The preloaded specimens showed negligible loss of ductility, and retained the multiple micro-cracking behaviour and tensile strain capacity of more than 3%. It was also discovered that micro-cracks due to mechanical loading will heal sufficiently under freezing and thawing cycles in the presence of salt solutions, restoring them to nearly the original stiffness. These results confirm that ECC, both sound and micro-cracked, remains durable despite exposure to freezing freeze-thaw cycles in the presence of de-icing salts.

2.3.7 Durability under Extremely Hot and Humid Environments

In contrast to freeze thaw tests which are designed to simulate temperature changes in winter conditions, hot water immersion tests were conducted to simulate the long term effects of hot and humid environments. To examine the effects of environmental exposure, hot water immersion was performed on individual fibers, single fibers embedded in ECC matrix, and composite ECC material specimens (Li et al., 2004). Specimens for both individual fiber pull-out and composite ECC material were cured for 28 days at room temperature prior to immersion in hot water at 60ºC for up to 26 weeks. After 26 weeks in hot water immersion, little change was seen in fiber

properties such as fiber strength, fiber elastic modulus, and elongation. The tensile strain capacity of the ECC dropped from 4.5% at early age to 2.75% after 26 weeks of hot water immersion. While accelerated hot weather testing did result in lower strain capacity of ECC, the 2.75% strain capacity exhibited after 26 weeks remained over 250 times that of normal concrete.

2.3.8 Durability under Highly Alkaline Environments

Another environment that could affect the microstructure and composite properties of ECC is a high alkaline environment. In addition to high alkaline matrix pore water solution, ECC can come into contact with alkaline media through interaction with a variety of alkaline chemicals, soil (or solutions diffusing through soil) and seawater. Even though no deleterious expansion has been expected due to alkali silica reaction because of the high volume fly ash (HVFA) content, small aggregate particle size and micro-fibers in ECC (Sahmaran and Li, 2008), durability of HVFA-ECC must be evaluated under high alkaline environments. Alkalis will penetrate through microcracks or even the uncracked matrix that could lead to modifications in the material microstructure and hence changes in the composite properties.

Sahmaran and Li (2008) investigated the durability of ECC under high alkaline environment. The performance of ECC under high alkaline medium was tested according to ASTM C1260 (1994). The length change of the ECC bars was measured up to 30 days. Figure 2.13 shows expansive behaviour of the ECC. The classification ranges given from the ASTM C 1260-94 (1994) are illustrated graphically in Figure 2.13 by horizontal gridlines. The results obtained from accelerated mortar bar test indicated that ECC did not show any expansion at the end of 30 days soaking period probably due to non-reactive fine aggregate. However, even if reactive silica sand and alkalis are present in ECC, it cannot be expected to develop deleterious expansion due to alkali silica reaction (ASR) because of the high volume fly ash content, small aggregate particle size and micro-fibers in ECC.

In the same study, Sahmaran and Li (2008) evaluated the mechanical performance of both virgin and mechanically-loaded ECC under high alkaline environments. ECC coupon specimens were firstly pre-loaded under uniaxial tension to different strain levels, and then exposed to an alkaline environment up to 3 months at 38^{o}C and reloaded up to failure. The reloaded specimens showed slight loss of ductility and tensile strength, but retained the multiple micro-cracking behaviour

and tensile strain capacity of more than 2% (about more than 200 times that of normal concrete and normal fiber reinforced concrete). The test results indicated strong evidence of self-healing

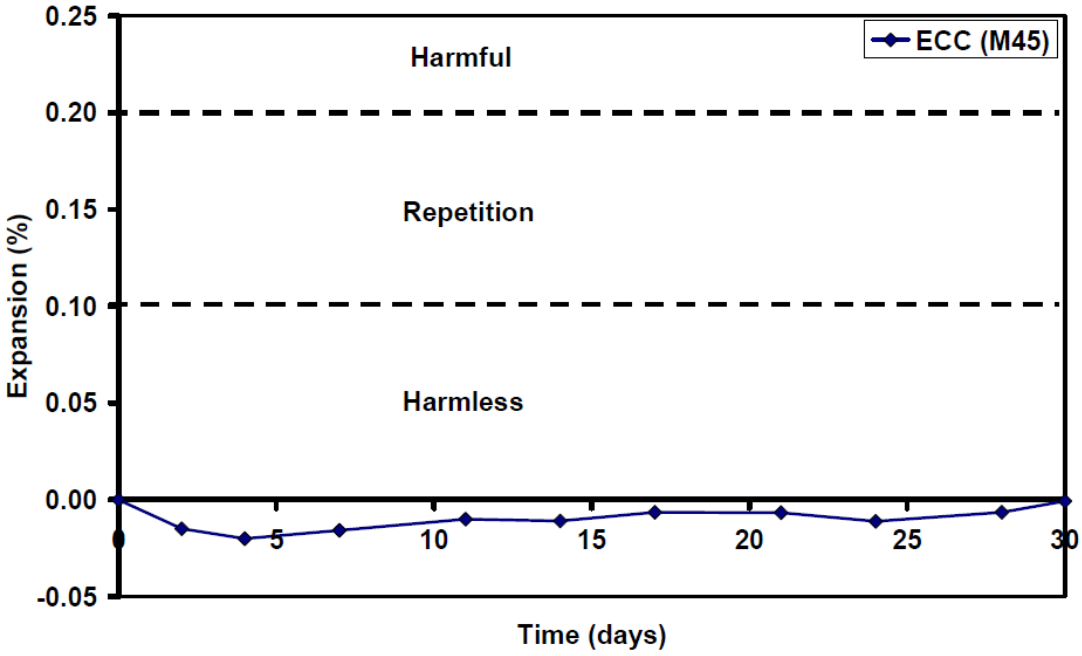

Figure 2.13 Expansion time histories for ECC (ASTM Standard C1260-94, 1994; Sahmaran and Li, 2008)

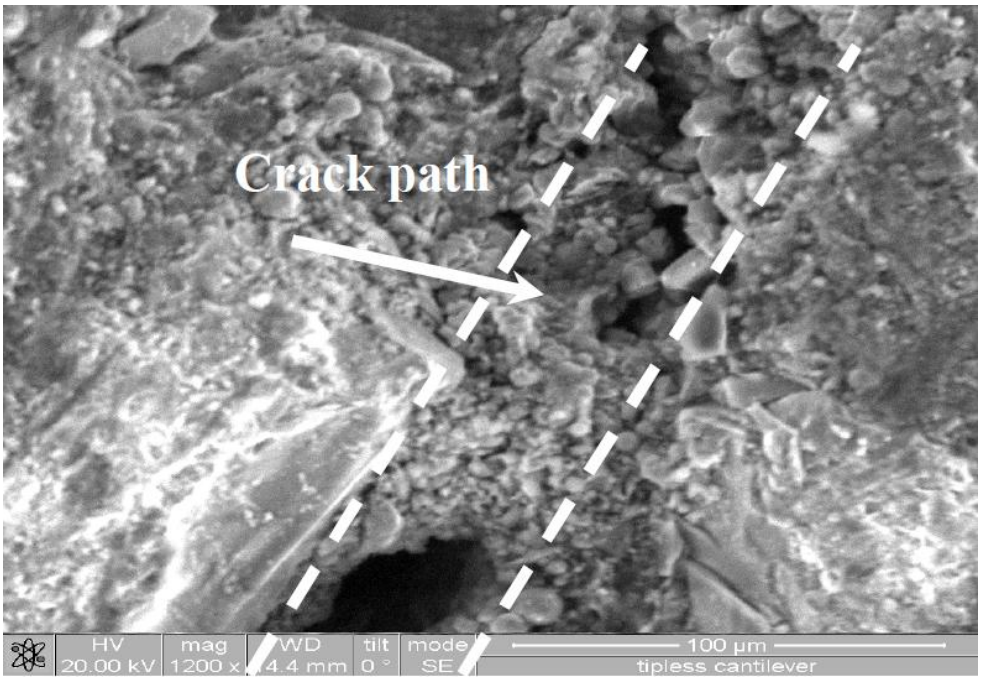

Figure 2.14 ESEM micrograph of rehydration products in a self-healed crack after 30-day sodium hydroxide solution exposure period (Sahmaran and Li, 2008)

of the micro-cracked ECC material, which can still carry considerable tensile stress and strain and restore nearly the original stiffness. This observation is also supported by an environmental scanning electron microscope (ESEM) observation of the fractured surface of ECC across a healed crack. The phenomenon of self-healing effectively closes the microcracks even after one month sodium hydroxide solution exposure period (Figure 2.14).

2.4 Application of ECC for Bridge Deck Link Slab

2.4.1 Introduction

Large scale highway and superhighway infrastructure remains the backbone of national and international trade supporting the economies of both highly developed and developing nations worldwide. Many highway bridges of these highways are composed of multiple span, steel or prestressed concrete girders simply supported at piers or bents. The girders support cast-in-place concrete decks. A mechanical joint is typically employed at the end of the simple span deck to allow deck deformations imposed by girder deflection, concrete shrinkage, and temperature variations. It is well known that bridge deck joints are expensive to install and maintain. Deterioration of joint functionality due to debris accumulation can lead to severe damage in the bridge deck and substructure. The durability of beam ends, girder bearings, and supporting structures can be compromised by water leakage and flow of deicing chemicals through the joints. A significant negative economic impact of mechanical joints in all phases of bridge service life, from design to construction and maintenance, was documented by Wolde-Tinsae and Klinger (Wolde-Tinsae and Klinger, 1987). A possible approach to alleviate this problem is the elimination of mechanical deck joints in multi-span bridges.

Two solutions to eliminate deck joints have been attempted, specifically an integral construction concept with girder continuity and a jointless bridge deck concept with simply supported girders. Alampalli and Yannoti (1998) found that the jointless deck construction practice is generally more efficient than the integral bridge construction practice. Based on field inspection of 105 jointless bridge decks, including 72 with concrete superstructures and 33 with steel superstructures, it was found that the bridges were functioning as designed without significant problems except for minor deck cracking. While further improvement on jointless bridge deck

construction practice was recommended, Alampalli and Yannotti (1998) concluded that as a group, they generally perform better than decks with joints.

The section of the deck connecting the two adjacent simple-span girders is called the link slab (Figure 1.1). Caner and Zia (1998) experimentally analyzed the performance of jointless bridge decks and proposed design methods for the link slab. These investigations revealed that the link slab was subjected to bending under typical traffic conditions rather than axial elongation. Tensile cracks were observed at the top of the link slab under service conditions due to a negative bending moment. For steel girders, the measured maximum crack width was 300 μm at 40% of ultimate load and 750 μm at 67% of ultimate load. They pointed out that additional tensile stress may be imposed on the link slabs due to shrinkage, creep, and temperature loading, and that crack width must be carefully controlled. The recommendation was to use epoxy coated reinforcing bars in the link slab in order to avoid reinforcement corrosion. To reduce the stiffness of the link slab, debonding of the link slab over the girder joint for a length equal to 5% of each girder span was also recommended. This link slab concept can be used for new bridge decks and also for replacement of deteriorated joints of existing bridge decks.

Ability to resists tensile and shear force while retaining compatibility with normal concrete in almost all other respect makes ECC the right material for the link slab application. As seen and confirmed in the previous discussion, self compatibility makes ECC an ideal material as congestion is a major concern of a link slab due highly reinforced structural element. The fresh properties of ECC can be adjusted by optimizing the composition of ECC for given workability requirements. Given the ability to self-control tight crack width regardless of the amount of reinforcement, the use of ECC as a material for bridge deck link slabs has been proposed (Li et al. 2003; Kim et al. 2004; Kim and Li 2004). The research revealed that the property requirements for link slab applications were satisfied by the mechanical properties of ECC material. Thus, the introduction of ECC to link slab construction is proposed for its ability to control crack widths and its processing flexibility.

2.4.2 Design Consideration of Link Slab with ECC

In a jointless bridge deck system, an ECC link slab can be used to accommodate bridge deck deformations due to temperature variation, live load, and shrinkage, replacing a typical

expansion joint or concrete link slab. The interface between concrete and ECC, however, may become a weak link due to minimal mechanical interaction and load transfer across the cold joint between the existing concrete deck and newly cast ECC link slab, as the concrete and ECC are not cast at the same time. This phenomenon has been observed by Gilani and Juntunen (2001), Gilani and Jansson (2004) in a preliminary laboratory investigation, where the design of an ECC link slab followed conventional concrete link slab design procedures. During their monotonic test to failure on a specimen simulating a jointless bridge deck using an ECC link slab, the interfacial crack between ECC and concrete grew noticeably while the width of cracks in the ECC link slab were maintained below 100 μm. This indicated that a macroscopically crack-free bridge deck system may be difficult to realize due to potential large interfacial cracks, even though ECC material satisfies the property requirements of link slab design.

This conventional design procedure for concrete link slabs did not address this potential interfacial cracking problem. In the design of conventional concrete link slabs (Caner and Zia, 1998), the debond zone begins at the interface between the link slab and the concrete deck (Figure 2.15a). This imposes high stress concentrations at this interface. Improvements in the interface design of an ECC link slab were investigated (Qian et al., 2009) using numerical structural analysis.

In the proposed new approach for designing the transition zone (Figure 2.15b) at the ends of the ECC link slab, however, the location of the shear studs connecting the steel girder and the deck were extended into part of the ECC link slab, shifting the high stress concentration expected at the end of the debond zone away from the ECC/concrete interface. In addition to shear studs, the existing longitudinal reinforcement is lap spliced with new reinforcing bars within the ECC link slab. This creates a transition zone between the debonded portion of the ECC link slab and the concrete deck or between the structural interface and the material interface (Figure 2.15 b). The shear studs and lap-spliced reinforcement located within the transition zone facilitate stress transfer between the concrete deck and the ECC link slab. These modifications are expected to prevent any failure of the ECC/concrete joint, but allow the free portion of the ECC slab to inelastically deform in response of tensile stretching, thus functioning as a jointless expansion joint. For constructability reasons, severe cold weather casting of ECC link slabs is not

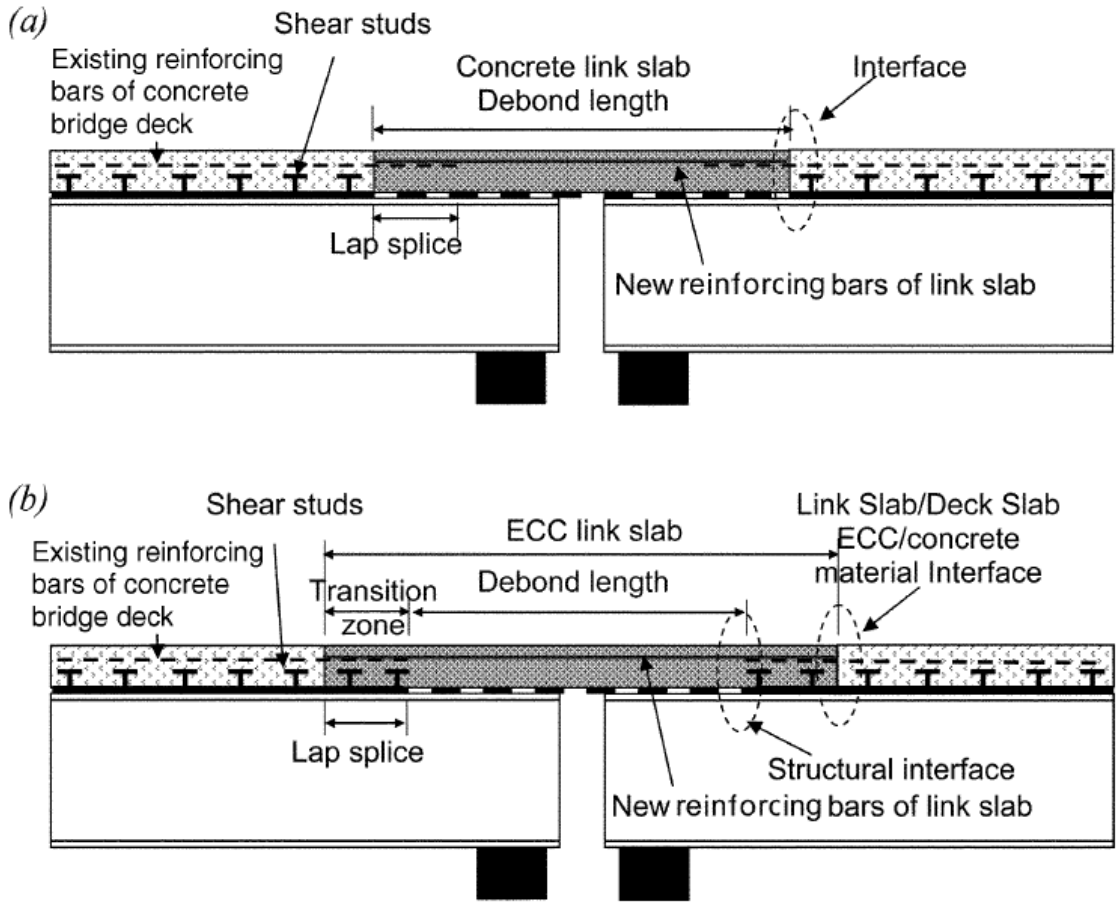

Figure 2.15 Schematics of link slab design concepts for: (a) conventional method without considering transition zone; and (b) proposed method focusing on transition zone design. (Qian et al., 2009)

recommended (Li et al. 2005). Due to this, most thermal deformation imposed upon the ECC link slab will be tensile in nature. Therefore, compressive strains due to thermal deformation will not be of significance to the design of ECC link slabs.

Using these guidelines Qian et al. (2009) tested two full scale link slab specimens by incorporating conventional ECC mix design. Based on this experimental test it was concluded that the addition of shear studs in the transition zone proved to be very effective in shifting the stress concentration from the interface to the bulk part of the link slab. As a result of this stress concentration shifting, no cracking was observed at the bridge deck/link slab interface under fatigue loading, whereas desirable microcracking formed over the debond zone of the link slab up to the location of shear studs. Moreover, experimental investigations demonstrated the feasibility and advantages of the proposed transition zone design in the ECC link slab. Overall,

the proposed transition zone design approach combined with advanced ECC material made ECC link slab a feasible solution for bridge deterioration problems associated with mechanical expansion joints, and potentially much more durable compared with concrete link slabs designed using conventional methods.

2.4.3 Shear Stud-ECC Interaction

As discussed above, stud connectors are widely used in beams and bridge girders to form composite action between steel and concrete. Composite beams have gained popularity in bridges since the 1950s due to the contributions of Viest on the stud shear connectors (1956a,b; 1960). Their primary growth in building construction was a result of the simplified design provisions introduced into the 1961 AISC specification (Driscoll and Slutter, 1961).

Thus far, research on stud connections is conducted at two levels: the pushout sub-assemblage level and composite beam level. Test results from pushout specimens can be used for designing composite beams because they give conservative values of the ultimate strength (Driscoll and Slutter 1961). Previous research (Ollgaard et al. 1971; Oehlers and Foley 1985; Yen et al. 1997; Bursi and Gramola 1999) on both levels revealed that concrete fracture contributed to the failure of pushout specimens or composite beams.

In most of the cases, the catastrophic failure can be attributed to the high stress concentration induced by the stiff steel stud bearing against the brittle concrete materials. It was predicted that using a more ductile concrete material may result in improved performance for stud connections in terms of structural strength, ductility, and integrity. Qian and Li (2006) did experimental work to understand shear stud- ECC interaction by conducting pushout test. ECC with two different compressive strengths were tested along with the normal mortar.

Specimen testing after curing them for 28 days in air proved that ECC due to its strain-hardening, higher tensile strain and micro-cracking behaviour achieved much higher load capacity and slip capacity compared with concrete specimens with similar compressive strength. Twenty-four to fifty-three percent increases in load capacity and 220% increase in slip capacity were achieved in the test range (Qian and Li, 2006). All the concrete pushout specimens failed by brittle fracture failure associated with a lower ultimate strength where the ECC pushout specimens were gradually damaged by ductile yielding of ECC materials and plastic deformation

of steel stud, resulting in a higher load-carrying capacity. This phenomenon is due to the ductile nature of the ECC material that ensures a shift of failure mode from brittle concrete fracture to ductile yielding of ECC materials and eventual fracture of the stud shank after extensive plastic deformation. This significant enhancement of ductility suggests that the use of ECC material can be effective in redistributing loads among the shear studs and in improving composite action between steel girder and concrete bridge deck.

2.5 Applications of ECC

To illustrate the versatility of ECC in real world applications, a number of recent/ongoing projects involving the use of ECC are briefly highlighted. Figure 2.16 shows the repair of the Mitaka Dam in Hiroshima-Prefecture, Japan in April, 2003 (Sakata et al., 2004). This dam is over 60 years old, with a severely damaged concrete surface. Cracks, spalling, and water leakage were concerns that prompted the use of ECC as a water-tight cover layer. This 20 mm layer was applied by spraying the ECC material directly onto approximately 600 m^2 of the upstream dam surface.

A second large-scale application (Rokugo et al., 2005) in Japan used ECC for repair of a concrete gravity earth-retaining wall (18 m in width and 5 m in height) that has been damaged by (ASR) cracking. The decision to use ECC for the 50-70 mm thick repair was based on the need to prevent reflective cracking from the substrate concrete through the repair layer (Li and Lepech, 2004). Such reflective cracking was anticipated had normal concrete been used for the repair. Since this repair was completed, this project performance has been continuously monitored. Ten and twenty-four months following the repair, microcrack widths in the ECC repair layer remain below 50 μm and 120 μm respectively, while the maximum crack widths in the premixed concrete repair mortar section (used as a control) were 0.2 mm and 0.3 mm, respectively (Kunieda and Rokugo, 2006).

Figure 2.16 Spray repair of the Mitaka dam with ECC for water-proofing (Sakata, et al., 2004)

Also in Japan ECC has been used in structural applications as coupling beams (Maruta et al., 2005) within high rise concrete construction. Due to the high energy absorption capacity of steel reinforced ECC material, the application of this material in coupling beams which connect adjacent core walls is very advantageous for high rise buildings in seismic regions. The recent development of precast ECC coupling beam elements by Kajima Corporation in Japan can be easily integrated into current seismic construction practices. Currently two high-rise buildings in Tokyo, Japan have been built integrating ECC coupling beams (Figure 2.17).

As one of the first field applications of ECC in the US, a concrete bridge deck patch was completed in cooperation with the MDOT in 2002. A complete summary of this work has been outlined by Li and Lepech (2004). During this work, one section of a deteriorated bridge deck was repaired with ECC while the remaining portion was repaired with a commercial concrete patching material commonly used by the MDOT (Figure 2.18). This repair scenario allowed for a unique

Figure 2.17 The Nabeaure Tower in Yokohoma, Japan uses precast ECC coupling beams in building core for seismic resistance (Maruta et al., 2005)

ECC/concrete comparison subjected to identical environmental and traffic loads. The concrete repair material used was a pre-packaged, commercially available repair mortar. At this writing, the repaired bridge deck has experienced more than six complete Michigan winter cycles of freezing and thawing, in addition to live loads. While the ECC patch repair has survived in this combined loading environment with minor micro-cracking limited to less than 50 μm, the concrete repair portion has developed localized cracks in excess of 3.5 mm wide and required re-repair in 2005.

In addition to bridge deck patching repairs, the most recent field application of ECC in the US is with a bridge "link slab" completed in cooperation with MDOT in 2005 (Figure 2.19). Within this "link slab", the material ductility of ECC is leveraged to replace problematic expansion joints within simply support multi-span bridges with a ductile ECC slab which links the adjacent simple spans (Li et al., 2005). In this project, about 32 m^3 of ECC were cast in place using standard ready-mix concrete trucks to build the first ECC link slab in US. With a strain capacity exceeding 2%, these composites can be used to replace traditional steel expansion devices and

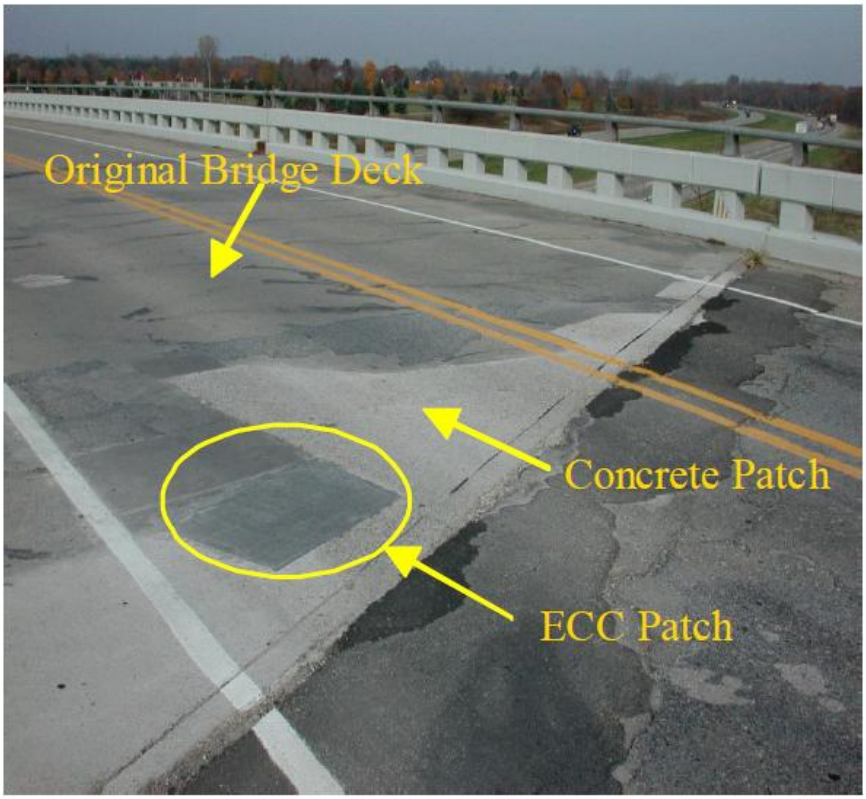

Figure 2.18 ECC patch repair on Michigan bridge deck (Li et al., 2005)

can fully accommodate the thermal deformations of adjacent bridge spans. (a) during construction (b) after construction.

Figure 2.19 ECC link-slab on Grove Street Bridge, Michigan (Qian et al., 2009)

2.6 Summary

Based on these review of the literature, it is clear that there have been research done about ECC ranging from micromechanics of the ECC to the performance of ECC under severe environmental exposures. In addition, the demonstration projects of ECC link slab application proved that ECC is one of the best solutions which can be used in the link slab application. ECCs performance is above satisfactory level among almost each and every aspect ranging from chloride attack, freezing and thawing effect in the presence of de icing salt, corrosion resistance of reinforcement bars embedded in ECC or water permeability. So the time has come to use the ECC more and more in to commercial application. However, construction industry being highly cost sensitive, authorities and engineers are reluctant to implement ECC into common construction industry practise.

Standard ECC mixtures use microsilica sand as an aggregate type. The development of a cost-effective ECC with locally available materials is important for such composite material to be used more commonly in the construction industry in future. Commercially available microsilica sand is relatively expensive and difficult to obtain compared to locally available sands. Therefore, it is important to investigate how the size and type of commonly available sands influence the mechanical and ductility behaviour of ECC. Simultaneously, other factor of major concern is higher cement volume in ECC. No significant effort has been done in the direction of using supplementary cementitious materials as a partial replacement of cement. Partial replacement of this higher volume of cement with supplementary cementitious composite will make ECC greener and sustainable and will make ECC more adoptable in the construction industry.

In nutshell, research studies are limited and some of the issues need to be further explored and experimented. So there is a need of research which will further explore and analyze mix design, mechanical and durability aspects of different ECC mixtures and their applications to link slab in a jointless bridge deck. This research will also cover the effect of various mix design parameters such as: amount and type of supplementary cementing materials (SCMs) (such as fly ash, slag) and type of aggregate (microsilica sand and locally available crushed sand) content on fresh, mechanical and durability properties of ECC. The structural performance of ECC link slab in bridges will also be studied in comparison to other forms of concrete.

CHAPTER THREE

EXPERIMENTAL PROGRAM FOR FRESH, MECHANICAL AND DURABILITY PROPERTIES

3.1 Introduction

Engineered cementitious composite (ECC) mixtures with different SCMs and different aggregate types were developed based on early research studies at Ryerson University. The evaluation of fresh, mechanical and durability properties of these ECC mixtures was conducted to make sure whether they could meet the requirements for the structural application specifically for link slab in the bridge deck construction. To perform the performance validation for these ECC mixtures, small-scale link slab specimens were cast and tested under static monotonic loading behaviour. This chapter describes the materials and methods utilized in the development of ECC including the testing procedures and fresh, mechanical and durability properties of concrete. Structural test setups for link-slabs and associated other tests will be explained in the Chapter 6.

3.2 Concrete Materials

3.2.1 Cement

Type GU (general use), hydraulic cement in compliance with CSA A3001-03 (type 10 normal portland cement) was used. Chemical, physical and strength properties of cement are shown in *Table* 3.1

3.2.2 Supplementary Cementitious Material (SCM)s

Three different supplementary cementitious materials were used as a cement replacement to generate different mix designs. These SCMs were incorporated as different replacement ratios of the cement.

3.2.2.1 Fly Ash

Two different types of fly ash were used for the preparation of 10 different ECC mixes, namely: (1) Class CI FA and (2) Class F FA. The Chemical and Physical properties of both types of fly ash are shown in *Table* 3.2

Table 3.1 Chemical and physical properties of type GU cement

Chemical Analysis (%)	**Cement**
Loss on ignition LOI	2.30
Silicon Dioxide SiO_2	19.60
Aluminium Oxide $Al2O_3$	4.90
Ferric Oxide Fe_2O_3	3.10
Calcium Oxide CaO	61.40
Magnesium Oxide MgO	3.00
Sulfur Trioxide SO_3	3.60
Tricalcium Silicate C_3S	52.26
Dicalcium Silicate C_2S	17.37
Tricalcium Aluminates C3A	10.39
TetraCalcium Aluminoferritte CaO	7.75
Total Alkali	1.00
Free Lime CaO	0.79
Physical Analysis	**Cement**
Residue 45 µm(%)	3
Blaine (m^2/kg)	410
Initial Setting time (min.)	113
Relative Density (g/cm^3)	3.15
Compressive Strength (MPa) 1 day	19.41
Compressive Strength (MPa) 3 day	30.35
Compressive Strength (MPa) 28 day	41.47

3.2.2.2 Blast Furnace Slag

Blast furnace slag was used as a SCM for some of the mixes. The chemical and physical properties of slag are shown in *Table* 3.2.

3.2.3 Water

Clean drinkable water with a temperature ranging between 22° and 25° C was used.

Table 3.2 Chemical and physical properties of fly ash and slag

Chemical Composition %	**Class F FA**	**Class CI FA**	**Slag**
Sum (SiO_2+Al_2O_3+Fe_2O_3)	85.6	71.12	48.9
Silicon Dioxide SiO_2	59.5	41.57	35.4
Aluminium Oxide Al_2O_3	22.2	26.12	13
Ferric Oxide Fe_2O_3	3.9	8.44	0.5
Calcium Oxide CaO	5.57	14.3	40.8
Magnesium Oxide MgO	-	3.4	8
Sulfur Trioxide SO_3	0.19	1.55	0.1
Alkalis as Na_2O (%)	2.75	0.71	0.2
Loss of Ignition LOI (%)	0.21	1.49	-
Physical Analysis	Class F FA	Class CI FA	Slag
Residue 45 μm (%)	9.6	17.5	-
Density (g/cm^3)	2.18	2.43	2.11

3.2.4 Aggregate

ECC is a special type of concrete where coarse aggregates are not used. For this reason, only fine aggregates were used. Two different types of fine aggregates were incorporated for ECC mixes: microsilica sand and crushed sand. The crushed sand used for the research was the one passing 100 % from 1.19 mm (No. 16) Sieve. The grading of these fine aggregates were conducted in accordance with ASTM C 136 (2006) and ASTM C 117 (2004). Their grain size distributions are tabulated in *Table* 3.3 and *Table* 3.4.

Table 3.3 Sieve analysis of microsilica sand

Sieve #	No. 40	No. 50	No. 70	No. 100	No. 140	No. 200	No. 270	Pan
Opening (μm)	420	297	210	149	105	74	53	0
% Passing	100	97.8	83.1	35.6	6.3	0.9	0.4	Trace

Table 3.4 Sieve analysis of crushed sand passing 100 % from 1.19 mm

Sieve #	No. 16	No. 20	No. 30	No. 50	No. 100	No. 200	PAN
Opening (mm)	1.19	0.841	0.6	0.3	0.15	0.075	0
% Passing	100	94	82.5	40	9.75	1.25	Trace

3.2.5 High Range Water Reducing Agent (HRWRA)

ADVA®cast 575 from Grace Construction Products was used as HRWRA. ADVA® cast 575 is polycarboxylic-ether type high range water reducer with solid content of approximately 30% and

conforming to ASTM C 494 (2011) type F and ASTM C1017 (2007) type I. *Table* 3.5 shows the characteristics of ADVA®cast 757 as per the producer. One of the inherent properties of such HRWRA is to provide high early strength of concrete.

Table 3.5 Super plasticizer ADVA®cast 575

Description	Property
Color	Turkish Blue
State	Liquid
Odor	No data
pH	2.7-6.5
Boiling Point	100°C
Freezing Point	0°C
Specific Gravity	1.104-1.116

3.2.6 Fiber

Although various fiber types have been used in the production of ECC, PVA fiber was used in this study (Figure 3.1). PVA-ECC represents the most practical ECC used in the field (Kunieda and Rokugo, 2006; Li et al., 2001) at the present. The PVA fiber has attracted most attention due to the outstanding composite performance and economics consideration. The dimensions of the PVA fiber were 8 mm in length and 39 μm in diameter. The nominal tensile strength of the fiber was 1620 MPa and the density of the fiber was 1300 kg/m^3. The mechanical and geometric properties of PVA fiber are summarized in Table 3.6. The PVA fiber was surface-coated by hydrophobic oil (1.2% by weight) in order to reduce the fiber/matrix interfacial bond strength. To account for material in-homogeneity, a fiber content of 2% by volume in excess of the calculated critical fiber content had been typically used in the mix design. This was achieved through ECC micromechanics material design theory and had been experimentally demonstrated to produce good ECC properties in previous investigations (Li et al., 2001; Kong et al., 2003a).

Table 3.6 Mechanical and geometric properties of PVA fiber

Fiber Type	Nominal Strength (MPa)	Apparent Strength (MPa)	Diameter (μm)	Length (mm)	Young Modulus (GPa)	Strain (%)	Specific Weight kg/ m^3
PVA	1620	1092	39	8	42.8	6.0	1300

Figure 3.1 PVA fiber used in the production of ECC

3.3 Mix Designs

The intension was to develop at least three concrete mix designs suitable for the required structural performance, each containing different types of aggregate and SCMs. This selection was based on their performance in fresh, mechanical and durability properties.

In the first phase, all ten mixes were tested for the fresh and mechanical properties. In the second phase, out of ten mixes, three mixes were chosen based on the results of fresh and mechanical properties. The third and the final phase was the structural application of these three mixes for durability and tested for the scale down link slab models and to study their behaviour. To compare the result with normal concrete, self-consolidating concrete was chosen as control mix. There were two reasons for choosing SCC as a control mix: (1) SCC's other properties are similar to normal concrete except self-consolidating property and (2) heavily reinforced link slab section virtually makes it impossible to apply vibration. For this reason, SCC mix was chosen as control mix.

3.3.1 ECC Trial Mix

A total of ten trial mixes were developed by incorporating different type of SCM and aggregate. The mixes would contain either microsilica sand or 1.19 mm crushed sand as fine aggregate. A

total of three different supplementary cementitious material (SCM)s i.e. class F FA, class CI FA and slag were selected and they were incorporated as different cement replacement ratio. Based on previous research (Wang and Li, 2007b), these ratio were kept as 1.2% and 2.2%. As any

Table 3.7 Selected ECC trial mix design with microsilica sand

Component	ECC Mix Designation					
	SS_CI_1.2*	SS_CI_2.2	SS_SL_1.2	SS_SL_2.2	SS_F_1.2	SS_F_2.2
Water (W), kg/m^3	331	327	380	379	331	327
Cement (C), kg/m^3	570	386	575	395	570	386
Class CI FA, kg/m^3	684	847	-	-		
Class F FA, kg/m^3			-	-	684	847
Slag SL, kg/m^3	-	-	690	868	-	-
Microsilica sand (SS), kg/m^3	455	448	456	455	455	448
Fiber (PVA), kg/m^3	26	26	26	26	26	26
HRWRA, kg/m^3	5.4	3.9	4.5	3.9	4.9	3.7
CI/C	1.2	2.2	-	-	-	-
F/C	-	-	-	-	1.2	2.2
Slag/PC	-	-	1.2	2.2	-	-
Cement Replacement by SCM	55%	70%	55%	70%	55%	70%
W/B	0.27	0.27	0.30	0.30	0.27	0.27

* Mix Designation: SS represents microsilica sand, F represents Class F FA, CI represents class CI FA and 1.2 represents SCM/cement replacement ratio;

further cement replacement is not favorable for the durability properties. Out of this ten mixes, four mixes were developed using class CI FA, four mixes using Class F FA and two mixes using slag as a supplementary cementitious replacement materials. Previous studies have given excellent results using fly ash as an SCM (Glasser, 1991). This was the reason for giving more preference to the fly ash over slag. *Table* 3.7 and *Table* 3.8 show mix proportions of ECC mixtures with different types of SCMs and aggregate types. The water/binder ratio was kept in the range of 0.27 and 0.30.

Table 3.8 Selected ECC trial mix design with 1.19 mm crushed sand

Ingredients	ECC Mix Designation			
	CS_CI_1.2	CS_CI_2.2	CS_F_1.2*	CS_F_2.2
Water (W), kg/m^3	326	318	326	318
Cement (C), kg/m^3	558	375	558	375
Class CI FA, kg/m^3	671	825	-	-
Class F FA, kg/m^3	-	-	671	825
Crushed Sand(CS), kg/m^3	447	436	447	436
Fiber (PVA), kg/m^3	26	26	26	26
HRWRA, kg/m^3	6.2	4.2	6.0	3.6
CI/C	1.2	2.2	-	-
F/C			1.2	2.2
Cement Replacement by SCM	55%	70%	55%	70%
W/B	0.27	0.27	0.27	0.27

* Mix Designation: CS represents Crushed Sand, F represents FA Class F and 1.2 represents SCM/cement replacement ratio

3.3.2 SCC Mix

SCC was used as a control mix for the structural performance of ECC. Simultaneously, SCC was adopted in the casting of bridge deck in the link slab specimen. 28-day compressive strength of SCC was 61.5MPa and flexural strength was 3 MPa at 1 mm of ultimate mid-span deflection. Except coarse and fine aggregate, all the materials for SCC mix were the same as those of ECCs. Well graded coarse sand was used as a fine aggregate and 10 mm nominal size aggregate was used as coarse aggregate. The mix design of SCC have been shown in *Table* 3.9

Table 3.9 Typical SCC mix design as a control mix

Water	Cement	Slag	Aggregate		HRWRA
			Fine	Coarse	
kg./m^3	kg./m^3	kg./m^3	kg./m^3	kg./m^3	kg./m^3
172	400	90	910	750	1850

3.4 Preparation of ECC Specimens

3.4.1 Mixing Sequence

For the processing of fresh ECC, Hobart mixer of 20 liter capacity, equipped with planetary rotating blade was used (*Figure* 3.2). A programmed Excel sheet for mix design was used to

Hobart type mixer

Mixing of solid ingredients

Water addition

Fiber addition

Figure 3.2 Hobart type mixer

adjust and to calculate the amount of each of ingredients of concrete mixtures for each batch. Before mixing, all required materials were prepared and weighed as per batch requirements. A combination of small electrical scale and syringe was used to measure HRWRA.

The mixing procedure involves the following steps:

All the dry material i.e. cement, SCM (fly ash/ slag), aggregates, were added into drum and mixed at a speed of 100 rpm for 1 minute.

Water and super plasticizer was next added into dry material and mixed at 150 rpm for one minute and at 300 rpm for additional two minutes to produce consistent ECC matrix (without PVA fibers)

PVA fiber was added in last and mixed at 150 rpm for an additional three minutes.

3.4.2 Specimens

All the specimens were cast as per the guidelines for the concerned ASTM standard. Immediately after concrete mixing, to understand fresh properties slump flow test, slump flow time (T_{50} time), visual stability index and heat of hydration were conducted for each mix. Simultaneously, from each mixture, 50 mm cube and 355×50×76 mm prism specimens were prepared without any compaction or vibration for compressive strength and for four point bending tests, respectively. For the testing of durability properties 100×200 mm cylinder specimens were prepared for rapid chloride permeability, 50 mm cubes were cast to determine water absorption, water sorptivity and water porosity tests. 285×25×25 mm bar and 406×100x75 mm prism specimens were prepared for the testing of drying shrinkage and freeze and thaw testing respectively. For the accelerated reinforcement corrosion test 355×50×76 mm prism specimens were cast with having 12 mm diameter bar at the centre. All specimens were demolded at the age of 24 h, and cured in sealed plastic bag at 95±5% RH, 23±2 °C for 7 days. The specimens were then air cured at 50±5% RH, 23±2 °C until the age of 28 days for testing except for the freeze- thaw and drying shrinkage specimens. The specimens for the freeze-thaw test were cured in lime saturated water for 13 days after being demolded whereas specimens for the drying shrinkage were cured in lime saturated water for 27 days after being demolded.

3.5 Tests on Fresh Properties

Workability tests included the determination of slump flow, slump flow time (T_{50} time), visual stability index and heat of hydration.

3.5.1 Slump Flow

Slump flow is a simple test to observe the fluidity of ECC and to evaluate the deformability of the mix. A standard slump cone is used for the test where the concrete is poured in the cone without consolidation. Unlike the standard slump test, the diameter of the materials is measured after removal of the cone to characterize the flowability of the concrete, hence the name slump flow. The test can also be used as a visual inspection for segregation. This is observed by the flow characteristics of the mortar and fluid of paste separation. Usually, the range of the slump flow is from (450- 600 mm) to make the ECC self-consolidating and flowable without any kind of vibration. The slump flow test was performed in conjunction the ASTM C1611 (2009). The

Figure 3.3 Slump flow test

apparatus involved during the test include a regular slump cone, as well as a steel plate measuring 900 mm by 900 mm square. A sample of freshly mixed concrete was placed in a slump cone either in the upright or inverted position. The concrete was placed in one lift without consolidation. The mold was raised, and the concrete was allowed to spread. After spreading ceased, two diameters of the concrete mass were measured in approximately orthogonal directions (*Figure* 3.3). Slump flow was the average of the two diameters.

Calculation for the flow rate was carried out based on the duration of time it requires for the concrete to reach a diameter of 500 mm. Flow rate (T50 time) was also noted during the test with

the help of stopwatch. Although not mandatory, the appendix of the ASTM C1611 (2009) standard test method for slump flow measurement outlines a procedure that can be used for the relative measurement of the properties of ECC mix. Based on these guidelines, the visual stability index was measured.

3.5.2 Setting Time

Setting time for all the ECC mixes were performed in accordance of ASTM C403 (2008). For the evaluation of setting time the penetration resistance of needle was observed at regular interval of time as prescribed in ASTM C403. This resistance was plotted against time and with the help of this graph corresponding time was obtained for the needle penetration resistance of 3.445 MPa and 27.56 MPa. This time is referred as initial setting time and final setting time, respectively.

3.5.3 Heat of Hydration

The hydration reaction of cement is an exothermic process. The total heat released during hydration is a function of the composition of cementitious materials, amount of cementitious materials, and the water-binder ratio of the mixture. Measurement of the heat of hydration of hydraulic cementitious materials was performed using isothermal conduction calorimetry as per the ASTM C1679 (2009). The concrete was mixed outside calorimetry and then the mix was loaded into the apparatus. Care was taken that all the materials used for the concrete mix was at the temperature $23 \pm 2^{\circ}C$. After mixing the concrete the same was placed in the apparatus within 5 min., the reading was taken continuously for 72 hours with the help of data acquisition system connected with the apparatus. Figure 3.3 shows the setup for the heat of hydration test.

Figure 3.4 Heat of hydration test setup

3.6 Tests on Mechanical Properties

Performance of the hardened concrete was measured for all concrete batches by means of compressive strength and flexural strength. It should be noted that the concrete specimen were cast without any mechanical vibration or compaction energy. At least three specimens were tested for each of the hardened properties at standard ages.

3.6.1 Compressive Strength

Performance of hardened concrete was measured for all concrete mixes by means of compressive strength at the age of 7 and 28 day. The average compressive strength was obtained from 50 mm cube specimens for each mix at each age. Minimum of three specimens were prepared for any given mix and for any given age. The compression machine had a capacity of 1780 kN Medium failure load; range 3 (up to 356 kN) was used for all cubes as per ASTM C109/C109 M (2011b).

3.6.2 Flexural Strength

To measure the flexural strength (Modulus of rupture) of concrete, a four-point bending test was performed under displacement control condition at a loading rate of 0.005 mm/s on a closed-loop controlled servo-hydraulic material test system. Flexural strengths of the concrete were tested at three different ages - 7, 28 and 56 days. Minimum of three 355×76×50 mm prism specimens were prepared for a particular age. The span length of flexural loading was 304.8 mm with a 101.6 mm center span length. During the flexural tests, the load and the mid-span deflection were recorded on a computerized data recording system. To find the flexural strength of the beam the following equation 3.1 was used.

$$R = \frac{PL}{bd^2} \qquad (3.1)$$

Where, R = Flexural strength (modulus of rupture), MPa, P = maximum applied load indicated by the testing machine, kN, L = span length, mm, b = average width of specimen, mm, at the fracture, and d = average depth of specimen, mm, at the fracture.

3.7 Tests on Durability Properties

Out of all these ten trial mixes, the mixes showing the best mechanical properties were selected for the determination of durability properties. Based on these criteria three mixes were chosen for the durability properties testing.

3.7.1 Rapid Chloride Ion Penetration Test

The test was conducted in accordance with ASTM C1202 (2012). This test measures the ease with which concrete allows the charge to pass through and gives an indication of the ECC resistance to chloride-ion penetration. 100 mm in diameter and 50 mm in thickness disc specimens were cut from mid portion of Ø100 × 200 cylinder specimens and conditioned according to the ASTM C 1202 (2012) standard. Specimens

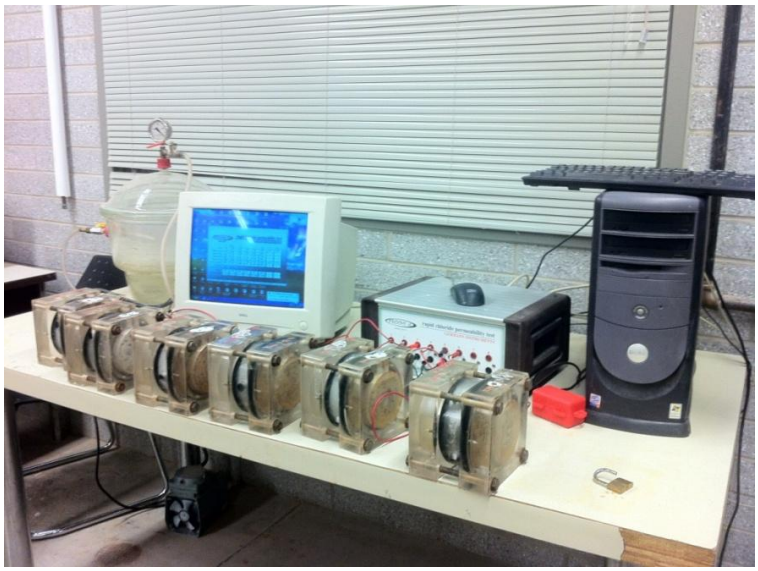

Figure 3.5 Rapid chloride ion penetration test setup

were subjected to 60-V potential for 6 h and total charge that passed through the concrete specimens was determined and used to evaluate the chloride penetrability of each ECC mixture. Minimum three specimens were test for each mixture.

3.7.2 Drying Shrinkage Test

The drying shrinkage of bar specimens was measured up to 120 days after an initial curing of one day in the mould and 27 days in lime saturated water by using three 285×50×50 mm prismatic specimens in accordance with ASTM C157 (2008) for all ECC mixtures (Figure 3.6). Gauge studs were inserted in the bar moulds coaxial with the bar before the ECC mixtures was poured in to the moulds. The drying shrinkage specimens were stored in laboratory at 23±2^{o} C, and 50±5% relative humidity.

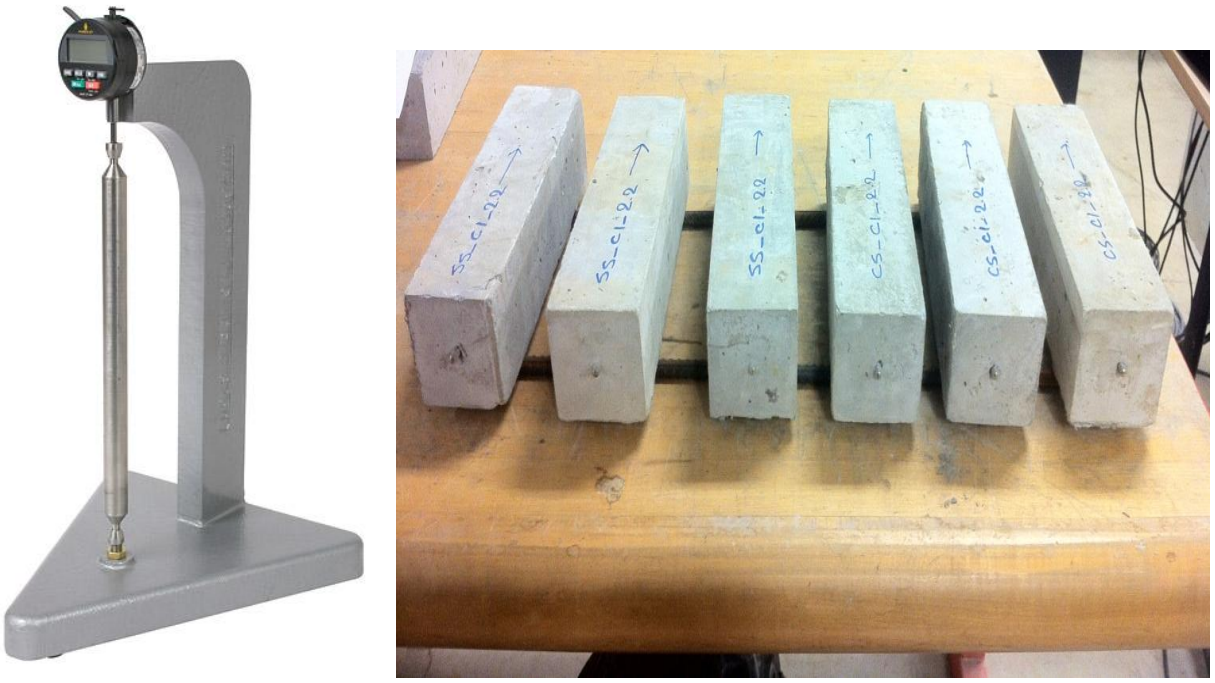

Figure 3.6 Drying shrinkage device and samples

3.7.3 Rapid Freeze-Thaw Test

To evaluate the freeze-thaw durability of ECC, freeze-thaw testing in accordance with ASTM C666 (2008) Procedure A was conducted. The mass loss, pulse velocity change, and flexural parameters (ultimate deflection and flexural strength) of specimens subjected to freeze and thaw cycles were determined. Normally, ASTM C666 specifies the use of the resonant frequency method, not the pulse velocity method. However, previous studies have shown that pulse velocity test method can also be used to measure the deterioration of specimens during freeze-thaw cycles.

From each mixture, six 400x100x75 mm^3 prisms were prepared for the freeze-thaw test. All specimens were cast in one layer without any compaction, demolded at the age of 24 h, and moist cured in lime-saturated water at 23$\pm$2°C for 13 days. Fourteen days after casting, the beam specimens were moved into the freeze-thaw chamber and subjected to between five and six freeze-thaw cycles in a 24 h period in accordance with ASTM C666 Procedure A (2008). The average flexural parameters (ultimate deflection and flexural strength) of the specimens were obtained by testing two companion samples prior to the freeze-thaw cycles. Changes in pulse velocity and mass loss were measured at each interval of nominally 30 cycles of freeze-thaw. At

the end of 300 freeze-thaw cycles, all the specimens were tested under four-point bending load with a span length of 355 mm and a height of 75 mm to determine their residual flexural performances, and their load-deflection curves were recorded. Three freeze-thaw specimens were tested for each mixture.

Figure 3.7 ECC specimens in the freeze-thaw test apparatus chamber

3.7.4 Water Absorption and Porosity Test

The water absorption was determined as per ASTM C642 (2006). The specimens were initially oven dried at 105 ± 5^{o}C for 72 h to reach constant mass to obtain the oven dry mass (W_1). They were then immersed in water for 72 h and the saturated surface dry mass (W_2) of the specimens was measured. The water absorption (WA) of the each specimen was calculated as follows:

$$WA\,(\%) = \left(\frac{W_2 - W_1}{W_1} \right) \times 100 \qquad (3.2)$$

To determine the water porosity, hydrostatic weight (W_3) of ECC specimens were also determined and water porosity was calculated as follows:

$$WP(\%) = \left(\frac{W2 - W1}{W2 - W3} \right) \times 100 \qquad (3.3)$$

3.7.5 Sorptivity Test

The sorptivity test evaluates the increase in mass of a cube specimen (50×50×50 mm) at given intervals of time (up to 360 min for initial sorptivity and up to eight days for secondary sorptivity) when permitted to absorb water by capillary suction. Only the bottom surface of the specimen was allowed to be in contact with water with the depth of water up to 4 mm, to prevent water ingress from other sides, perimeter and top surface of specimens sealed with adhesive aluminum tape. This test was chosen as it measures the rate of ingress of water through unsaturated concrete. Therefore, it can be considered a measure of water transport associated with capillary suction. Three specimens were used to determine the ingress of water for each ECC mixture. The curing of the specimen was performed in the same way as it was performed for other specimens. It was specifically performed in this way to understand capillary suction effect in the normal condition.

3.7.6 Accelerated Reinforcement Corrosion Test

From each mixture, 355 x 76 x 50 mm prism specimens with a centrally placed deformed steel bar that had a 12 mm diameter (No. 4, Grade 60, ASTM A615 (2012)) and a length of 600 mm were prepared for the accelerated corrosion test. Steel bars were cleaned with a wire brush to remove any rust from the surface just before casting the reinforced specimens. At the air/mortar interface, the steel bars were coated with epoxy glue to avoid crevice corrosion. All specimens were demolded at 24 hours and moisture-cured in plastic bags at 95 ± 5% relative humidity (RH) and 23 ± 2 °C (73 °F) for 7 days. The prism specimens were then air-cured in laboratory medium at 50 ± 5% RH and 23 ± 2 °C (73 °F) until 28 days for testing.

An accelerated reinforcement corrosion testing technique was used to compare the corrosion performance of ECC. At the end of 28 days, the ECC prism specimens with a centrally placed steel bar were partially immersed in a 5% NaCl solution, as shown in Figure 3.8 The exposed steel bar was then connected to the positive terminal of a DC power source while the negative terminal was connected to stainless steel plates placed near the specimen in the solution. The weight of the steel bar was measured and recorded for weight loss measurement before accelerated reinforcement corrosion test. The corrosion process was initiated by applying a

constant 30 V anodic potential. High voltage was used to accelerate the corrosion and shorten the test period. The test was conducted for 300 hr of accelerated reinforcement corrosion.

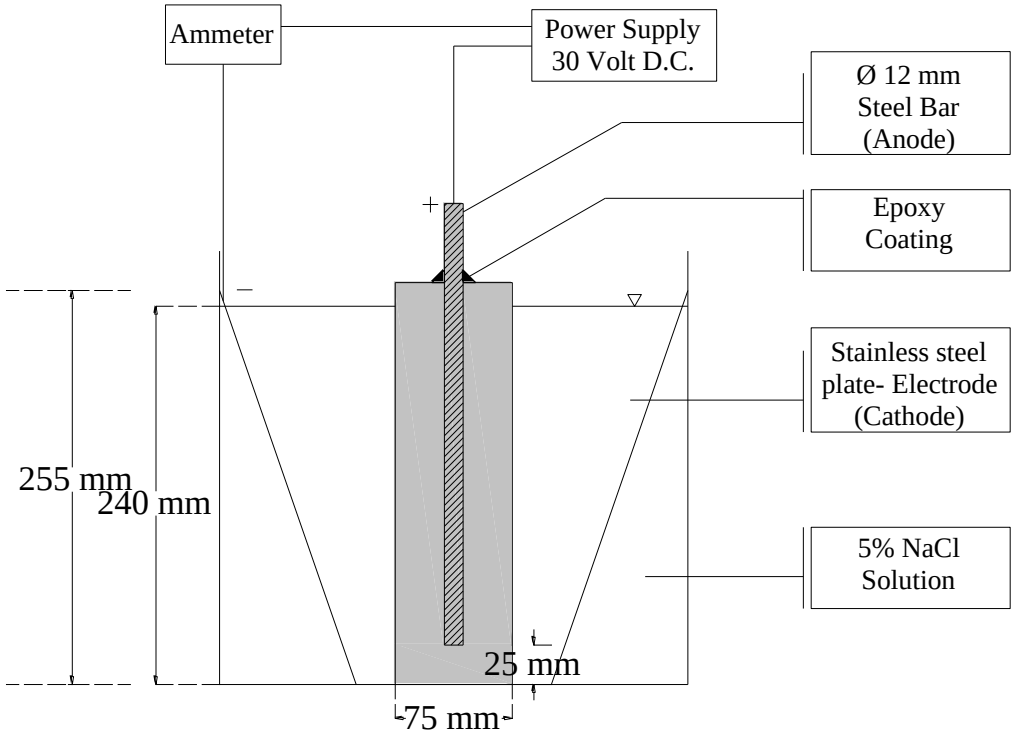

Figure 3.8 Corrosion test setup

The samples were visually inspected for cracks daily while the current flow was continuously monitored. The current would increase suddenly whenever the specimen cracked. The widths of the crack were also measured regularly on the surface of the specimens by an optical microscope.

The 28-day residual flexural load was determined by performing a four-point bending test under displacement control condition at a loading rate of 0.005 mm/s on a closed-loop controlled servo-hydraulic material test system, ECC with a 50 x 75 mm cross section, 355 mm in length, a support span length of 325 mm, and a center span length of 108 mm were tested in a closed-loop machine after having been exposed to different degrees of accelerated corrosion. In each case, two replica specimens were loaded until failure to determine their load-deflection curves and ultimate flexural load capacity. Two control prisms of each mixture without accelerated corrosion exposure were also tested after 28 days.

3.8 Summary

This chapter describes the material properties of cement, different SCMs, aggregate, water and fiber. This has been followed by descriptions of different test methods for testing fresh, mechanical and durability properties of ECC.

CHAPTER FOUR

FRESH AND MECHANICAL PROPERTIES

4.1 Introduction

This chapter describes the results of fresh and mechanical properties of ECC mixtures obtained by following the test procedures mentioned in Chapter 3. A brief discussion and the effect of various material and other factors affecting the properties of ECC mixtures are also included.

4.2 Slump Flow, Flow Time and Visible Stability Index (VSI)

Observed slump flow, flow time and visual stability index (VSI) has been listed in Table 4.1. The diameter of the slump flow is the recorded average of orthogonal axis through the center of the slump flow. The test was performed on a smooth dampened metal plate and all the equipments in contact with the concrete were dampened to avoid any removal of water from fresh concrete.

Table 4.1 Slump flow, flow time and visual stability index of ECC mixes.

Mix No.	Mix Designation	Slump Flow mm	Flow Time (T_{50}) Sec	Visual Stability Index(VSI)
1	SS_CI_1.2	540	2.54	0
2	SS_CI_2.2	530	2.98	0
3	SS_SL_1.2	475	1.58	0
4	SS_SL_2.2	485	N.A.	0
5	SS_F_1.2	550	N.A.	0
6	SS_F_2.2	530	2.83	0
7	CS_CI_1.2	520	3.43	0
8	CS_CI_2.2	500	3.11	0
9	CS_F_1.2	530	3.29	0
10	CS_F_2.2	515	3.09	0

* Mix Designation: CS represents Crushed Sand, F represents FA class F and 1.2 represents SCM/cement replacement ratio

The average slump flow for all ECC mixes with class CI FA was between 500 mm and 540 mm whereas for the mixes with class F FA, the slump flow of the mixes ranged between 515 mm and 550 mm. While obtaining fresh properties of mixes with slag there was an issue encountered. At the same water to binder ratio (w/b) and same HRWRA content, mixes with slag showed less

slump flow compared to the mixes with fly ash. When the effort was made to increase the slump flow by increasing HRWRA, the mixes with the slag showed signs of bleeding. In other words, mixes with slag was more sensitive to HRWRA content and prone to bleeding more rapidly than other mixes.

In order to make the mix stable, workability was compromised in the case of mixes with slag. The slump flow for slag ECC mixes was ranging between 470 and 485 mm. Because of this reason, flow time was not possible to measure.

All the mixes with fly ash, irrespective of their types showed excellent workability and no signs of bleeding. All the mixes were designated VSI as 0 as a highly stable mix without any type of bleeding or segregation. As such, segregation was not particularly applicable as coarse aggregate was not there in the matrix. It was observed that excess quantity of HRWRA was resulting into the balling of fibers after separating from matrix. This phenomenon could be considered as segregation in terms of ECC. And for this reason, the HRWRA content was limited to such an amount that would maintain the homogeneity of the mix.

4.3 Heat of Hydration

The heat of hydration is one of the important parameter of fresh property to understand the thermal behaviour of ECC. Thermal curves are used to evaluate the heat of hydration of the combined mixture of different materials during early age after the contact with water. These isothermal curves, or hydration profiles, may provide indications relative to setting characteristics, compatibility of different materials, sulfate balance and early strength development. The isothermal hydration profiles can also be used to evaluate the effects of compositions, proportions, and time of addition of materials as well as curing temperature.

Test results in terms of maximum hydration pick along with time are tabulated in Table 4.2. Hydration profile of different mixes obtained in accordance with ASTM 1679 (2009) are shown in Figure 4.1a-b. To facilitate the comparison between the test results for different ECC mixtures, the same scales for both axes were used in these figures.

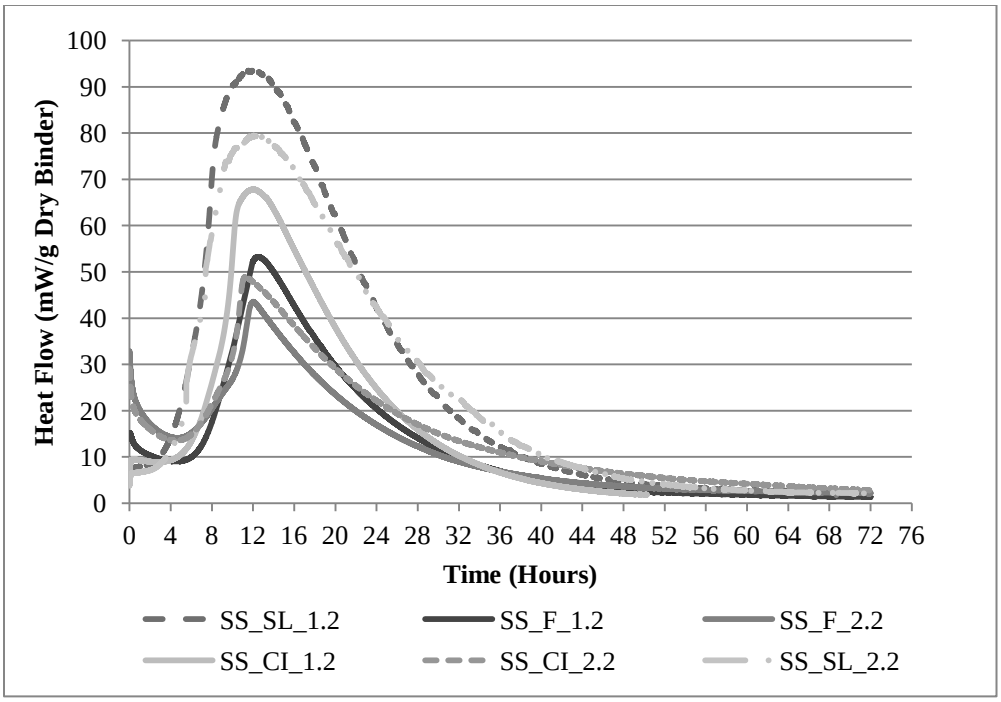

(a) mixes with microsilica sand

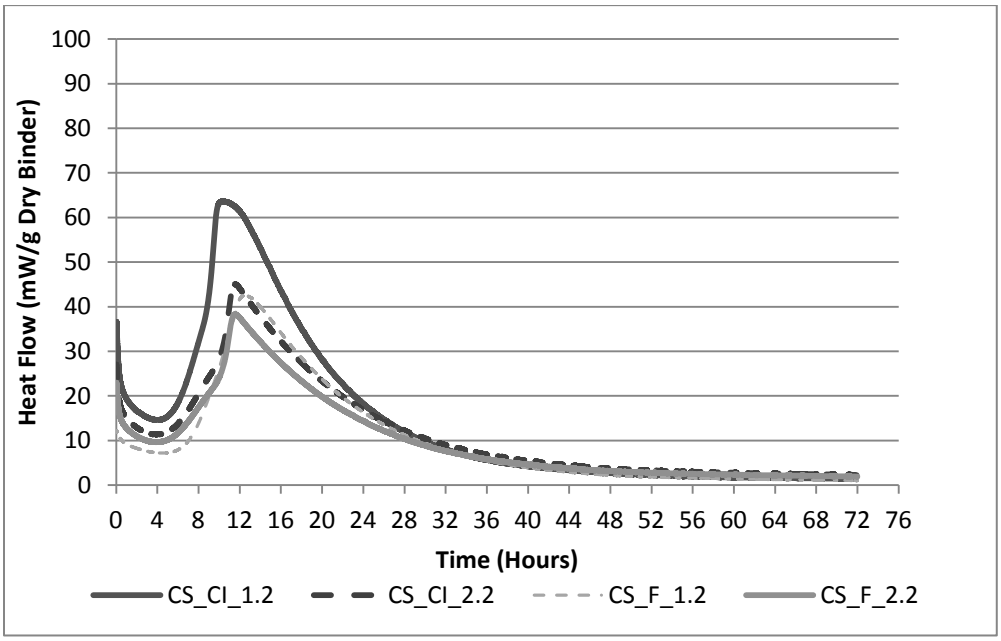

(b) mixes with crushed sand

Figure 4.1 Variation of heat of hydration of different mixes

Table 4.2 Hydration peak with corresponding time and setting time for ECC mixes

Mix No.	Mix Designation	Value at hydration peak	Duration to reach maximum hydration	Initial Setting Time	Final Setting Time
		(mW/g dry Binder)	(min)	(min)	(min)
1	SS_CI_1.2	67.74	711	232	332
2	SS_CI_2.2	48.53	664	249	356
3	SS_SL_1.2	63.24	559	196	280
4	SS_SL_2.2	44.59	680	212	303
5	SS_F_1.2	93.40	696	244	348
6	SS_F_2.2	79.32	729	256	365
7	CS_CI_1.2	53.04	734	249	355
8	CS_CI_2.2	43.02	709	257	367
9	CS_F_1.2	42.30	731	245	350
10	CS_F_2.2	37.75	679	256	366

As shown in Figure 4.1a-b, there was a significant effect of type and volume of supplementary cementitious material on the hydration curves of ECC mixes. Among all mixes SL-ECC showed highest amount of hydration which was followed by class CI FA and lowest was observed for class F FA ECC. The reason behind this phenomenon can be attributed to the CaO content of different SCMs which was chemically reacting with water and creating $Ca(OH)_2$ and releasing heat during this process. Slag having highest amount of CaO showed highest amount of hydration and FA class F showed lowest. Higher replacement of any SCM (70% of cement replacement) resulted in total decrease in free CaO of the mix (as CaO in Portland cement is higher than any SCM CaO content) and so as lowering of hydration peak. Use of fly ash as SCM delayed the time to reach maximum hydration. Slower reactivity of fly ash particles could be the reason for this delay.

In terms of the effect of the aggregate type, mixes with microsilica sand showed slight higher hydration peak than the corresponding mix with crushed sand. Microsilica sand is amorphous in nature and may contain some crystalline silica in the form of quartz or cristobalite. The higher surface area and amorphous nature of microsilica sand make it highly reactive. The hydration of C3S, C2S, and C4AF are accelerated in the presence of microsilica sand (Kurdowski and Nocun-Wczelik, 1983; Uchikawa an Uchida, 1980). For this reason the microsilica sand mixes showed slightly higher hydration peak than corresponding crushed sand mixes.

4.4 Setting Time

The setting time of all the mixes was obtained in accordance with ASTM C403 (2008). Results for initial setting time and final setting time are shown in Table 4.2 As predicted slag-ECC showed the lowest initial and final setting time. Class F FA mixes showed the highest initial and final setting time whereas mixes with class CI FA showed slightly lower setting time than class F FA. Higher CaO content of slag made the setting time process faster whereas due to slower reactivity of fly ash particles delayed setting time process. Higher replacement of SCM slower the process and setting time was increased.

Larger surface area and higher reactivity of microsilica sand resulted in slightly faster setting of concrete which in turn lowered setting time of mixes with microsilica sand compared to corresponding mixes with crushed sand.

4.5 Compressive Strength

Compressive strength tests were performed at 7 and 28 days of age. Three cube specimens were tested at each age for each mixture. As seen from Table 4.3 and as expected, at the same replacement level, especially at early age, the slag produced significantly greater strengths than the FA (CI or F). The greatest difference was observed at 7 days for the replacement level of 2.2 (70% replacement), where the SS_SL_(1.2 or 2.2) specimens achieved more than 70% higher compressive strengths than those respective mixes containing FA. The reason behind this observation was the slower activity of FA compared to slag (Sahmaran et al., 2009). All the mixtures, however, showed compressive strengths higher than 45 MPa at 28 days of age. This value significantly exceeds that of normal concrete strength (30 MPa), and fulfill engineering requirements in most projects.

Out of these three SCMs, compressive strengths of mixes incorporating slag were higher than those mixes incorporating FA (CI or F). Incorporation of slag into the matrix improved the bond between the cement paste and aggregate particles as well as increasing the density of the cement paste which in turn significantly improves the compressive strength of ECC mixtures. In the same way, higher Calcium Oxide CaO content of FA CI is responsible for obtaining higher

Table 4.3 Compressive strength of ECC mix

Mix No.	Mix Designation*	Compressive Strength (MPa)	
		7*d*	28*d*
1	SS_CI_1.2	27.15	62.43
2	SS_CI_2.2	26.74	52.80
3	SS_SL_1.2	30.82	73.11
4	SS_SL_2.2	28.55	69.78
5	SS_F_1.2	26.18	46.38
6	SS_F_2.2	25.52	45.29
7	CS_CI_1.2	26.18	60.39
8	CS_CI_2.2	25.52	47.30
9	CS_F_1.2	28.80	58.63
10	CS_F_2.2	24.24	45.34

compressive strength of mixes with class CI FA compared to class F FA. Simultaneously, as the amount of SCM increases and cement decreases, the compressive strength decreases as well. This is due to lower CaO% available for the hydration process compared to the cement. That is the reason why, the mixes with higher SCM content showed slightly lower compressive strength than the lower SCM content mixes.

At each SCM replacement level, ECC mixtures with microsilica sand (e.g. SS_CI_1.2, SS_CI_2.2, SS_F_1.2 and SS_F_2.2) yielded slightly higher compressive strengths than those with crushed sand (CS_CI_1.2, CS_CI_2.2, CS_F_1.2 and CS_F_2.2). In the case of normal concrete, because the surface texture is partly responsible for the bond between paste and aggregate, the crushed sand is expected to produce a better bond between paste and aggregate, and therefore higher compressive strength compared with microsilica sand. However, as seen from Table 4.3, crushed sand produced almost similar or slightly lower compressive strengths than that for ECC mixtures with microsilica sand. Therefore, unlike conventional concrete, aggregate characteristics, such as the surface texture and maximum aggregate size, did not influence the compressive properties in the case ECC. In general, everything else being the same, the larger the aggregate size, the higher the local w/b in the interfacial transition zone and, consequently, the weaker the concrete (Mehta & Monteiro, 2006).

4.6 Flexural Performance (Modulus of Rupture)

The direct tensile test is considered to be the most accurate and effective method to confirm the strain-hardening behaviour of a composite, as quasi-brittle fiber reinforced composites can potentially show apparent strain-hardening behaviour under flexural loading, depending on the specimen geometry. However, one of the major concerns in designing concrete structures or to study the structural performance is the flexural performance of the concrete. Flexural strength test of ECC is also an indirect measure of direct tensile performance. Therefore, it was decided to use the four-point bending test to investigate the flexural strength and ductility (by measuring mid-span beam deflection capacity) of ECC mixtures. Previous studies also demonstrated that the deflection capacity can be correlated with the tensile strain capacity when the material showed truly strain hardening behaviour (Qian and Li, 2007; Qian and Li, 2008).

The test results in terms of flexural strength (modulus of rupture – MOR) and ultimate mid-span deflection at the peak stress are displayed in Table 4.4, and the typical flexural stress-mid-span deflection curves for different aggregate amounts of the ECC mixtures are shown in Figure 4.2. To facilitate the comparison between the test results for different ECC mixtures, the same scales for both axes were used in these figures. In the flexural load–deflection curves, the maximum

Table 4.4 Flexural properties of different ECC mix

Mix Designation	Flexural Strength (MPa)			Deflection (mm)			Crack Width (μm)			Number of Cracks		
	7d	28 d	56 d	7 d	28 d	56 d	7 d	28 d	56 d	7 d	28 d	56 d
SS_CI_1.2	9.74	12.17	13.63	4.38	4.17	3.96	≤ 50	≤ 50	≤ 50	16	11	7
SS_CI_2.2	9.4	11.73	13.16	4.55	4.33	4.11	≤ 50	≤ 50	≤ 50	56	49	20
SS_SL_1.2	12.4	15.37	17.36	2.1	2	1.9	≤ 90	≤ 90	≤ 90	12	5	2
SS_SL_2.2	12	15	16.8	2.1	2	1.9	≤ 90	≤ 90	≤ 90	21	13	6
SS_F_1.2	9.37	11.71	13.12	4.74	4.51	4.28	≤ 50	≤ 50	≤ 50	18	21	20
SS_F_2.2	8.8	11	12.32	4.79	4.56	4.33	≤ 50	≤ 50	≤ 50	54	54	40
CS_CI_1.2	9.2	11.5	12.88	4.17	3.97	3.77	≤ 50	≤ 50	≤ 50	23	12	18
CS_CI_2.2	8.8	11	12.32	4.46	4.25	4.04	≤ 50	≤ 50	≤ 50	40	42	19
CS_F_1.2	9	11.26	12.6	4.48	4.27	4.06	≤ 50	≤ 50	≤ 50	25	19	23
CS_F_2.2	8.4	10.57	11.76	4.73	4.5	4.28	≤ 50	≤ 50	≤ 50	48	52	30

stress is defined as the flexural strength (modulus of rupture), and the corresponding deflection is defined as the flexural deflection (mid-span beam deflection) capacity. The flexural

performances of ECC mixtures were obtained by averaging the results of at least three or more four-point bending measurements. It is important to note that the coefficient of variation of the flexural strength test results within each mix design is lower than 10%.

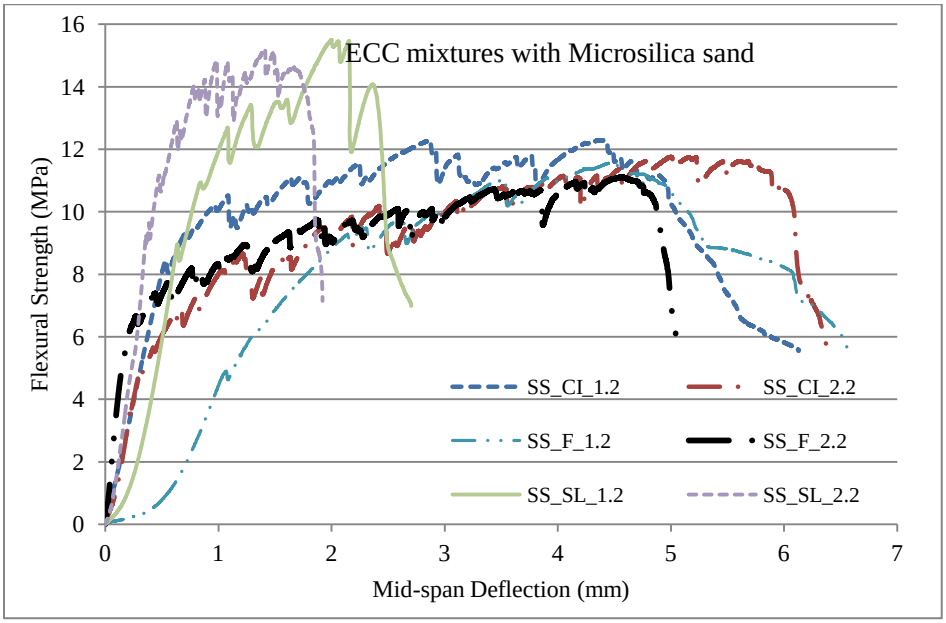

(a) ECC mixtures with micro silica sand

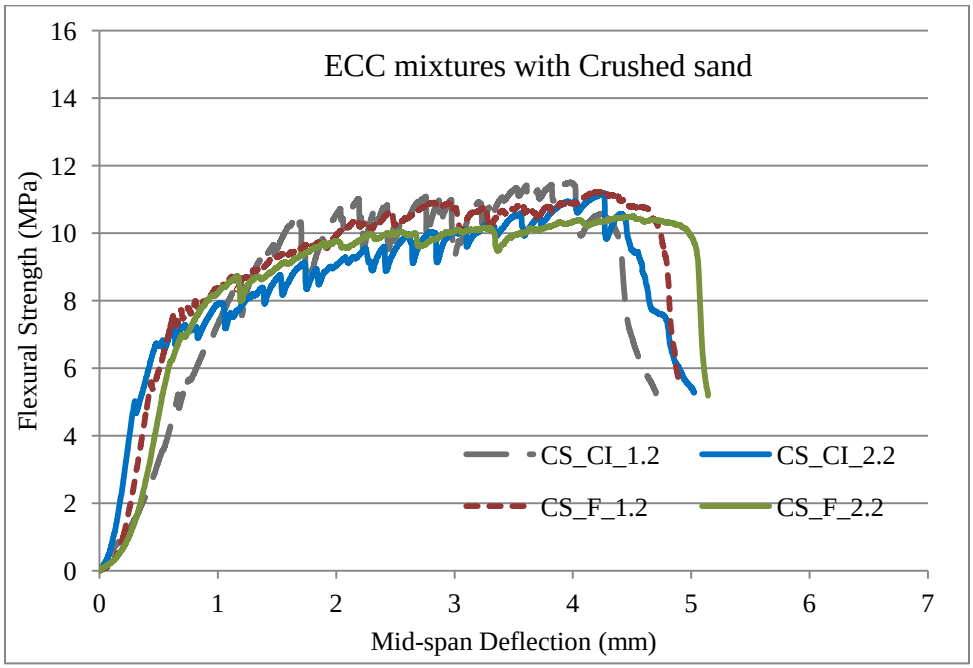

(b) ECC mixtures with crushed sand

Figure 4.2 Flexural strength vs. mid-span deflection

4.6.1 Load-Deflection Curves

Typical load deflection curves for PVA-ECC incorporating 2% volume fraction of PVA fibers, different type of aggregates and different types of SCMs are presented in Figure 4.2. As seen in Figure 4.3, under severe bending load, an ECC beam containing fly ash as SCM irrespective of their aggregate type deforms similarly to a ductile metal plate through plastic deformation.

Each specimen was examined using a portable microscope during and after the loading to determine the crack width and distribution. In all ECC specimens, the first cracks to appear were flexural cracks starting at the surface of the tension face. After the first cracking, the load continued to rise accompanied by multiple micro-cracking, which contributed to the inelastic deformation as stress increases. Shortly after the initial cracking, the crack width grew rapidly with an increase of deformation, and then stabilizes at a value between 40 to 90 μm while additional micro-cracks further develop. Micro-cracks developed from the first cracking point and spread out in the mid-span of the flexural beam as shown in Figure 4.3. The bending failure in ECC occurred when the fiber bridging strength at one of the micro-cracks was reached; resulting in localized deformation at this section (Figure 4.3) once the flexural strength is approached.

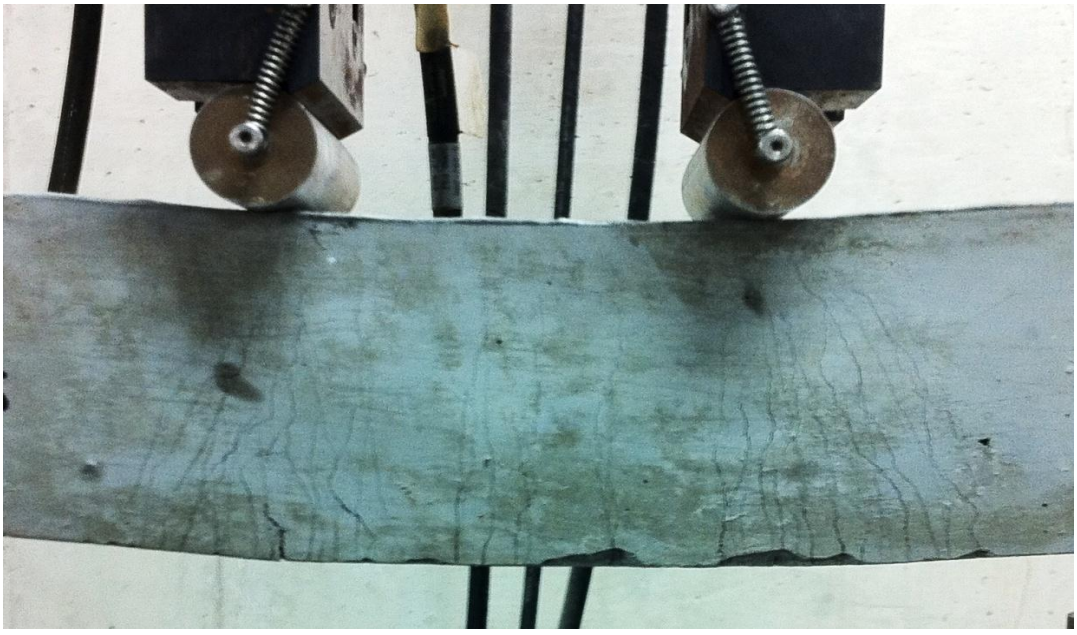

Figure 4.3 Typical cracking patterns of ECC beam specimen after flexure load applications (Mix ID.: CS_F_2.2)

The slope of the load-deflection curve represents the stiffness of the beams and it can be easily noted from Figure 4.2(a and b) that the slope increases significantly with replacement of slag, and thereby, indicating an increase in the stiffness of the SL-ECC beams. On the other hand, stiffness of the beams with both the FAs were in the same range, FA CI-ECC being slightly stiffer compared to FA F-ECC. This result is consistent with what is stated in the literature (Cetin and Carrasquillo, 1998; Baalbaki et al., 1991; Sahmaran et al., 2009). As can be seen, there was no apparent difference in slope and in turn stiffness of ECC mixtures when microsilica sand was replaced with crushed sand. Unlike conventional concrete and as shown in Figure 4.2, ECC with 0.4 or 1.19 mm maximum aggregate size had very similar stiffness for ECC mixtures containing same supplementary cementitious material (FA or slag). As a result, within the size range studied, elastic modulus appears to be independent of maximum aggregate size at a given aggregate content.

4.6.2 Flexural Strength (Modulus of Rupture - MOR)

Flexural strength of ECC specimens are summarized in Table 4.4. The average ultimate flexural strengths are found to vary from 10.57 to 15.37 MPa depending on the SCM content. As it is seen on Table 4.4, the increase of SCM/C ratio from 1.2 to 2.2 resulted in to the decrease of flexural strength. The specimens which contained slag developed slightly higher strength than specimens of identical cement replacement. It is apparent from the minor difference of the compressive strength test results, there is no significant influence of the FA CI or F replacement on the flexural strength values especially at the ages of 28 days or later in the tested range. For example, the flexural strength of ECC with FA CI/C ratio of 2.2 (SS_CI_2.2 and CS_CI_2.2) is about 95% that of the ECC mixtures with FA F/C ratio of 2.2(SS_F_2.2 and CS_F_2.2). This value is about 73% that of ECC mixtures with SL/C ratio of 2.2. The MOR is likely limited by the fiber bridging capacity governed by the fiber/matrix bond and in turn by the supplementary cementitious material replacement rate. However, even at about 70% replacement of cement by FA or slag (SCM/cement ratio of 2.2), the flexural strength of ECC at 28 days was significantly higher than that of conventional concrete and fiber reinforced concrete. Moreover, flexural strength increased with age more slowly than compressive strength.

Bending capacity (defined by mid-span deflection) of ECC specimens has been summarized in Table 4.4. The mid-span deflection of the ECC beams at peak bending load vary from 2.00 to

4.56 mm depending on the class CI, F FA or slag content. As it is seen in Table 4.4, the increase of SCM/C ratio from 1.2 to 2.2 improved the bending capacity of ECC mixtures while decreased flexural strength. The improvement in the bending capacity with the increase in the SCM content can be attributed to the fact that increase in the SCM content tends to reduce the PVA fiber/matrix interface chemical bond and matrix toughness, while increasing the interface frictional bond, in favor of attaining high bending capacity (Wang and Li, 2007; Sahmaran and Li, 2009a),. Moreover, flexural strength test results also showed that the load carrying capacity of ECC mixtures incorporated with class CI FA were slightly higher than those of the ECC mixtures which were produced with class F FA. However, mid-span beam deflection values of the ECC mixtures with class CI FA are slightly lower than that of the ECC mixtures incorporated with class F FA.

Unlike conventional concrete, ECC mixtures with crushed sand tend to have similar or vaguely less flexural strength and mid-span deflection compared to mixtures with microsilica sand. For example, the flexural strength of ECC mix CS_CI_2.2 is about 93.5% that of the ECC mixtures SS_CI_2.2. As in the case of compressive strength test results, the aggregate type and maximum aggregate size also had no or only a minor effect on the flexural strength. In the case of normal concrete, increasing aggregate size generally produces higher fracture energy and hence higher matrix toughness, (Perdikaris & Romeo, 1995) which in turn should reduce the ductility of ECC. The reason for similar range of ductility with crushed sand may be attributed to the use of high volumes of FA in the production of ECC (Sahmaran, et al., 2009). Specifically, the micromechanics study showed that the presence of FA reduced the fiber/matrix interfacial chemical bond while simultaneously lowering the matrix toughness, thus improving strain-hardening potential (Wang & Li, 2007). Another possible explanation is that a partial replacement of cement by FA results in a higher volume of paste at constant total weight of cementitious materials due to its lower density, and this increase in the paste volume reduces the friction at the fine aggregate-paste interface and improved the plasticity and cohesiveness (Sahmaran, et al., 2006; ACI Committee 232, 1994) this leads to a better distribution of the fibers in the mortar matrix. Moreover, the spherical shape of FA reduces the friction at the aggregate paste interface, producing a “hinging effect” at the point of contact, (Wei, et al., 2003; Okamura & Ouchi, 2003) which might also improve the distribution of fibers. As a result, ductility appears

to be independent of aggregate size at a given aggregate content, at least within the size range studied herein.

Mid-span deflection values of bending test signified that the most important feature of ECC, high ductility with multiple cracking behaviours, was protected and is not sacrificed by replacing cement with a maximum of 70% FAs and by replacing microsilica sand with crushed sand.

4.6.3 Crack Characterization

After performing the four point bending test, the bending load was released and specimens were taken out of the MTS machine. A crack closure occurred on unloading position and it was observed in this study that the width of a loaded crack was approximately 30% more than the width of the unloaded one. All crack width measurements were conducted in the unloaded stage. The widths of the crack were measured on the tension surface of the specimens by using a crack microscope. Table 4.4 also shows average crack widths and number of cracks of prism specimen. Each data point in Table 4.4 is an average of at least three or more prism specimens and more than 10 μm crack widths are measured from each specimen. All of the ECC mixtures show a crack width smaller than 100 μm. Among these mixtures SS_CI_2.2, SS_F_2.2, CS_CI_2.2 and CS_F_2.2 showed a very tight average crack width in the range of 40 to 50 μm. It was found that the number of crack increased and crack width reduced as fly ash content increased from 50% to 70%. Crack width appeared to be independent of the aggregate type used in the research. ECC mixtures (SS_SL_1.2 and SS_SL_2.2) incorporating slag lead to a slightly larger crack width and less number of cracks.

4.7 Summary

As seen in this chapter, all the mixes with fly ash showed clear signs of self flowability where slag-ECC showed moderate level of self-flowability. Slag-ECC obtained higher compressive strength compared to FA-ECC at all the corresponding ages. FA-ECC succeeded to show micro-cracking and strain hardening behaviour under flexural loading. Whereas in the case of Slag-ECC, cracks were less in numbers, crack opening were wide and flexural strength was higher compared with FA-ECC but ductility was compromised. Increasing the SCM/C ratio decreased compressive strength to some extent but ductility and number of microcracks increased. All the mixes with fly ash obtained moderately high compressive strength and showed enough flexural

strength and ductility. All the cracks after flexural strength test remained below 100 μm. There is no significant difference in behaviour in terms of fresh, compressive strength and flexural property while replacing fly ash CI with FA class F. As noted above there is fairly minor influence of aggregate type (crushed sand or silica sand) and aggregate size studied under this investigation on fresh and mechanical properties.

CHAPTER FIVE

DURABILITY PROPERTIES

5.1 Introduction

As discussed in the previous chapters, this research work was carried out specifically to design ECC mixes with suitable properties and validate its performance for the application in link slabs of bridge decks. Emphasize was given to the ECC mixes which are performing well in terms of strength, deflection and crack characteristics along with their fresh performance. Out of ten developed mixes, best three mixes were based on their performance in terms of flexural strength, micro-cracking behaviour, and deflection. These mixes are considered to be used in link slab to provide better structural performance and resistance against severe environmental exposure. Therefore, it was important to test these mixes for the durability properties and to see whether they are performing satisfactorily or not. The results of the durability properties tests of selected three ECC mixes (Table 5.1, using class CI or F FA and silica sand (SS) or crushed sand (CS)) are presented and discussed in this chapter.

Table 5.1 Mix design of best three mixes.

	ECC Mix Designation		
Ingredients	SS_CI_2.2*	CS_CI_2.2	SS_F_2.2*
Water (W), kg/m^3	327	318	327
Cement (C), kg/m^3	386	375	386
Fly ash CI, kg/m^3	847	825	-
FA class F, kg/m^3	-	-	847
Microsilica Sand(SS), kg/m^3	448	-	448
Crushed Sand(CS), kg/m^3	-	436	-
Fiber (PVA), kg/m^3	26	26	26
HRWRA, kg/m^3	3.9	4.2	3.7
CI/C	2.2	2.2	-
F/C	-	-	2.2
Cement Replacement by SCM	70%	70%	70%
W/B	0.27	0.27	0.27

5.2 Rapid Chloride Ion Penetration Resistance

Rapid chloride ion penetration test results of the selected ECC mixtures and their chloride ion rating according to ASTM C 1202 (2012) are presented in Table 5.2. The test was performed in accordance with ASTM C1202 (2012).

Table 5.2 Rapid chloride ion permeability test results

Mix Designation	Coulombs	Rating
SS_CI_2.2	1893	Low
CS_CI_2.2	1922	Low
SS_F_2.2	1747	Low

The ECC sample is subjected to a potential difference of 60 V and the total charge passing through sample at the end of 6 h is measured and expressed in terms of Coulombs. A reduction in this total charge value indicates a better resistance to chloride ion penetration and lower permeability (Sengul et al., 2002). As seen in the table, replacement of microsilica sand with crushed sand (SS_CI_2.2 to CS_CI_2.2) reduced the resistance to chloride ion penetration of ECC. Being this difference very small and both the ECC mixtures being in the same rating zone, the difference can be considered to be negligible. In other words, unlike conventional concrete, aggregate characteristics, such as the surface texture and maximum aggregate size, did not influence the resistance to chloride ion in the case of these ECCs.

From Table 5.2, it can be seen that the replacement of class F FA with class CI FA slightly reduced the resistance to chloride ion penetration of ECC. This result is completely opposite to the findings of the previous researches performed on mortar and concrete. Normally, concretes with high volumes of pozzolanas have lower chloride ion permeability due to the result of a denser microstructure. The pozzolanic reaction may cause lower amount of capillary pores and clogging of the pores, which reduces chloride ion transport in concrete (Li and Roy, 1986). Also it was mentioned in the literature that fineness of pozzolanas has a great influence on the chloride ion permeability, high fineness which may have contributed to obtaining lower chloride ion permeability (Zhang et al., 1999). However, as mentioned by Sahmaran and Li (2009a), the trend in ECC is completely different from those of the mortar and concrete. As seen in Table 5.2, replacing class F FA with class CI FA increased chloride ion permeability of ECC just by 9%. The possible reason behind higher chloride penetration with replacement of class F FA by class

CI FA can be that ECC specimens were cured in air after a 7-day sealed curing, and because of lack of curing, most of the FA particles in the matrix remain without any chemical reaction. Since SS_CI_2.2 has more pozzolanas than SS_F_2.2, it has been somewhat more negatively affected by the lack of curing. The benefits of using class F FA in concrete in terms of improved durability properties such as chloride ion penetration resistance is usually manifested at later ages with the continuous supply of moisture (Sahmaran and Li, 2009a). Other possible reason can be attributed to the fineness of fly ash; class F FA is finer and denser than class CI FA. For this reason, the use of class F FA could have resulted in to somewhat more dense and clogged structure than class CI FA and in turn lower chloride ion permeability.

5.3 Drying Shrinkage

This section presents the results of the drying shrinkage tests. The effects of maximum aggregate size, aggregate type, and mineral admixture type on the shrinkage of ECC mixtures are evaluated with the goal of establishing guidelines to reduce cracking in ECC. The drying shrinkage specimens were stored in a controlled environment at 23 ± 2°C and 50 ± 4 percent relative humidity, and drying shrinkage was recorded as the change in length over a gage length (distance between tips of gage studs) of 254 mm up to a period of 120 days. The results of drying shrinkage test at the age of 120 days are shown in Figure 5.1. Each value in Figure 5.1 represents the average drying shrinkage measurements of three specimens.

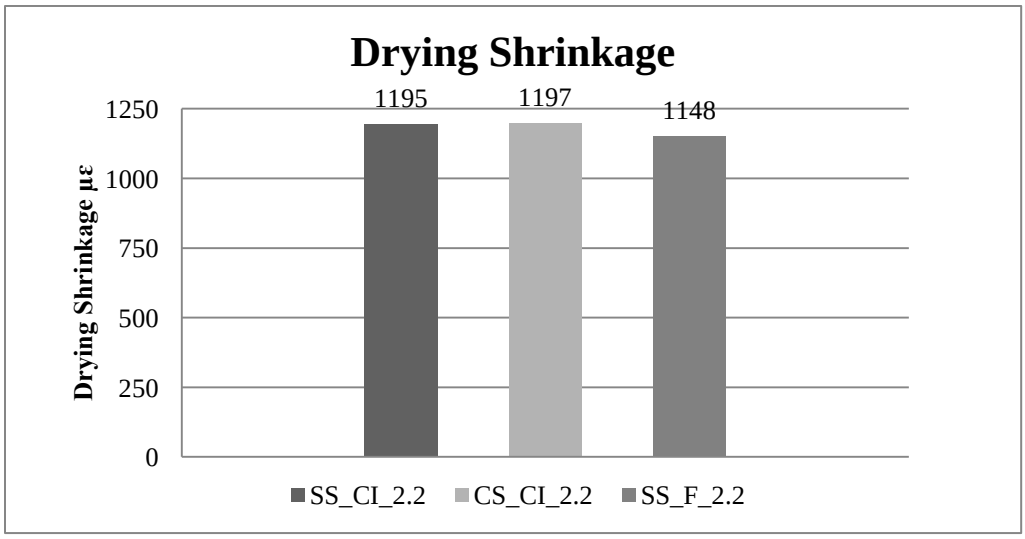

Figure 5.1 Drying shrinkage of ECC mixtures at 120 days

The drying shrinkage strains at the age of 120 days ranged between 1148 and 1197 micro-strain. Although among all mixtures highest amount of drying shrinkage of 1197 micro strain at the age of 120 days was observed with class CI FA and maximum aggregate size of 1.19 mm i.e. crushed sand (CS_CI_2.2), this result lies in the same range of the ECC mix SS_CI_2.2 (i.e. microsilica sand) of 1195 micro strain. The only difference between these two mixes was the aggregate type and aggregate size. This provided the evidence that the drying shrinkage is merely affected by the aggregate type and aggregate size considered under this research work.

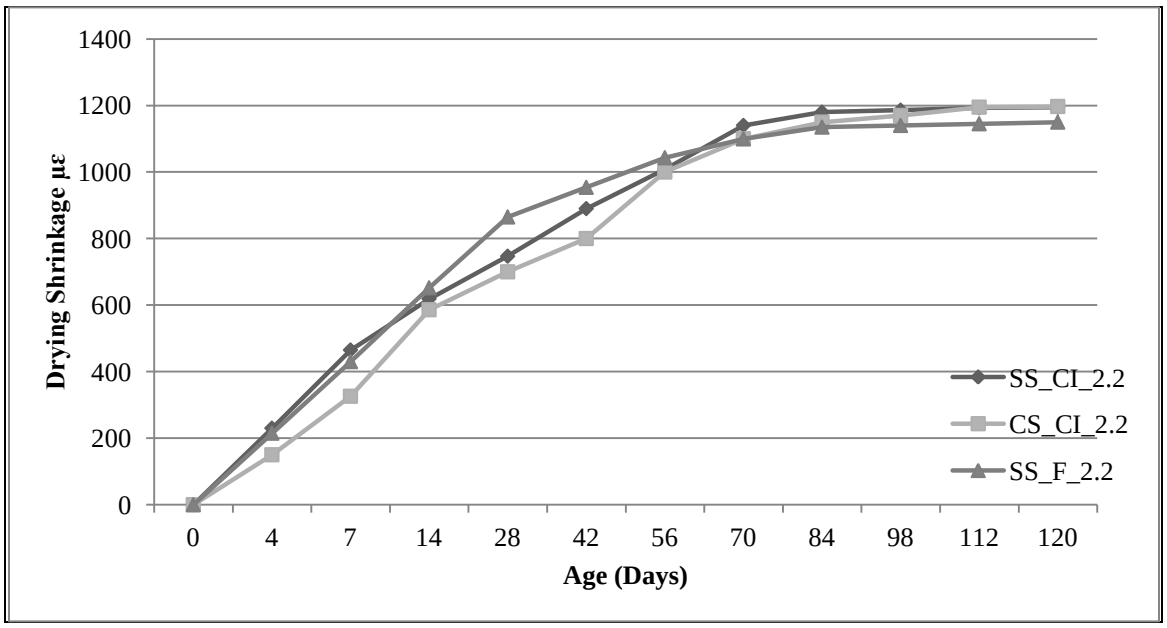

Figure 5.2 Drying shrinkage variation of ECC mixtures

Even though the difference between all these three mixes is very small in terms of drying shrinkage, the general trends in Figure 5.2 show that the use of class F FA reduced drying shrinkage deformation. Similar results have been reported for high volume fly ash concrete (HVFA) concrete (Sahmaran and Li, 2007; Sahmaran et al., 2009). A possible mechanism contributing to the reduction of drying shrinkage in ECCs is the matrix densification due to FA addition, which may prevent internal moisture evaporation (Maslehuddin et al., 1987). The matrix densification is typically attributed to the shape, pozzolanic property, and micro-filler effect of FA. This is being observed in the current study that use of class CI FA i.e with higher amount of pozzolanas tend to increase the drying shrinkage whereas class F FA being finer than class CI FA tends to decrease the drying shrinkage. An alternative mechanism is that un-hydrated FA particles act as aggregates, which provide restraint to shrinkage, and the coarser

pore structure, which results in decreased surface tension when a meniscus is formed and, thus, lower shrinkage forces exerted on the surrounding cement paste (Bisaillon et al., 1994; Zhang, 1995; Sahmaran and Li, 2007).

5.4 Freeze and Thaw Resistance

In this study, the frost resistance of different ECC mixtures was assessed by alternate freeze-thaw cycles in accordance with ASTM C666 Procedure A (2008) To measure the internal damage caused by freeze-thaw cycles, the changes in pulse velocity through a prism were also measured. The freeze-thaw durability test results are summarized in Table 5.3. Figure 5.3 shows the data of different ECC mixtures for the relative pulse velocity change V_i/V_0 and relative mass change M_i/M_0 with the number of freeze-thaw cycles. V_i and M_i are the pulse velocity and mass, respectively, after a specific number of freeze-thaw cycles, and V_0 and M_0 are initial pulse velocity and mass, respectively, prior to any freeze-thaw cycles.

Table 5.3 Freezing and thawing resistance of different ECC mixes

	ECC mix Designation		
	SS_CI_2.2	CS_CI_2.2	SS_F_2.2
Number of cycles completed	300	300	300
Changes in mass (%)	1.15	1.17	1.21
Pulse velocity change (%)	2.16	2.21	2.2

As seen in Figure 5.3a-b, the all the ECC mixture prisms showed excellent performance when exposed to freeze-thaw cycles, even after 300 cycles. All the mixes showed similar behaviour in terms of mass loss and change in pulse velocity. As can be seen in Table 5.3 the SS_CI_2.2 mixture showed the lowest mass loss and lowest pulse velocity change of 1.15 % and 2.16 %, respectively. A maximum of only 1.21 % and 2.2 % mass and pulse velocity losses, respectively, were observed for the ECC specimens for SS_F_2.2 mix. This results being in the same range provided with the evidence that the freeze-thaw resistance of ECC is independent of the type of supplementary cementitious material used and the type and maximum aggregate size of the aggregate considered under this investigation. This can also be observed in Figure 5.3, where the relationship between relative pulse velocity/relative mass loss and number of freeze-thaw cycles

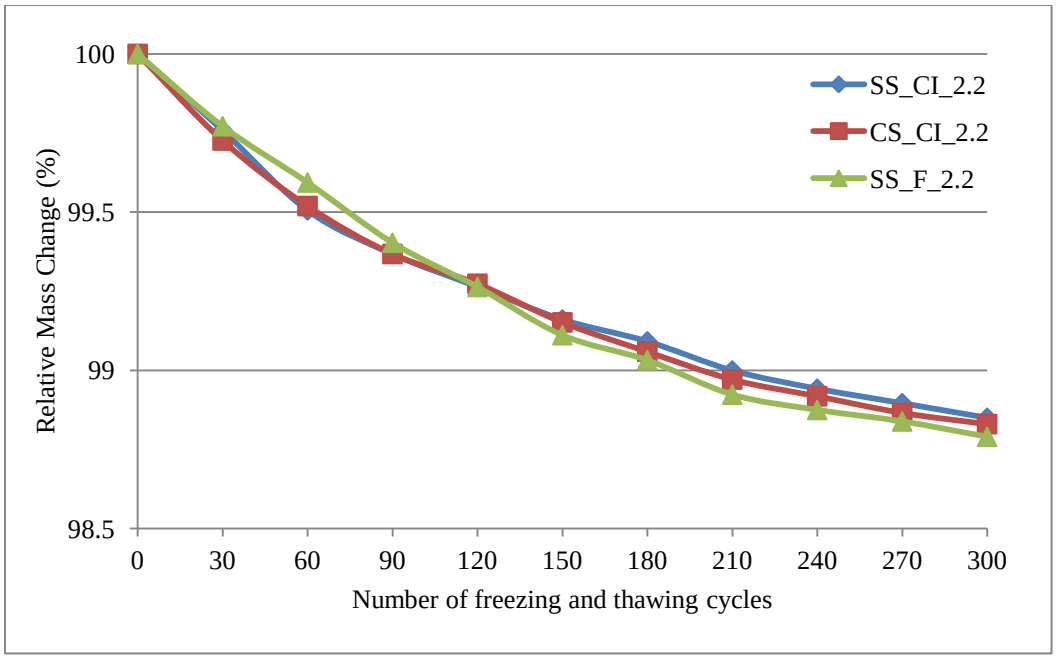

(a) Relative mass change (%)

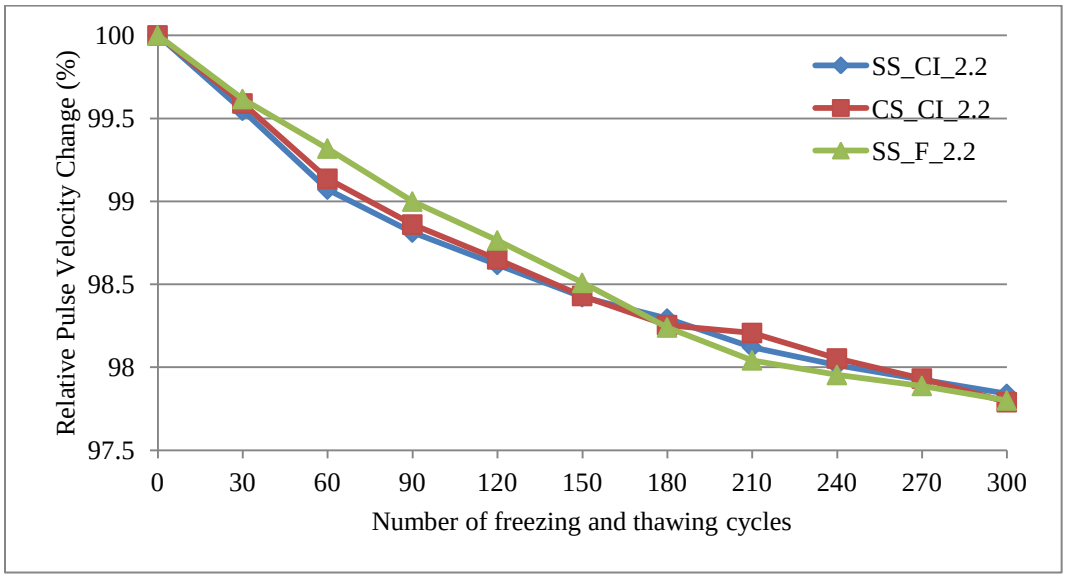

(b)Relative pulse velocity change (%)

Figure 5.3 Relative pulse velocity and mass loss changes as a function of number of freeze-thaw cycles.

is shown for ECC specimens that were subjected to 300 cycles. At the end of 300 cycles, very little scaling was observed on the ECC prism surface (Figure 5.4).

Figure 5.4 ECC specimen surface appearance after 300 freeze-thaw cycles

One of the possible reasons for the ECC's excellent frost resistance, which is favored by the previous researchers as well (Yang, et al., 2009; Lepech & Li, 2005b), can be attributed to its superior tensile properties. It is well known that upon freezing, water in capillary pores expands. If the required volume is greater than the space available, the pressure build-up could reach the tensile strength of the material, resulting in local micro-crack formation, brittle rupture and scaling. Therefore, the high tensile strength in ECC could lead to its higher frost resistant characteristic. The influence of micro-fiber addition on frost resistance of conventional concrete has also been examined by other researchers (Pigeon et al., 1996) and is in agreement with what is found in this study. The presence of air voids also can help enhance the freeze-thaw resistance by providing space to the increased volume of capillary water. When PVA fiber is incorporated into ECC matrix, the pressure-releasing effect due to larger pore size and the crack resisting effect contribute to the ability to resist deterioration during freeze-thaw cycles.

5.4.1 Flexural Performance

The flexural performance results in terms of flexural strength (modulus of rupture), ultimate mid-span deflection, residual crack width, and number of cracks has been provided in Table 5.4. Data for different ECCs containing fly ash CI and FA class F as supplementary cementitious material and microsilica sand and crushed sand as an aggregate type before and after undergoing 300 cycles of freeze-thaw deterioration are tabulated. The physical stress and mid-span deflection curves are presented in Figure 5.5. Each data point is an average of at least three specimens. As

seen from Table 5.4 and Figure 5.5, all ECC specimens irrespective of aggregate type and irrespective of type of SCM, showed strain-hardening behaviour, that is, a sustained increase in load capacity beyond the first matrix crack after freeze-thaw deterioration.

All of the ECC specimens with/without freezing and thawing deterioration showed multiple cracking behaviours with small crack spacing and tight crack widths (≤100 μm). The flexural stress increased at a slower rate, along with the development of multiple cracks with small crack spacing and tight crack widths. Micro-cracks developed from the first cracking point and spread out in the mid-span of the flexural beam, as shown in Figure 5.5. The bending failure in the ECC occurred when the fiber-bridging strength at one of the micro-cracks was reached; resulting in localized deformation once the modulus of rupture was approached.

The typical flexural stress-deflection curves of ECC specimens after frost deterioration show that the influence of 300 freezing and thawing cycles on the flexural stress-mid-span deflection curves is fairly minor. As seen in Table 5.4, the flexural strength was reduced from 11.86 to 9.44 MPa and the mid-span deflection from 7.96 to 4.47 mm, when micro silica sand was replaced by the crushed sand. Similarly, the reduction in the same range in the flexural strength and mid-span deflection was noticed when class CI FA was replaced with class FA F.fly ash F. However, all the mixes performed well in terms of flexural strength and mid-span deflection required for the link slab application of bridge deck, even after freeze-thaw deterioration. This may be attributed to the fact that micro-fibers inhibit the localization of micro-cracks into macro-cracks and consequently.

The typical flexural stress-deflection curves of ECC specimens before and after frost deterioration show that the influence of 300 freeze-thaw cycles on the flexural stress-mid-span deflection curves is fairly minor. This result is consistent with the earlier results of mass and pulse velocity losses of ECC specimens after 300 freeze-thaw cycles (Figure 5.3).

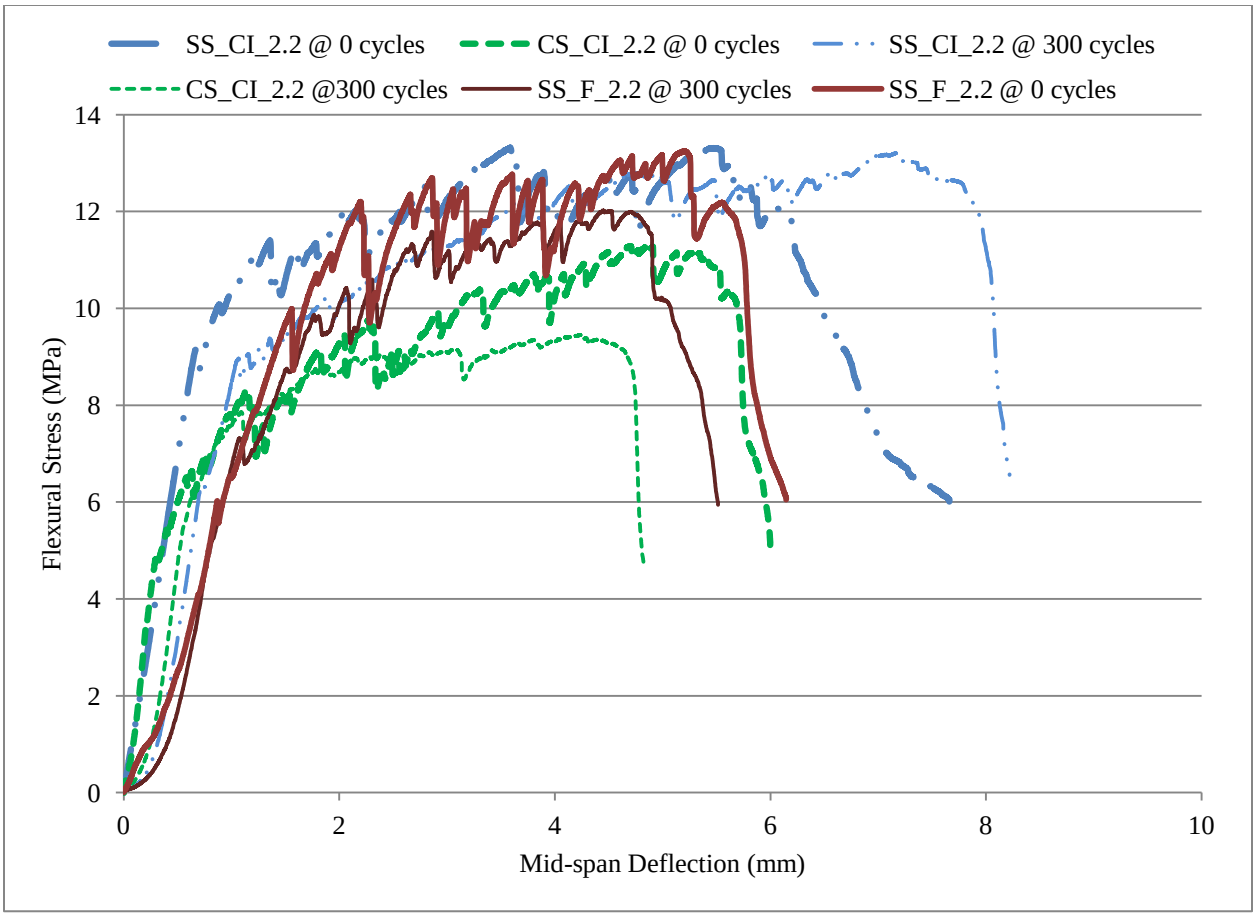

Figure 5.5 Flexural performance of ECC mixes after freeze-thaw cycles

Table 5.4 Flexural properties of different ECC mixes after 300 freeze-thaw cycles

Sr. No.	ECC Mix	No of Freeze-Thaw Cycles	Flexural Strength MPa	Ultimate Deflection Mm	Residual Crack Width µm	Number of Micro-cracks
1	SS_CI_2.2	0	13.28 ± 1.02	5.53 ± 0.23	≤ 50	121
2	CS_CI_2.2	0	10.94 ± 0.98	5.04 ± 0.78	≤ 50	104
3	SS_F_2.2	0	13.21 ± 1.84	5.31 ± 0.29	≤ 50	132
4	SS_CI_2.2	300	11.86 ± 1.35	7.96 ± 0.79	≤ 75	99
5	CS_CI_2.2	300	9.44 ±0.01	4.47 ±0.10	≤ 100	78
6	SS_F_2.2	300	10.92 ± 1.11	4.91 ± 0.05	≤ 75	43

Figure 5.6 Typical multiple crack pattern on the bottom tensile surface of ECC beam specimen after flexure load applications.

As seen in Figure 5.5, the first-cracking strength (corresponding flexural strength when there is a first drop in the graph which is due to first cracking of the specimen) of the ECC specimens after cyclic exposure falls below the first cracking strength of the virgin ECC specimens (control specimens prior to freeze-thaw cycles). The slope of the load-deflection curve represents the stiffness of the beams. Figure 5.5 shows that the slope with frost deterioration as well as the virgin specimen, thereby indicating a slight reduction in the stiffness of the ECC beams. Nevertheless, no significant reduction in the flexural strength of the ECC specimens exposed to 300 freeze-thaw cycles was detected.

It should be noted that the residual ultimate flexural load-deflection curves of frost deteriorated ECC beams (Figure 5.5) obtained following induced accelerated freeze-thaw cycling (up to six freeze-thaw cycles were achieved in a 24 h period) provide a conservative estimate of their residual flexural properties in actual structures. These accelerated deterioration periods are

equivalent to a time span of many years in real structures, even those located in regions with harsh winters. This difference in accelerated and normal frost deterioration periods should have a significant influence on the residual flexural properties of ECC because in the long term, deterioration in ECC as a result of freeze-thaw cycles can easily be closed due to a self-healing process (Sahmaran and Li, 2007). Thus the flexural performances of ECC summarized in Table 5.4 are overestimated.

Table 5.4 summarizes the flexural strength (modulus of rupture) and total mid-span deflection at the peak stress of ECC specimens exposed to 300 freeze-thaw cycles. The total deflection of the ECC beam, which reflects the material flexibility, exposed to 300 freeze-thaw cycles is in the range of 4.47 to 7.96 mm, which is slightly lower than that of ECC specimens prior to undergoing freeze-thaw cycles. Compared to the control ECC specimens cured in laboratory air (Table 5.4), the ECC specimens exposed to freeze-thaw cycles showed reductions of nearly 15 % in flexural strength at the end of 300 cycles; this may be attributed to the effects of damage on the fiber/matrix interface and matrix micro-cracking. Out of all mixes, the mix with class CI FA maintained higher flexural strength due to early bonding due to higher CaO% compared with class F FA.

Table 5.4 also shows the residual crack width of different ECC mixtures. The term "residual crack width" indicates that crack width was measured from the unloaded specimen after the four-point flexural test by using a portable microscope with an accuracy of 5 μm. Both frost-deteriorated and virgin ECC specimens revealed saturated multiple cracking (Figure 5.6) with crack width at ultimate flexural load limited to below 100 μm. Crack width control is of primary importance for many reinforced concrete applications since it is believed that there is a close relationship between the mean or maximum crack widths and the durability of the structure. Moreover, the lower magnitude of the crack width is expected to promote self-healing behaviour, and thus the transport properties in cracked composites (Sahmaran et al., 2007; Sahmaran and Li, 2009b; Yang et al., 2009). In terms of permeability and diffusion, a crack width less than 100μm generally behave like sound concrete (Wang et al., 1997; Sahmaran et al., 2007). Based on experimental results Sahmaran et al. (2007), Evardsen (1999), and Reinhardt and Jooss (2003) proposed that cracks with a width below 100 μm can be easily closed by a self-healing process.

5.5 Absorption and Porosity

Figure 5.7 presents the results of water absorption and porosity tests. It can be seen that the change of supplementary cementing materials and change of aggregate type did not remarkably affect the water absorption and porosity. SS_CI_2.2 mixture had 10.75 % and 21.38 % of water absorption and water porosity, respectively; while those values were 11.54 % and 22.08 % for mix CS_CI_2.2. This minor change in water absorption and porosity could be attributed to the change in aggregate type. As microsilica sand is finer than crushed sand, improvement of packing density could be attained with the mix SS_CI_2.2 compared to CS_CI_2.2. This could have resulted in slight reduction in water absorption and porosity. Similarly, SS_F_2.2 mixture had 10.71 % and 20.94 % water absorption and porosity, respectively. Fly ash F particles being finer than fly ash CI could have resulted in lower water absorption and porosity with respect to mix SS_CI_2.2.

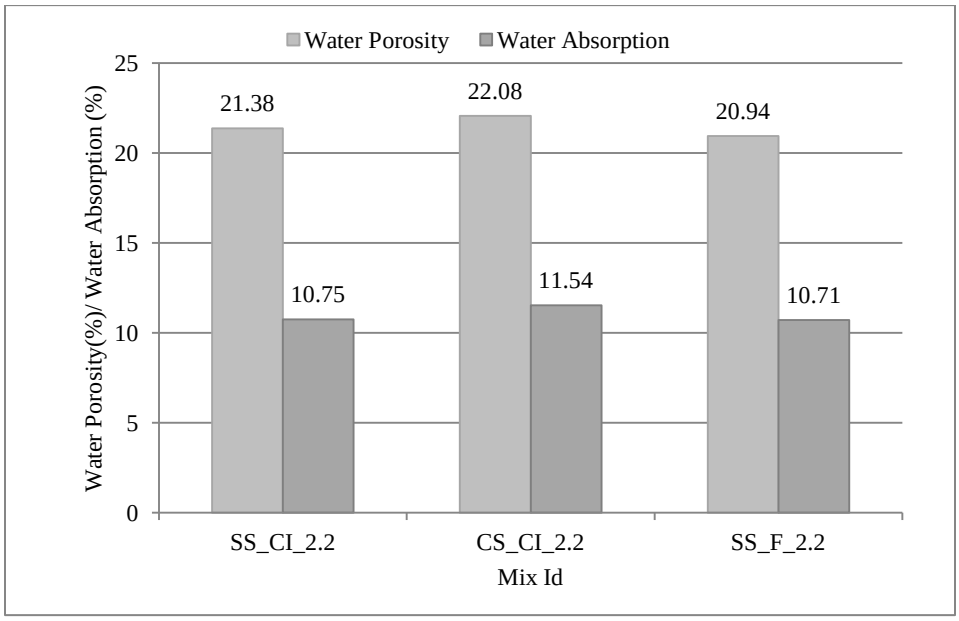

Figure 5.7 Water absorption and porosity test results of different ECC mix

It has been observed that the replacement of higher volume of fly ash may lead to higher water absorption and porosity. Similar finding on the mortar and concrete specimens was also reported by other investigations (Bisaillon et al., 1994; Ozkan and Mehmet, 2009). The most probable reason of the higher water absorption and porosity with high volume of FA is that the slow fly ash pozzolanic reaction due to lack of insufficient curing. As explained in the "experimental program" section, ECC specimens were cured in air after a 7-day sealed curing. But as the

samples get cured by the atmospheric moisture, the results of water absorption and porosity could further reduce. Moreover, the water absorption and porosity values given in Figure 5.7 likely represent upper limits of transport properties in actual structures.

5.6 Sorptivity

The sorptivity is a material property that characterizes the tendency of a material to absorb and transmit water by capillarity. Therefore, sorptivity test measures the rate of capillary suction at a specified time. The value of sorptivity illustrates the water mass uptake by concrete from the bottom surface. The cumulative water absorption per unit area of the 50 mm cube specimen up to 6 h and 8 days were fitted using linear regressions and the slope of equations obtained were used to describe initial and secondary sorptivity of ECC mixtures, respectively. Figure 5.8 demonstrates the both initial and secondary sorptivity coefficients of ECC mixtures. As seen in Figure 5.8, changing the aggregate from microsilica sand to crushed sand i.e. increasing maximum aggregate size lead to slight increase in both the initial and secondary sorptivity of the ECC from 0.029 mm/min$^{1/2}$ and 0.007 mm/min$^{1/2}$ to 0.033 mm/min$^{1/2}$ and 0.008 mm/min$^{1/2}$, respectively. Similarly, changing supplementary cementitious material from class F or class CI FA (i.e. SS_CI_2.2 to SS_F_2.2) has also lead to the slight reduction in initial and secondary sorptivity from 0.029 mm/min$^{1/2}$ and 0.007 mm/min$^{1/2}$ to 0.023 mm/min$^{1/2}$ and 0.005 mm/min$^{1/2}$, respectively.

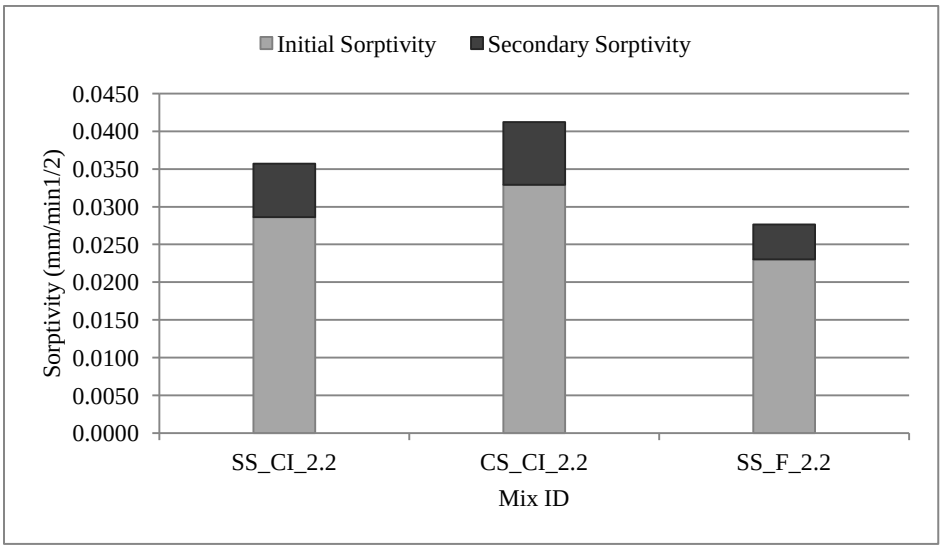

Figure 5.8 Initial and secondary sorptivity test results of different ECC

However, as noted, even at about 70% (SCM/C =2.2) replacement of cement with FA, the initial sorptivity is still remarkably less than the sorptivity coefficient of normal concrete. According to Neville (1996), typical sorptivity is 0.09 mm/min$^{1/2}$ for oven dried at 105°C normal concrete specimen with a w/c ratio of 0.40. Other research suggested that ordinary Portland cement concrete with w/c ratio of 0.40-0.50 would have sorptivity of about 0.23 mm/min$^{1/2}$ (Tsivilis et al., 2003). Therefore, the measured sorptivity (<0.045 mm/min$^{1/2}$) for all the ECC specimens was not particularly high when compared to that of conventional concrete. The reason for the lower sorptivity of ECC mixtures may be attributed to a significantly lower w/b ratio, high FA content and absence of coarse aggregate. The use of FA probably resulted in a denser matrix, by reducing the pore size and thickness of transition zone between fiber and surrounding cementitious matrix (Kuroda et al., 2000).

5.7 Accelerated Reinforcement Corrosion

During the accelerated corrosion, it was assumed that the electrical potential applied to the reinforcement attracted negatively charged chloride ions from the solution into the concrete and toward the positively charged steel bars. As the chloride ions reached the steel-concrete interface above threshold concentration, the steel surface began to corrode. The expansive products of corrosion-imposed tensile stresses on the ECC cover resulted in cracking when the tensile stresses exceeded the tensile strength of the cover material. Cracking, especially large cracks, would allow the conductive chloride solution to come into direct contact with the steel surface, thus providing a direct current path between the reinforcement and the electrodes in solution. Therefore, a dramatic increase in current flow, suggests a reduction in electrical resistance following cracking in the cementitious material around the steel bar.

The current response as a function of time under the fixed potential is shown in Figure 5.9. Each line in Figure 5.9 is the average of two specimens. The current-time curves were used to determine the time to initiation of reinforcement corrosion by observing any instantaneous rise in the current recorded. As can be seen from Figure 5.9, the current recorded for all the different ECC mixtures were much lower, in the range of 0.2 to 0.23 A up until 15 to 20 hours. The lower initial current recorded in the ECC specimens may reflect the higher electrical resistivity of the ECC. In general, each of the current responses and corrosion rates of the material is considered to be inversely proportional to the electrical resistivity of the material (Bazant, 1979; Smith et al.,

2004). In addition, according to Andrade et al., (1993) the resistivity is inversely proportional to the chloride diffusion coefficient in concrete materials and, therefore, the corrosion initiation period.

For ECC, a lower w/b material ratio (*w*/*cm*) and high-volume fly ash (FA), resulting in a denser matrix by reducing the pore sizes and thickness of the transition zone between the fiber and the surrounding cementitious matrix, may explain the observed higher electrical resistivity (Hussian and Rasheeduzzafar, 1994; Hossain, 2003; Hossain, 2003; Hossain and Lachemi, 2004; Sun et al., 2004; Hossain, 2005; Hossain, 2005); This higher electrical resistivity of ECC is expected to be associated with a longer corrosion initiation period under field conditions.

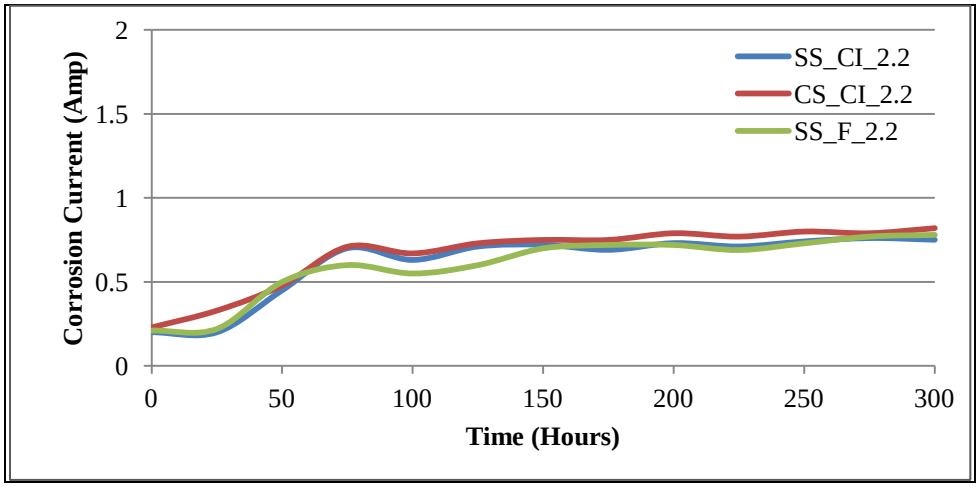

Figure 5.9 Measured corrosion current with time for different ECC mixtures

As the experiment was continued, the recorded current (and the corrosion of the steel bar) steadily increased and all the ECC mixture specimens followed more or less the same trend until approximately 75 hours. Micro-cracking on the surface of these specimens was first noted after 40 hours. Beyond 75 hours, the recorded current became more or less steady until the failure (defined in the following as when the crack width reaches 0.3 mm (ACI Committee 318, 1995)) of the ECC specimens. Out of all the mixes, ECC CS_CI_2.2 showed the highest recorded current whereas SS_CI_2.2 and SS_F_2.2 were in the same range. Despite being difference in the recorded current, this difference being so small and thus it was negligible. Large cracks were absent in all the specimens and rather a distribution of micro-cracks was observed. The tight crack width of the surrounding ECC did not allow easy access of the moisture (Lepech and Li,

2005a) and chloride ions (Sahmaran et al., 2007) to the surface of the steel bars embedded in the ECC specimens. In addition, self-healing (Sahmaran et al., 2007) and potentially plugging of these microcracks by corrosion products may have occurred. Microcracks tend to be easier to seal than large cracks, thus prolonging the corrosion propagation period. This increase in the accelerated corrosion propagation time indicates a superior durability performance of ECC over mortar. Whereas the increase in the number of microcracks tends to lower the resistivity of the specimen, the plugging of these cracks that stabilize in width below 100 μm is likely responsible for the steady state current observed beyond 75 hours in Figure 5.9. The typical surface patterns of corrosion-induced cracks for typical ECC specimens after subjected to accelerated corrosion test are shown in Figure 5.10.

Figure 5.10 ECC specimen after accelerated corrosion test; after 300 hours of accelerated corrosion (Mix ID: CS_CI_2.2)

Multiple microcracks on the two wider faces of the ECC beams were observed. The number of microcracks on the surface of ECC specimens increased as corrosion progressed. This could be attributed to the strain-hardening and multiple-cracking behaviours of ECC. After 150 hours of accelerated corrosion, numerous (at least 10) microcracks with widths less than 0.1 mm were observed on each surface of the ECC specimens. This implies that ECC maintains substantial resistance against cover spalling in R/ECC members in the presence of significant steel bar corrosion. At the end of 300-hour accelerated corrosion test, in addition to microcracks, one longitudinal localized crack with width of nearly 0.3 mm on the surface of the ECC prism specimens was observed. If a crack width of 0.3 mm is defined as a failure limit for RC structures, as, for example, suggested by an earlier version of the ACI Building Code (ACI Committee 318, 1995) or AASHTO (2004) for crack width limit for outdoor exposures, the service life duration of R/ECC will be at least 15 times that of the ordinary concrete specimens

(Sahmaran et al., 2008). This indicates that ECC significantly extends service life (time to corrosion initiation plus time to corrosion propagation) under accelerated test conditions.

5.7.1 Mass Loss Measurements

To measure the mass loss of the reinforcing steel, the specimens were broken after performing four point flexural tests to retrieve the entire reinforcing bar after inducing different degrees of accelerated corrosion exposures. The reinforcing bar for each specimen was cleaned with deionised water and scrubbed with a stiff metal brush to ensure that the bar was free from any adhering corrosion products. The reinforcing bar was then weighed and the percentage mass loss was computed using Eq. 5.1

$$Corrosion\ Mass\ Loss = \frac{[Initial\ Mass - Final\ Mass]}{[Initial\ Mass]}\ x\ 100 \qquad (5.1)$$

Where, the initial and final mass refers to the mass of the reinforcing bars before and after corrosion exposures. The percentage of steel mass losses of different ECC mixes at different accelerated corrosion exposures has been presented in Figure 5.11. Initially there was nearly no mass loss of reinforcing bars embedded in all the ECC specimens up to 50 hours of accelerated corrosion exposure. Out of these three mixes mix CS_CI_2.2 showed the highest percentage of mass loss of 25.4% at 300 hours. While ECC mixes SS_F_2.2 and SS_CI_2.2 showed slightly lower percentage of mass loss of 24.3% 23.7% at the end of 300 hours of accelerated corrosion exposure, respectively. These differences in % mass loss being small, it was clear that there was no apparent influence of maximum aggregate size, aggregate type or the supplementary cementitious material type.

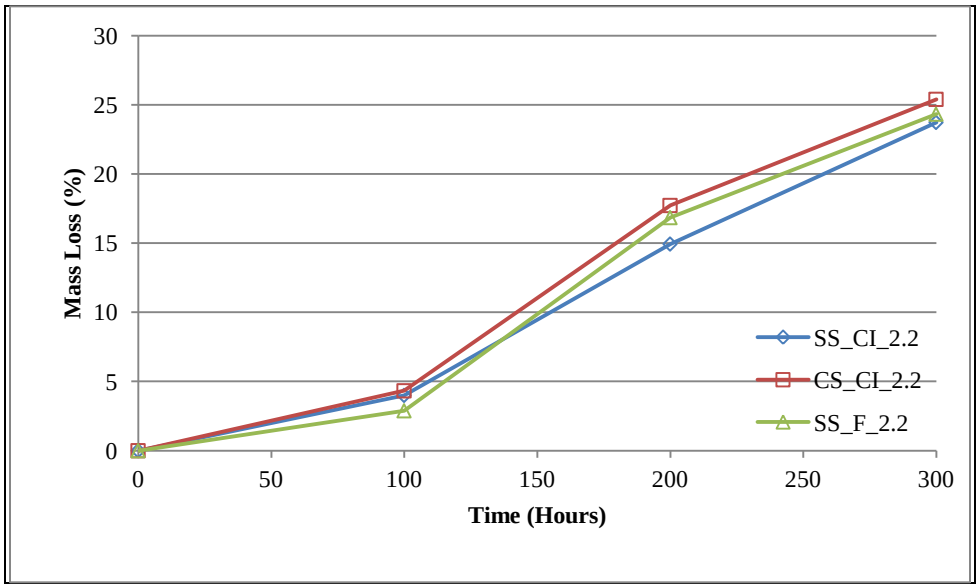

Figure 5.11Mass loss versus corrosion exposure time for ECC and mortar corrosion specimens

For all the ECC beams, the tight crack width inhibits movements of the corrosion products that serve as a shield against chloride ion migration toward the steel bar. Therefore, ECC cover reduces the corrosion rate of steel reinforcement significantly when compared with an ordinary concrete cover, at least under the present accelerated test conditions.

5.7.2 Residual Flexural Load

After inducing different degrees of accelerated corrosion, the corroded beams were tested under four-point bending to determine their residual load-deflection curves and ultimate flexural loads. Bending loads were applied to the smaller face of the beam (the face was 50 mm wide).

The ultimate flexural load of the deteriorated (with corrosion) and control (without corrosion) specimens of all the ECC specimens at each selected degree of accelerated corrosion level is summarized in Table 5.5. Average ultimate flexural loads for the beam specimens were obtained by combining the results of two specimens tested in each case. All the ECC mixtures showed excellent resistance to the accelerated reinforcement corrosion and their flexural behaviour remained intact. Ultimate flexural load was in the range of 6.70 to 8.10 kN and their respective mid-span deflections were in the range of 2.80 to 3.95 mm.

Table 5.5 Ultimate flexural load at different degrees of accelerated corrosion level

Accelerated Time, Hours	Ultimate Flexural Load (KN)			Mid-span Deflection (mm)		
	SS_CI_2.2	CS_CI_2.2	SS_F_2.2	SS_CI_2.2	CS_CI_2.2	SS_F_2.2
0	18.82	19.27	17.72	3.09	3.9	3.8
100	14.11	17.62	14.5	3.16	3.47	3.48
200	11.75	12.84	11.38	3.01	4.62	3.76
300	7.84	8.08	6.74	3.11	3.94	2.84

All ECC specimens showed multiple cracking behaviours with small crack spacing and tight crack widths (<0.1 mm). This proved that all the ECC mixes, maintained the multiple micro-cracking behaviour even after undergoing accelerated reinforcement corrosion. Bending failure in the ECC occurred when the fiber bridging strength at one of the micro-cracks was reached, resulting in localized deformation at this section.

Typical load-deflection curves of the different ECC mixtures before (control) and after different accelerated corrosion periods (corroded, *x* hours) are shown in Figure 5.12. To facilitate the comparison between the test results for different ECC mixes, the same scales for both axes were used in these figures. These curves of different ECC mixes shown in Figure 5.12 reveal that the influence of accelerated corrosion test up to 100 hours on the load-deflection curves of all ECC specimens were fairly small. Beyond 100 hours of accelerated corrosion, the ultimate residual flexural load capacity of ECC specimens decreased slowly as corrosion progressed. All the mixes behaved in the similar manner when exposed to the accelerated corrosion. Out of these three mixes, mix CS_CI_2.2 showed the highest amount of ultimate flexural load as well as the deflection at the end of 300 hours of accelerated corrosion. Higher CaO content resulted in early bonding which was facilitating in maintaining higher strength compared with class F FA. It was 8.08 kN in comparison to 7.84 kN and 6.74 kN for mixes SS_CI_2.2 and SS_F_2.2, respectively. It is worth noting that there was no noticeable reduction in the mid-span deflection because of the accelerated corrosion which was observed for all the mixes. In other words, all the mixes showed the ultimate mid-span deflection almost in the same range which was before accelerated corrosion. The only reduction was observed in the ultimate flexural load. All the mixes showed the reduction of ultimate flexural load in the range of 58% to 62% with their respective control specimens. These results were consistent with the earlier results of steel mass loss of ECC

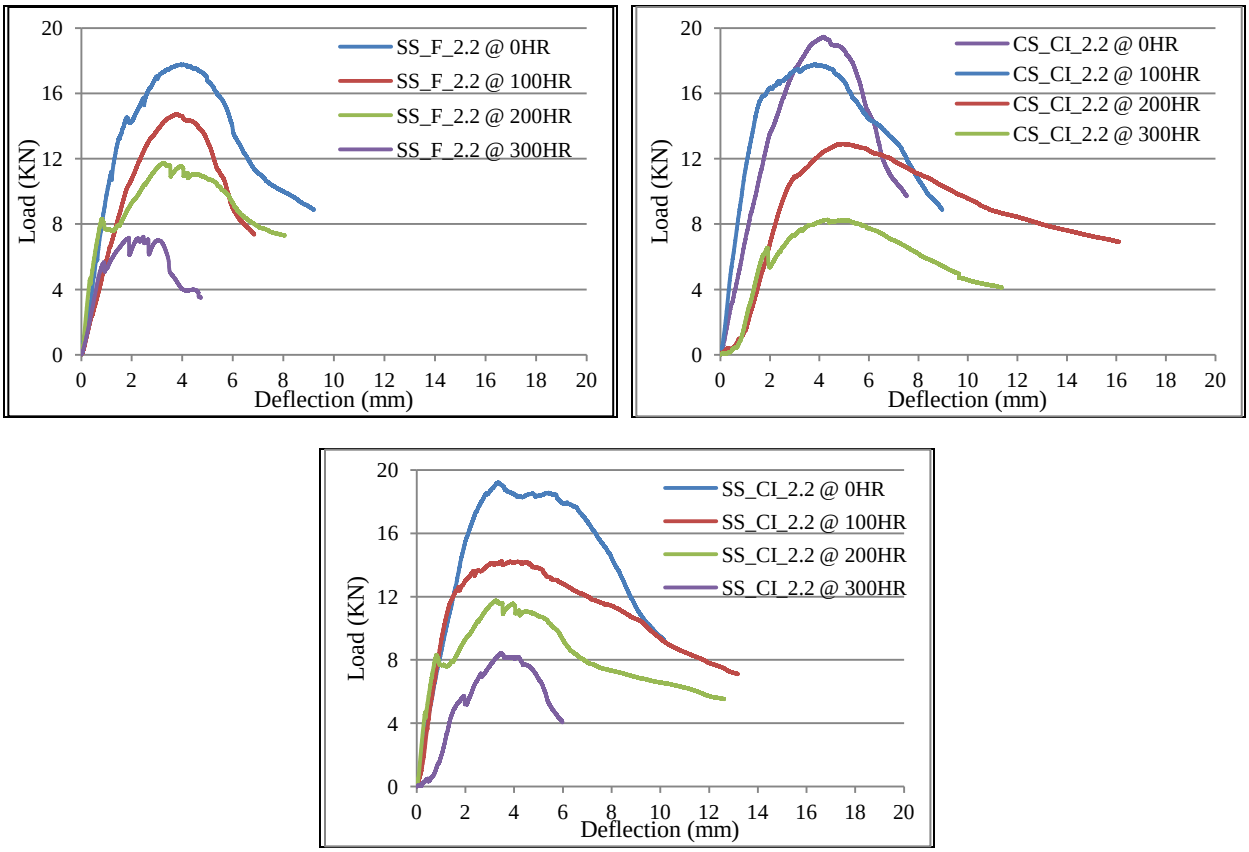

Figure 5.12 Effect of accelerated corrosion on load-deflection curves of different ECC mixes

specimens (Figure 5.11). The decrease in the ultimate flexural loads is attributed to the loss of the cross-sectional area of steel reinforcements and, in addition, to the presence of multiple micro-cracking. On the other hand, ECC deterioration due to the corrosion of reinforcement did not change the type of failure in ECC beams. All the specimens irrespective of the duration of accelerated corrosion control ECC beams failed in flexure.

The residual ultimate flexural load-deflection curve of corroded ECC beams presented in Figure 5.12 provides a conservative estimate of their ultimate residual flexural load capacity in actual structures. This is because the effect of self-healing of micro-cracked ECC has not been included in these specimens due to the short experimental duration. Tuutti (Tuutti, 1982) proposed that cracks of width less than 0.1 to 0.3 mm did not affect the corrosion rate of the reinforcing steel. The residual flexural load capacity of the ECC beams was determined following induced accelerated corrosion of the reinforced specimen during 50 to 300 hours.

Such corrosion periods are equivalent to those of many years in real structures. This difference in accelerated and normal corrosion periods can have a significant influence on the residual flexural load of ECC. For long-term corrosion exposure, after corrosion initiates, micro-cracks in ECC generated by mechanical loading or corrosion expansion can easily be closed or become smaller and less connected among them due to self-healing, (Sahmaran et al., 2007) thus slowing down further chloride penetration and reducing the rate of corrosion propagation.

The present accelerated corrosion experiment had been carried out by applying a constant potential to the specimens, as is typical of this type of investigation (Hossain and Lachemi, 2004; Hossain, 2005; Sahmaran et al., 2008). Because of the expected differences in electrical resistance between different uncracked ECC, however, the generated currents may also be different. As a result, the rate of corrosion and mass loss rate data may reflect this difference and therefore should be interpreted with care. Even so, the tight crack width of ECC provides an effectively higher resistance material by limiting the access of chloride ions, carbon dioxide, and moisture to the reinforcing bar may be different for different mixtures. If we compare the results of these ECC mixes with ordinary concrete, all these ECC mixes showed quite lower current (higher resistance) than the ordinary concrete (Hossain and Lachemi, 2004; Hossain, 2005; Sahmaran et al., 2008). This results in a reduction of current (and therefore mass loss and corrosion rate), which is a real benefit of ECC over mortar. Regardless of the way the accelerated corrosion test was conducted, the mode of failure between ECC and mortar are substantially different.

5.8 Summary

Three best ECC mixes were selected out of ten developed trial mixes based on superior flexural strength, ductility and crack width in addition to meeting the requirements of self consolidation. Durability property tests (such as rapid chloride ion penetration, drying shrinkage, freeze-thaw resistance, water absorption / porosity/sorptivity and accelerated corrosion) were performed on these three mixes designated as SS_CI_2.2, CS_CI_2.2 and SS_F_2.2. All these mixes were performed similarly with minor differences in terms of durability. All these mixes met the requirements for their application to link slab of the bridge deck. It would be worth mentioning that there is no considerable influence of type of fly ash (CI or F) , type of aggregate (crushed sand or silica sand) or maximum aggregate size on ECC durability studied under this research.

CHAPTER SIX

STRUCTURAL PERFORMANCE AND EVALUATION OF BRIDGE DECK WITH ECC LINK SLAB

6.1 Introduction

This chapter discusses the structural application of ECC for link slab construction in bridge deck. To validate the feasibility of using ECC for the structural application specifically for the link slab in the bridge deck, scale down link slab specimens were cast with different mixes and with different reinforcement ratios. For the purpose of comparing the results of ECC link slab with normal concrete link slab, SCC link slabs were cast as a control specimen. As discussed in the chapter of experimental program, SCC can be cast without compaction like ECC and suitable for construction of link slab with congested reinforcement - self compatibility provides an added advantage. The results of structural testing of ECC/SCC link slabs under monotonic static loading are described based on load-deflection response, strength, stress-strain development, cracking/crack propagation and failure modes. In addition, the influence of concrete material ductility on the shear load–slip response of stud shear connectors (integral to part of a bridge deck) including failure mode are described based on push out tests conducted on specimens made with ECC and SCC.

6.2 Experimental Program

6.2.1 Selection of ECC Material for Link Slab Tests

For material selection based on the Integrated Structure-Material Design concept, (Li and Fischer, 2002) property requirements of ECC material for link slabs were examined prior to material design mentioned in the previous chapters using fresh, mechanical and durability properties. All the ECC mixes were designed to achieve a minimum compressive strength of 35 MPa on the basis of widely chosen design compressive strength (27.5 MPa) of concrete in bridge deck slabs. Current AASHTHO Standard Specifications for Highway Bridges 2002 (AASHTO code thereafter) provide maximum permissible crack width of 330 μm in reinforced concrete (R/C) bridge deck in severe exposure conditions. The data obtained from the freeze-thaw test results indicate that all the ECC specimens even after 300 freeze-thaw cycles showed the crack width below 100 μm while maintaining excellent flexural property. The influence of reduced

crack width on the permeability of water contaminated by harmful substances such as chlorides introduced by de-icing salt has been evaluated using the test results of ECC water permeability in the previous chapter and reference data (Wang et al., 1997). The data obtained from sorptivity test results and from Figure 5.8 (Chapter 5) indicate that for crack widths below 100 μm the permeability coefficient remains relatively small and constant (10^{-10} m/s). As per Figure 2.7 (Chapter 2), at increasing crack widths, however, the permeability coefficient increases rapidly and reaches values several magnitudes higher (10^{-6} m/s at 330 mm crack width). Therefore, the desired crack width was to keep less than 100 μm to approach transport properties of sound concrete without cracks for corrosion resistance.

Based on the study of fresh, mechanical and durability properties two mixes were chosen - one with microsilica sand and one with crushed sand as an aggregate type. Based on the same test results it was noted that the performance of ECC mixes with class F or class CI FA was similar. For this reason a change was made in original research plan and as a effect of change, only two mixes were selected having fly ash F as a SCM and microsilica sand and crushed sand as an aggregate type. The mix design of the chosen ECC mixes (ECC-CS_F_2.2 and ECC-SS_F_2.2) and SCC mix are already discussed in the previous chapter.

6.2.2 Link Slab Testing Configuration

Construction of link slab is a relatively new technology and the long-term behaviour of link slabs is still not well documented. The experimental testing was carried out on small-scale link-slab specimens. The deformed shape and moment distribution due to applied load of a two-span bridge structure with link slab are schematically shown in Figure 6.1(a). Flexural crack formation was expected at the top of the link slab as illustrated in Figure 6.1(b). Therefore, the link slab specimens were designed to include the link slab within the distance between the points of inflection in the adjacent spans. The location of inflection point should be determined by the stiffness of the link slab. In case of zero stiffness, the point of inflection is located at the support, while for a continuous girder and deck its location is at 20% of the span length from the support. In the case of a link slab with girder discontinuity, the point of inflection is located within these boundaries.

As the design procedure for the link slab detail currently requires a debond length of 5% of the simple supported span (Lepech and Li, 2009), the same debond length was adopted in current study. This debonded length requirement was supported by early study (El-Safty 1994). The tests were designed to study the effect of ECCs made with different aggregate type/size as well as the reinforcement ratio on the link slab behaviour.

6.2.3 Design of Test Specimen and Casting

The specimen test setup focused on the link slab portion between the points of inflection in the adjacent spans as illustrated in Figure 6.1(b). The full scale dimension of the representative bridge deck was 711 mm width and 230 mm depth. Based on this, a typical ¼ scale link slab model has a total length of 930 mm, width of 175 mm and depth of 60 mm depth. Figure 6.2 shows the SCC/ECC link slab specimen geometry showing debond zone length (300 mm) equal to roughly 2.5% of both adjacent spans. It is noted that the length and depth dimensions of the specimens are identical to a link slab between two adjacent span of a full-scale bridge. The thickness of the full-scale link slab was 230 mm which corresponds to typical deck slabs in simply supported composite girder bridges. The location of inflection point should be located between 0% and 20% of the span and for the current study, 7% was selected. The complete structural detail is discussed in Appendix A.

Altogether four link slab specimens (LS1 to LS4) were cast (Figure 6.2). For all the specimens, adjacent bridge deck part was with SCC. For control SCC link slab specimens (LS4, Figure 6.2(c)), link slab portion was also cast with SCC. For three ECC link slab specimens, link slab portion was cast with two ECCs and by employing two different reinforcement ratios (r/f ratio). One link slab (LS 2, Figure 6.2(c)) was cast with ECC mix SS_F_2.2 with 3, 6mm bars (0.010% r/f ratio), one (LS3, Figure 6.2(c)) with CS_F_2.2 with 3, 6mm bars (0.010% r/f ratio) and one (LS1, Figure 6.2a) with CS_F_2.2 4, 6 mm bars (0.012% r/f ratio). The details of link slab specimens are presented in Table 6.1.

For all the link slabs, as followed in the general field practice, the bridge deck part was cast initially and left for setting for 24 hours. After 24 hours, the link slab zone was cast with different ECC mixtures or SCC. The specimens were cured for 28 days at the laboratory

conditions while covered with burlap. The relative humidity (RH) and the temperature of the laboratory was 45+5% and 24+2°C, respectively.

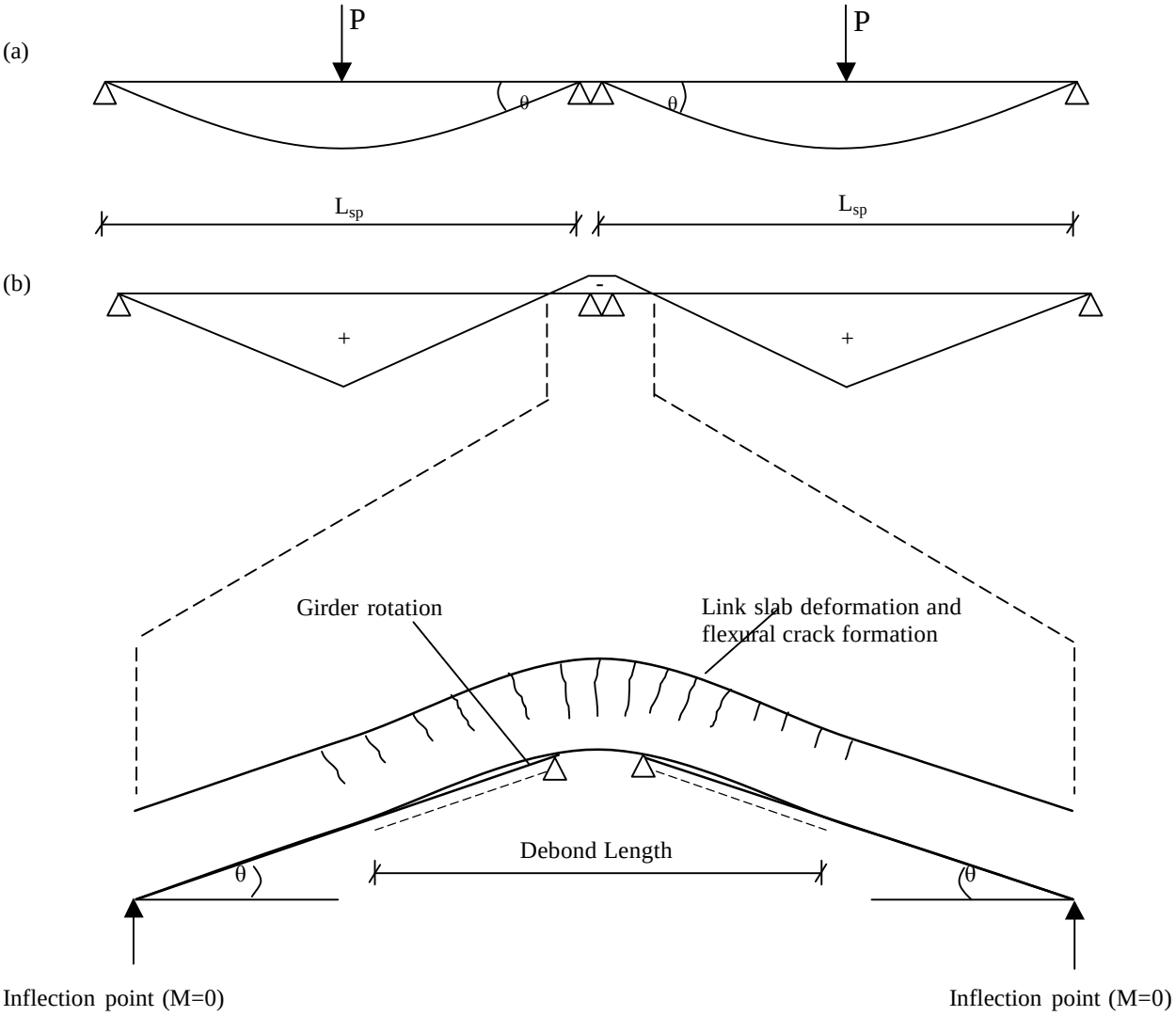

Figure 6.1 Schematics of two span bridge subjected to point load at mid-span for (a) deformed shape of bridge and (b) moment distribution on bridge span and corresponding deformed shape of link slab region

Table 6.1 Details of the link slab specimens

Designation	Detail of Concrete Mix	R/F Ratio	R/f Detail	Debond Length	Shear Stud Detail
LS-1	ECC-CS_F_2.2	0.012%	4-6 mm ϕ	2.5 % of adjacent span	8-10 mm ϕ shear stud on each side
LS-2	ECC-CS_F_2.2	0.010%	3-6 mm ϕ		
LS-3	ECC-SS_F_2.2	0.010%	3-6 mm ϕ		
LS-4	SCC	0.010%	3-6 mm ϕ		

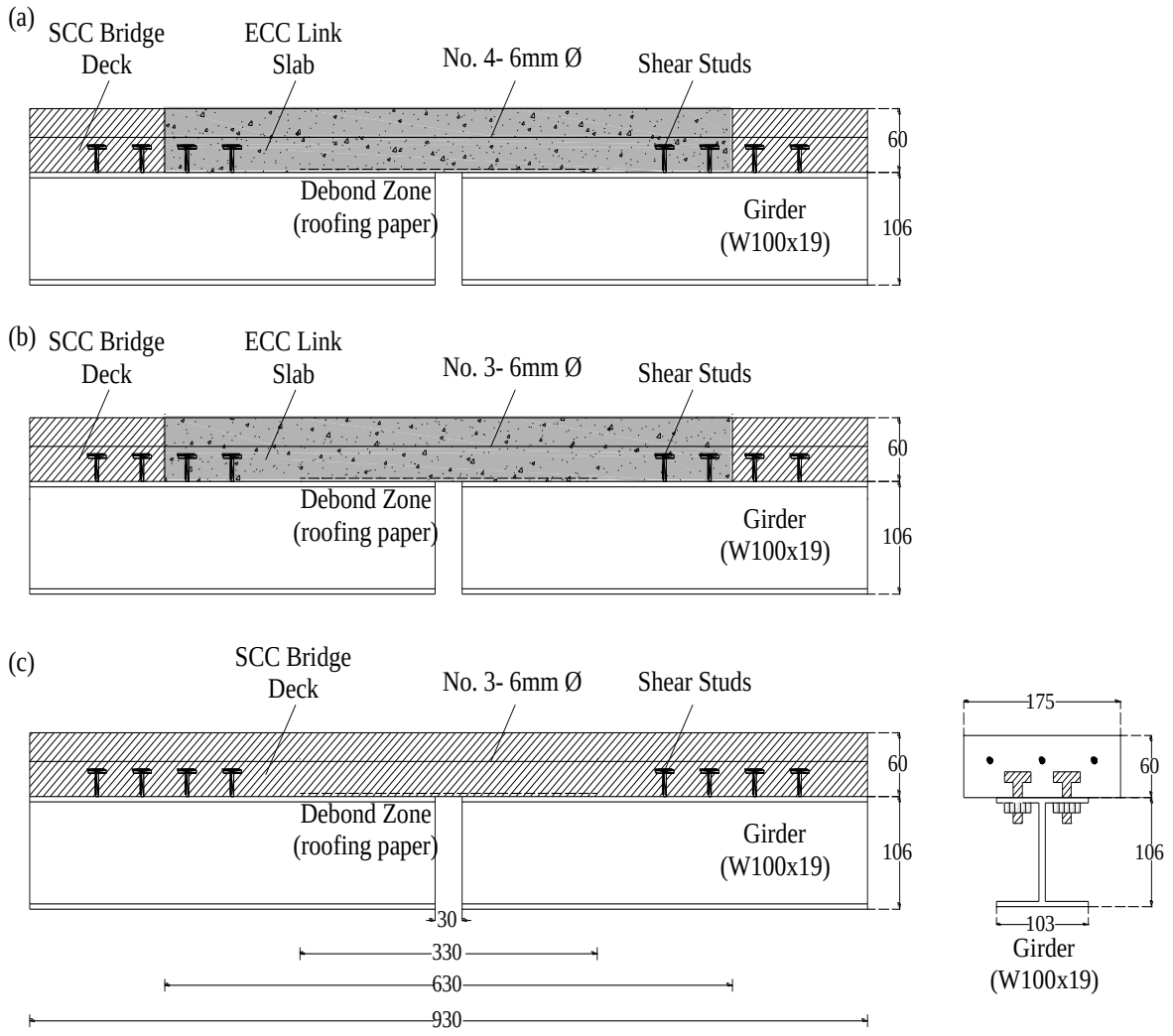

Figure 6.2 Geometry of link slab specimen for (a) LS-1 (b) LS-2, LS-3 and (c) LS-4 (Dimensions are shown in mm)

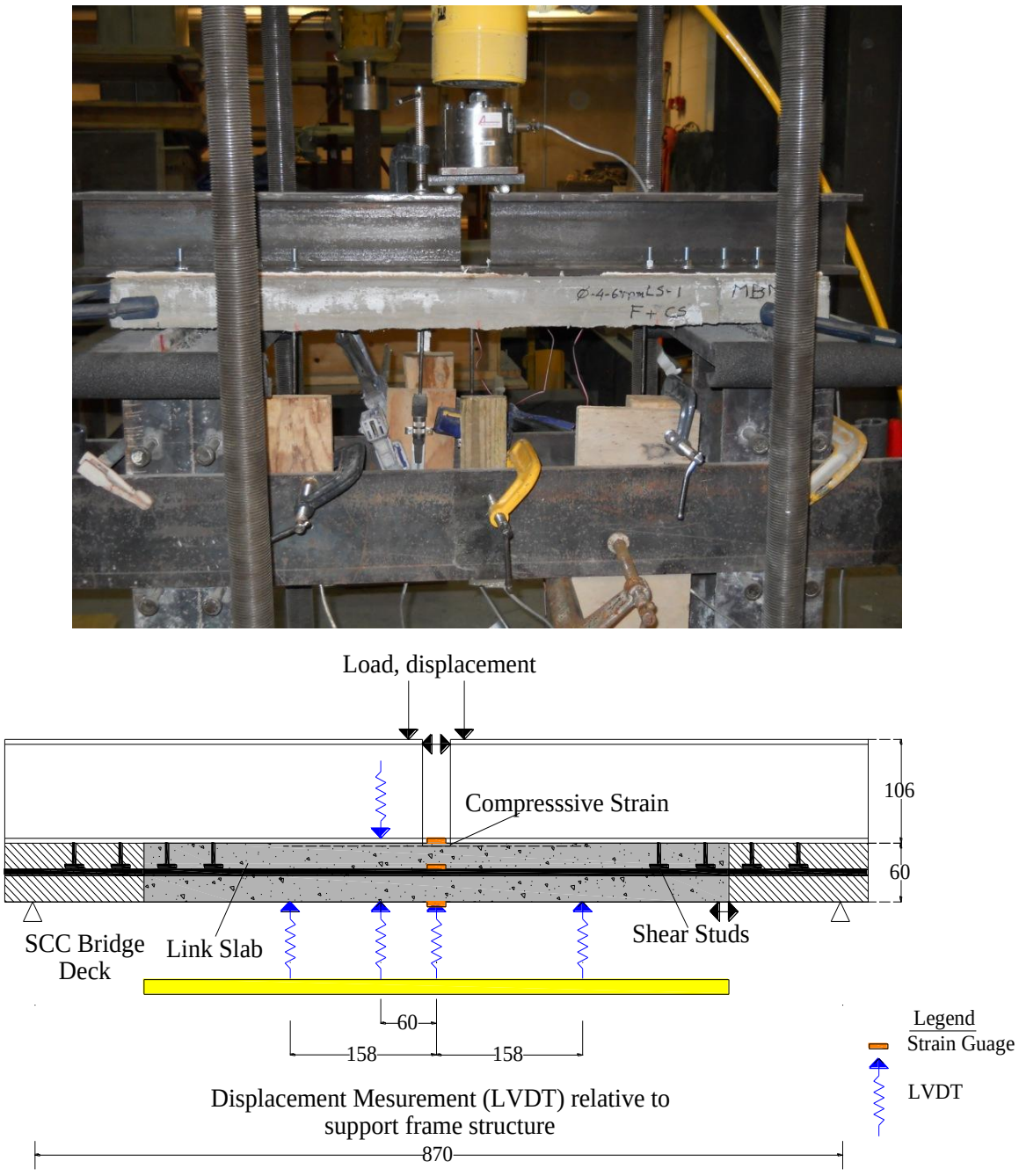

Figure 6.3 Laboratory setup and instrumentation of specimen (Dimensions are shown in mm)

6.2.4 Experimental Details and Test Arrangement

After 28 days, the link slab specimen were tested under monotonic/static loading in its upside down condition to represent the actual loading and support condition of the real bridge structure. The test set-up and instrumentation of the link slab showing location of LVDT's and strain gauges are shown in Figure 6.3. The test specimen was 930 mm long and supported symmetrically on roller pins, 870 mm apart. The girders were separated by a gap of 30 mm at the centre line of the link slab. The stain gauges were installed at the centre of the specimen to monitor the strain development in concrete and reinforcing bars. In the current test setup, the test load was applied through a hydraulic actuator at the centre of the test specimen. The load was applied gradually at a rate of 0.05kN⁄min until failure. The data was collected with a data acquisition system connected to computer. During testing, the load, displacements and strains in concrete and reinforcing steel of the specimens were monitored. The cracking, crack propagations and failure modes were also visually observed; simultaneously number of cracks and crack width were also noted with the help of crackscope.

6.3 Results and Discussion

6.3.1 Cracking Pattern

Figure 6.4 (a) shows a photo of the crack pattern. For the purpose of clarity a zoom view of the cracked zone is shown in Figure 6.4(b). Based on the cracking pattern of all specimens the following observations can be made:

For LS- 4(SCC) link slab, in the initial loading phase, a small transverse crack formed across the deck near the mid-span of the link slab. The mid-span deflection increased with the increase of load with additional cracks formation and propagation across the width of the link slab. The first crack at the centre of the link slab gradually grew wider during subsequent loading and reached 130 μm at the failure with maximum mid-span deflection of 3 mm. Ultimately, seven cracks were observed during the test.

In contrast to that, several microcracks appeared in the debonding zone of the ECC link slabs (LS-1, LS-2, LS-3) in the initial loading steps. Additional hairline cracks formed as the mid-span deflection increased. All the crack widths remained below 50 μm and the localization of the

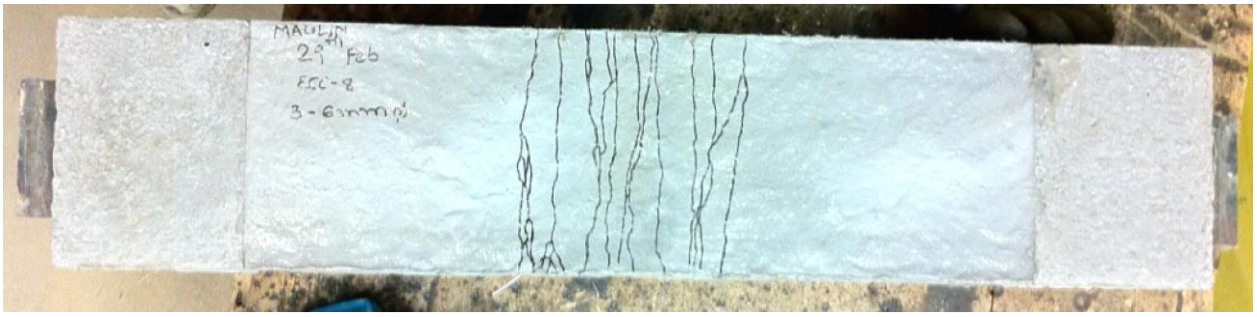

(a)

(b)

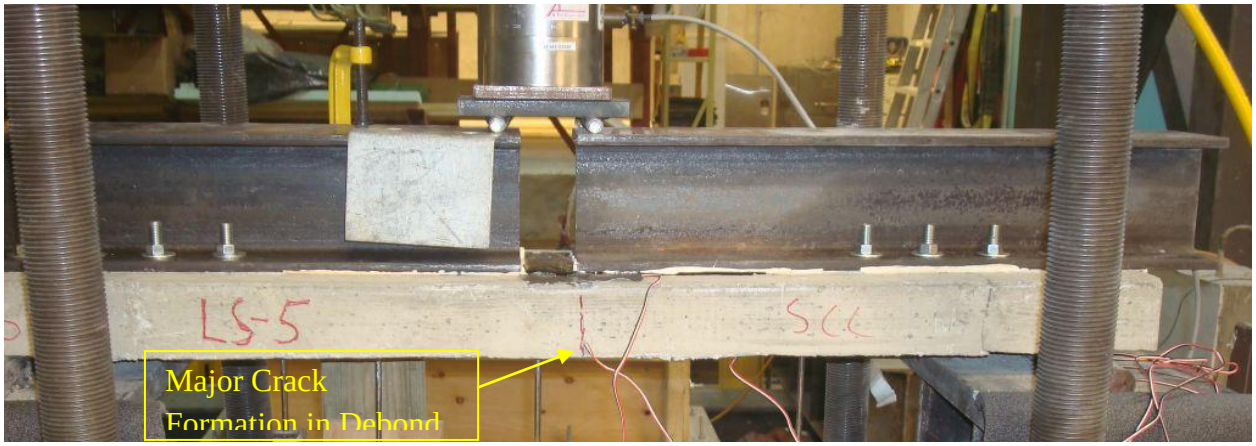

(c)

Figure 6.4 (a) Typical crack pattern of link slab, cracks are limited to the debond zone only (b) zoom view of the crackzone (marked with ink pen for clarity) (c) failure and crack pattern for SCC link slab

crack near the mid-span resulted in the failure of the link slab. The behaviour of all the link slabs with ECC was more or less same in terms of number of micro-cracks and crack width. There was a minor reduction in the number of micro-cracks, which was noticed for the LS-1 in comparison to LS-2 and LS-3 link slabs. The possible reason for this situation could be attributed to higher percentage of reinforcement, which could have imparted LS-1 additional stiffness. But this reduction in the number of cracks was very minor and can be ignored. There was no apparent difference in the performance due to change in the aggregate type (CS_F_2.2 - LS-2 and CS_F_2.2 -LS-3).

For all the specimens including LS-4 (SCC), the cracks generally extended across the entire slab width and were spaced out at a regular spacing, indicating that the link slab behaved as a flexural member. All the cracks were observed in the debonding zone only and no crack was extended into the deck slab zone. This provided with the evidence that the 5% debonding zone was sufficient to keep the stress concentration in the link slab only. All the link slabs with ECC showed more or less the similar behaviour in terms of crack pattern and number of cracks. It is worth noting that reinforcement ratio and the ECC mixture types studied under this research work has no significant influence on the number of microcracks, crack pattern and failure pattern.

6.3.2 Load-Vertical Deflection at Mid-Span

Figure 6.5 compares the load- midspan deflection responses of the four link slab specimens. No apparent difference was observed between ECC specimens (LS-1, LS-2, LS-3). The significant differences in the response of SCC specimen (LS-4) were observed compared with other ECC-specimens. The following observations can be made:

For all ECC link slabs, the load-deflection relationships showed ductile behaviour with strain hardening as evident from the steady increase in deformation with the increase in load. The link slab with SCC was brittle and failed to show the same strain hardening behaviour during the loading history, a sudden drop of load was observed followed by the major crack formation in the debonding zone. All the ECC link slabs, showed ultimate flexural strength in the range of 10.10 kN to 12.30 kN. Whereas the flexural strength observed in the case of SCC link slab was

significantly low of 4.26 kN. Accordingly, the ductility of the ECC links slabs is evident from the large deflection ranging between 10 and 13 mm at peak load compared to only 3 mm for SCC link slab.

The difference in the behaviour of ECC and SCC link slabs can be attributed to the absence of shear lag (as shown in Figure 6.6) between reinforcing bars and the surrounding ECC material in steel-reinforced ECC (R/ECC) while the brittle fracture of concrete in R/C causes unloading of concrete, resulting in high interfacial shear and interfacial bond failure (Li, 2002). The stress concentrations on the reinforcement are nonexistent even as the ECC is experiencing micro crack damage. Subsequently, the yielding of the rebar is delayed in the ECC matrix compared with that in the concrete matrix.

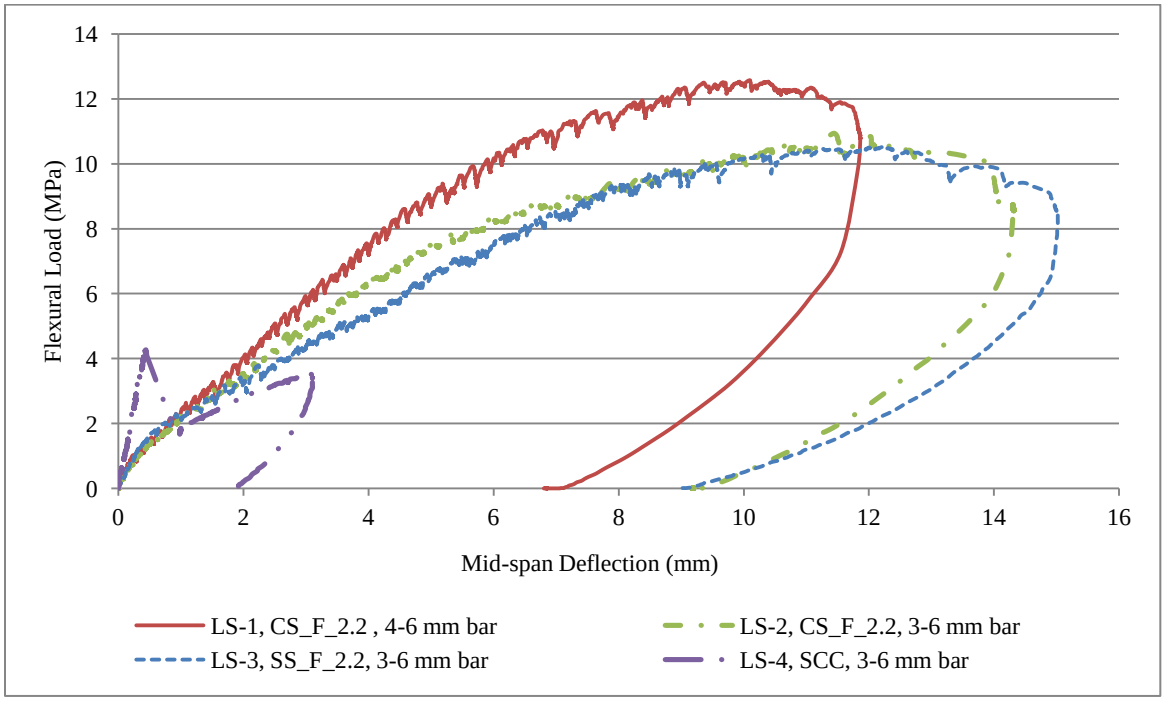

Figure 6.5 Flexural load vs. mid-span deflection of link slabs

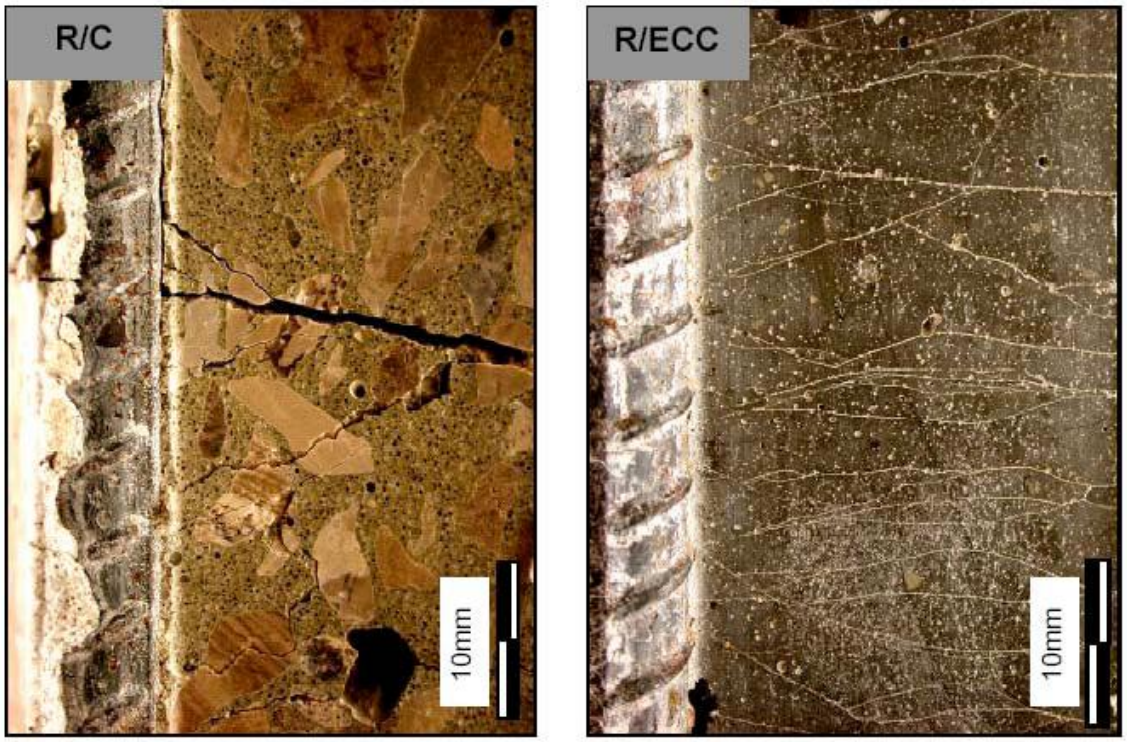

Figure 6.6 The brittle fracture of concrete in normal R/C (left) causes unloading of concrete, resulting in high interfacial shear and bond breakage. In contrast, compatible deformation between ECC and steel reinforcement (right) showing micro-cracking in ECC with load transmitted via bridging fibers (Li, 2002)

The slope of the load-deflection response for ECC specimens remained more or less constant during the loading, which indicates that the loading does not have much impact on the structural stiffness of the link slab system.

Link slabs with all three ECC mixes showed similar deflection response. However, ECC link slab (LS-1) with higher reinforcement ratio showed more stiff behaviour with higher peak load and lower peak deformation. LS-1 (with 4-6 mm bars) showed higher flexural strength and less mid-span deflection in comparison to LS-2 and LS-3 (with 3-6 mm bars). Higher reinforcement ratio was favorable for achieving higher flexural strength but at the same time, it increased the stiffness of the system and thus resulting into the lower mid-span deflection. LS-2 and LS-3 showed almost the same load-deflection behaviour illustrating no significant effect of maximum aggregate size, aggregate type on the structural behaviour of ECC in link slab.

6.3.3 Flexural Strain Development along The Cross-Section in Link Slab

Figure 6.7 illustrates the typical flexural strain distribution of ECC link slab at three locations across the midspan section at different loading step. The rebar strain of the ECC link slab (LS-1, LS-2, LS-3) was smaller than that of the SCC link slab LS-4. The difference between these rebar stresses became larger as the midspan deflection increased. This is due to the strain hardening and micro-cracking of ECC material, allowing for compatible deformation of the ECC matrix with reinforcing bars as well as due to the lower stiffness of ECC compared to SCC in compression. In a study conducted by Fischer and Li (2002) on the tension stiffening behaviour of R/C and R/ECC, strain jumps were measured locally by strain gages attached to the reinforcing bar in concrete whenever the concrete cracked, but these strain jumps were not observed in the rebar embedded in the ECC matrix. This unique behaviour is caused by ECC material exhibiting a metal-like behaviour and deforming compatibly with reinforcing bars. The micro cracks (< 50 μm in widths) developed in ECC act as inelastic damage distributed over the bulk volume of ECC. In contrast, beyond the elastic limit, ordinary concrete experienced localized fracture.

A comparison of the sequential strain development at midspan section in the three specimens confirms the strain compatibility of the ECC link slabs Figure 6.7. Because of the different distances from the neutral axis of the beam, the measured strain on the tensile face (of SCC and ECC) should be higher than that in the reinforcing bar if the beam is acting elastically. At a midspan deflection of 1.5 mm, the strain of the reinforcement became almost identical to the concrete strain at the tension face in SCC specimen. The rebar strain became even larger than the SCC strain at the tension face during subsequent loading. This indicates that the SCC in specimen LS-4 lost compatibility with the reinforcing bars due to the localized cracks. For the ECC link slabs, the difference between the strain of reinforcement and the ECC strain at tension face were maintained in a proportional manner, i.e., the three strain data points (ECC at tension face, reinforcement depth, and ECC at compression face) recorded at each step can be plotted on a straight line (Figure 6.7).

The load-deflection and strain development confirm the suitability of ECC a suitable material for link slab construction compared with SCC or other conventional concrete.

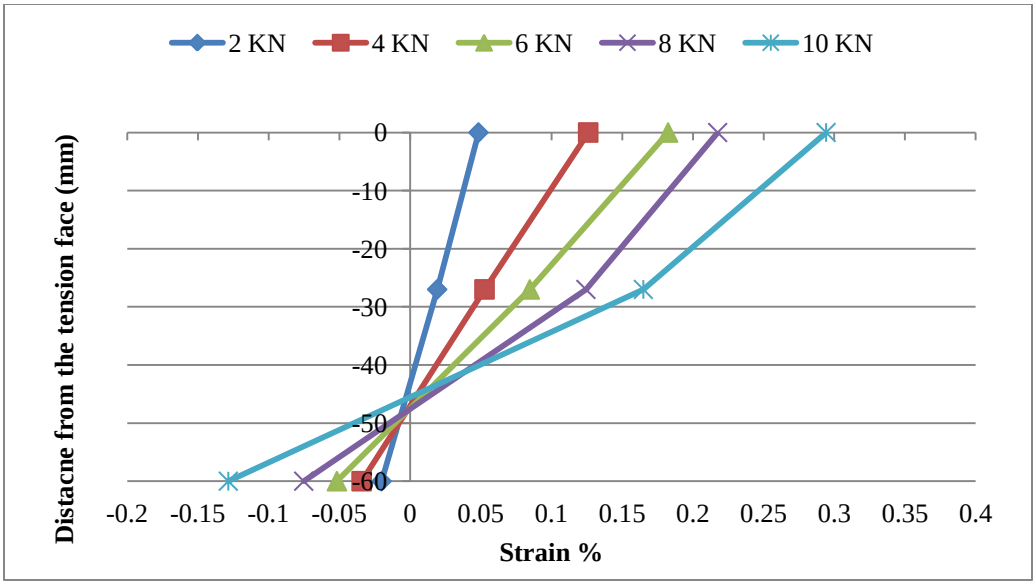

Figure 6.7 Strain distribution measured at three locations (from tension surface) across the midspan section at each loading step (step 1: 2 KN, step 2: 4 KN, step 3: 6 KN, step 4:8 KN, and step 5: 10 KN flexural loading) for typical ECC behaviour

6.4 Shear Stud-ECC Interaction Using Pushout Test

The feasibility and advantages of ECC link slab acting as a connector between two adjacent bridge deck girders are demonstrated from the load-deflection response, stress-strain development, cracking and failure modes of the system. The shear studs act as a load transfer mechanism in bridge decks especially in the transition zone of the link slab. It is important to study the shear stud-ECC compatibility by conducting push out tests. The push out provided information on the influence of ECC's ductility on shear response of stud connectors including failure mode, ultimate strength, slip capacity and over structural integrity compared with SCC counterpart.

6.4.1 Experimental Setup

6.4.1.1 Materials

Push out test was performed using a representative ECC mix CS_F_2.2. The materials and other mix design data was the same as discussed in the previous chapters. The results of the push out test of ECC were compared with the control specimen prepared with SCC. Simultaneously, the corresponding shear strength per stud was determined for both the cases. As discussed before, all

the mixes had a compressive strength of at least 35 MPa. The shear studs used in the test were 10 mm in diameter made from stainless steel conforming to ASTM A193 "Standard Specification for Alloy-Steel and Stainless Steel Bolting for High Temperature or High Pressure Service and Other Special Purpose Applications."

6.4.1.2 Preparation of Specimens and Testing

The geometry of the pushout specimen is shown in Figure 6.9. Two substrate slabs, with a dimension of 450 x 175 x 60 mm were connected with a wide flange steel beam W100 x 19 with two shear studs bolted on each side of the beam. Ideally the shear studs should be welded to the I- beam but as this was scale down model of the push out test and so as the shear studs were also comparatively small, decision was made not to weld the shear studs with the web of the I-beam. Rather bolts were joined with the help of nuts to the I-beam.

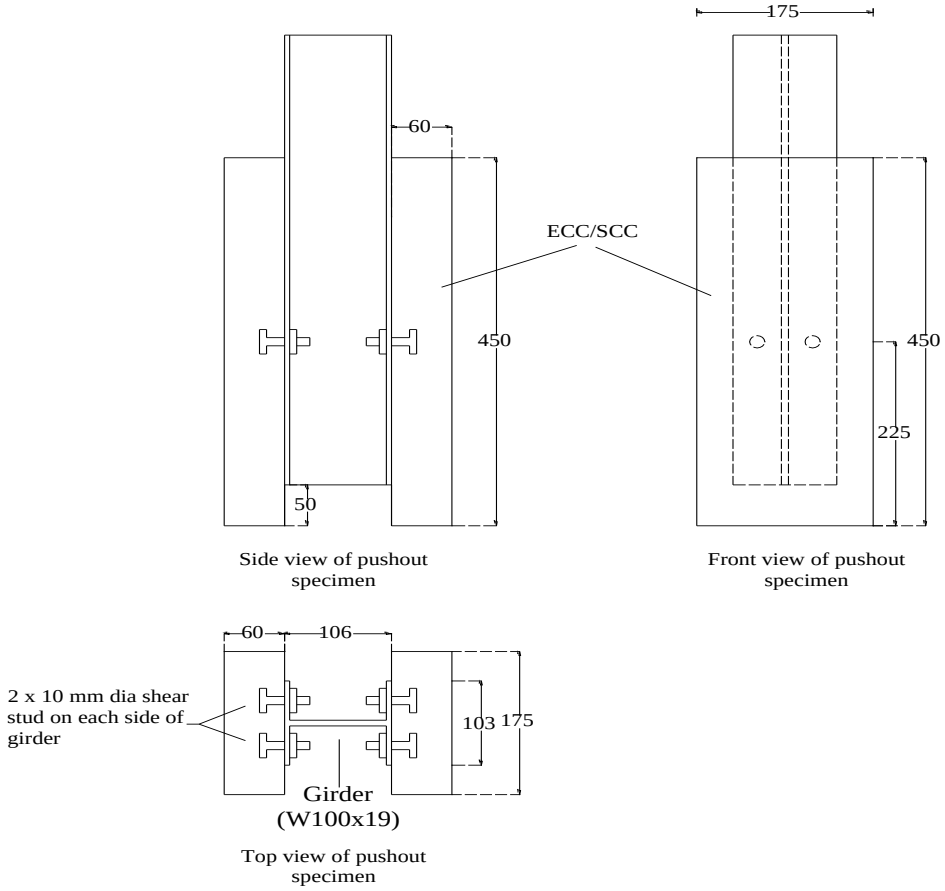

Figure 6.8 Geometry of pushout specimen (All dimensions are in mm)

Figure 6.9 Test set-up for push out test

All the specimens were cast with two numbers of 10-mm diameter shear stud on each side of an I-beam. To correlate the results of push out test and link slab size of I-beam, the dimensions of shear stud and depth of concrete were kept the same. The geometry of the push-out test was adopted from Qian and Li (2006). During casting, the material was placed from the top of the specimen. Therefore, the steel beam remained vertical to ensure that the horizontal loading plane was parallel to the bottom of the specimen. Even though this casting orientation is different from field conditions, the pouring direction is thought to be unimportant because polyvinyl alcohol (PVA) fibers in ECC are likely to be randomly distributed in a three dimensional state. To ensure the symmetry of the two slabs, the plywood molds were constructed using two integral side plates and a single bottom plate.

Both ECC and SCC specimens were cured in air while covered with the burlap at a temperature of 23 ± 2°C with RH 45 ± 5. The testing was conducted using 2224 N capacity MTS testing machine at a loading rate of 2 kN/min until failure. The push out test set up is presented in Figure 6.9. The loading surface of the specimen was grounded for uniform load distribution before testing. Load-slip relationship was obtained during the loading history using a computer aided data acquisition system. The failure modes and over all behaviour of the system were also observed.

6.4.2 Results and Discussion

6.4.2.1 Pushout Behaviour

Overall, the pushout behaviour of ECC specimens was significantly better than SCC in terms of failure mode, load/slip and structural integrity. Figure 6.10 shows the load-slip response of SCC and ECC push out specimens. As shown in Figure 6.11 and Figure 6.12, the failure mode of the stud connection switched from brittle concrete fracture in SCC to ductile multiple cracking fracture in ECC. This lead to a higher ductility of ECC/stud connections at higher peak load as indicated in Figure 6.10.

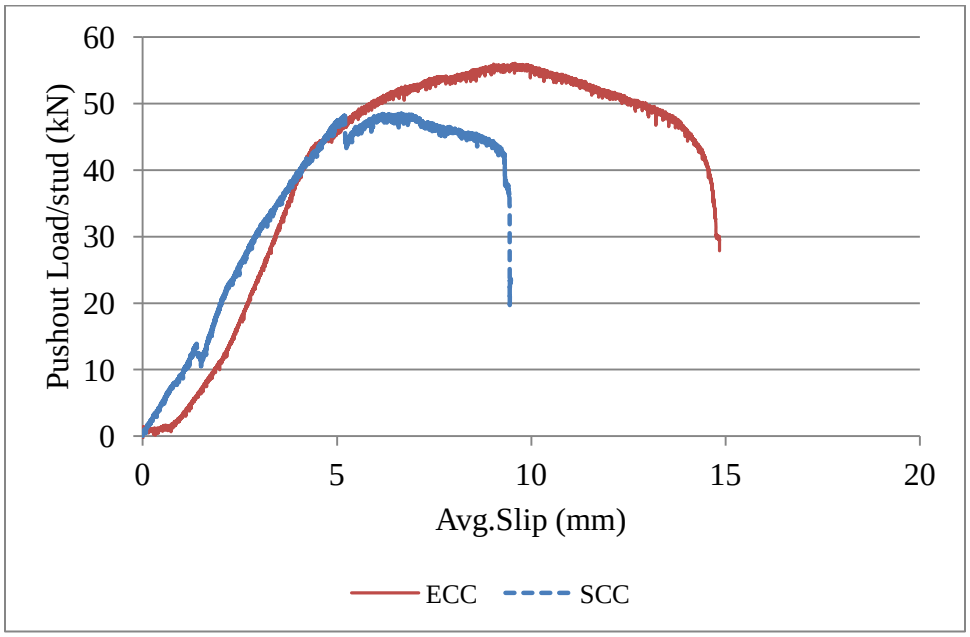

Figure 6.10 Comparison of pushout load-displacement relation for ECC and SCC

Figure 6.11 SCC pushout specimen after test showing brittle fracture macrocraks (cracks width approximately 2 mm) are observed on (a) outside; and (b) inside (natural fracture surface along shear stud) of specimen

Figure 6.12 ECC specimen after test showing ductile failure mode (crack width is approximately 40 µm). microcracks observed on (a) outside and (b) inside of the specimen.

In SCC pushout tests, as the loading approached the peak value (around 95% of peak value), large cracks (crack width of approximately 2 mm) formed in the concrete near the shear studs

and developed rapidly throughout the entire specimen as the peak load was reached. As revealed in Figure 6.11, the SCC specimen fractured into several pieces after testing, with fracture clearly initiated from near the head of the shear studs. The sudden drop after peak load in Figure 6.10 (a) demonstrates that after the SCC was fractured, the bearing resistance of SCC near the stud head was drastically reduced. The SCC under the shear stud was crushed due to the large bearing stress of the stud shank. The high stress concentration induced by the stiff steel stud combined with the brittle nature of SCC led to the rapid development of macrocracks resulting in the catastrophic failure of SCC pushout specimen. Limited yield of the steel stud at the base of the shank was observed.

On the other hands, ECC specimen showed a ductile failure mode due to their unique strain-hardening behaviour. During the linear elastic stage (Figure 6.10 b), no cracks could be observed from the surface of the ECC pushout specimens. As the load increased, a few microcracks appeared on the surface, accompanied by the beginning of inelastic range in the load-slip curve. When the peak load was reached, more microcracks radiated from the shear stud and developed outward, as shown in Figure 6.12. In some phases, a dominant crack was initiated, but diffused into many microcracks (microcrack width = 50 ± 20 μm) due to the ductile nature of ECC in tension and propagated slowly. Because the ECC near the stud head developed a large microcrack zone and the bearing side resisted the compressive force well, the ECC load-slip curve showed a large inelastic range (Figure 6.10). The large slip capacity shown in the ECC specimen indicated the feasibility of engaging adjacent shear studs in sharing the shear load and improving the composite action between steel girder and concrete bridge deck.

In the case of ECC, the peak load was associated with the localization of one of the microcracks into a fracture, even though fracture of the steel shank eventually led to a drastic load-drop, which suggested that the ductility of the ECC and the steel stud are fully used. Overall, this indicated that the replacement of conventional concrete by ECC materials allowed for plastic yielding of the matrix material, resulting in a large deformation of the stud shank, and finally a shift of the failure from concrete brittle fracture to ductile damage process of ECC materials and eventual fracture of the stud shank after extensive plastic deformation.

6.4.2.2 Load-Carrying Capacity of Stud Connection

According to the AASHTO LRFD (2004) code, the ultimate strength (Q_n) of a concrete/stud connection can be derived from eq. 6.1

$$Q_n = \min \begin{Bmatrix} 0.5Asc\sqrt{f`_cE_c} \\ \text{or} \\ A_{sc}F_u \end{Bmatrix} \quad (6.1)$$

Where A_{sc} = cross-sectional area of a stud shear connector (mm^2) = 78.54 mm^2 in the present experiment; f_c' = specified 28-day compressive strength of concrete (MPa); E_c = elastic modulus of concrete (MPa); and F_u = ultimate tensile strength of a stud shear connector (MPa).

Table 6.2 Material properties and structural behaviour of ECC and SCC pushout specimens

Material	ε_u, %	f'_c, MPa	E_c, GPa	Q_n, kN	Q_m, kN	S_c, mm	w_c, μm
SCC	0.01	62.3 ± 1.37	31.6 ± 2.45	55.10	48.49	5.85	≈ 2000
ECC	2.5 ± 0.3	45.34 ± 2.43	18.1 ± 1.4	35.57	56.06	9.91	50 ± 20

Notes: ε_u = uniaxial tensile strain capacity; f'_c = compressive strength; Ec = modulus of elasticity; Qn = computed strength per stud; Qm = measured strength per stud; Sc = slip capacity (average slip at peak load); and w_c = crack width at peak load.

Table 6.2 shows the computed ultimate strength Q_n of a shear stud in the matrix, assuming the validity of AASHTO equation for all concrete materials, along with measured strength Q_m, slip capacity S_c, and crack width w_c. In all cases, the computed Q_n is governed by $0.5Asc\sqrt{f`_cE_c}$, which is lower than $A_{sc}F_u$ (43.67 kN). Table 6.2 revealed that the measured strength of an ECC stud connection was much higher than that of a concrete stud connection even though the computed strength of the ECC stud connection should be approximately the same or even lower than that of the concrete stud connection. This suggested that material ductility of ECC played a more significant role than compressive strength in improving the connection response.

The measured strength of the studs in SCC is 48.49 kN, within 12 % of the calculated value of 55.10 kN. In the test, brittle fracture of conventional concrete was the dominant factor controlling the peak load. This could have happened as a result of its higher brittleness with increasing compressive strength. Therefore the AASHTO design equation may not give a conservative prediction when the compressive strength of concrete increases.

The measured strength Q_m of a stud in ECC was approximately 56.06 kN, approximately 36 % higher than the calculated values Q_n, and 14 % higher than the measured strength of SCC. This is mainly due to the fact that the compressive strength, a main contributing factor in the AASHTO equation for design of studs in concrete, is not necessarily relevant to the failure of ECC stud connections. Instead, the initial high stress concentration induced by the stud/ECC interaction caused yielding of the ECC, resulting in stress redistribution and delay of fracture localization in the ECC, thus leading to a higher load capacity of the ECC specimens. Therefore, the direct adoption of the AASHTO equation for ECC material will be excessively conservative. The actual failure mechanism of ECC specimens, that is, fracturing of the stud shank near the welds, suggests that $A_{sc}F_u$ may be used to better predict the load capacity. Furthermore, the greatly enhanced ductility and structural integrity of ECC/stud connection need to be addressed in the design procedure if ECC were to be used in stud connections of composite structures.

6.5 Summary

This chapter described the ECC performance in link slabs compared with SCC based on experimental testing. Experimental investigation demonstrated that as a characteristics of ECC, several microcracks (< 50 μm) appeared in the debonding zone of all the ECC link slabs (LS-1, LS-2, LS-3) which remained below. The high tensile ductility allowed the ECC matrix to deform compatibly with the reinforcing bars in link slabs. As a result, yielding of the rebar was delayed in the ECC matrix when compared with that in the SCC matrix. On the other hand, the higher reinforcement ratio imparted unwanted stiffness in the link slab and thus proved that reinforcement could be further reduced in link slab when conventional concrete is replaced by ECC. Results from the pushout test suggest the compatibility of ECC on the shear response of stud connections. Moreover, stud connectors in ECC can achieve much higher shear strength and slip capacity and provided with the evidence that the good structural performance requires a balanced material strength and ductility. ECC proves to be one unique type of high performance fiber-reinforced cementitious composite (HPFRCC) satisfying this requirement.

CHAPTER SEVEN

CONCLUSIONS AND RECOMMENDATIONS

7.1 Summary

This thesis describes the influence of aggregate type, maximum aggregate size and different types of supplementary cementitious material (SCM)s on the fresh, mechanical and durability performances of ECC mixtures. Developed ECC mixtures contain SCMs (class CI, class F FA or slag) with SCM/cement ratio of 1.2 or 2.2, aggregates of two different types namely microsilica sand and crushed sand with maximum sizes of 0.4 or 1.19 mm. Altogether ten ECC mixes were selected to evaluate their fresh (slump flow, flow time, setting time and heat of hydration) and mechanical properties (compressive strength, flexural strength). The best three mixes were selected from ten mixes based on their performance in fresh and mechanical properties (specifically flexural properties) for further investigations. These three mixes were further tested to understand their durability performance under different environmental conditions (rapid chloride ion penetration resistance, drying shrinkage, rapid freeze-thaw, water absorption and porosity, sorptivity and accelerated reinforcement corrosion of reinforcement). In the last phase, the performance of these three ECC mixtures compared with a control self-consolidating concrete (SCC) was investigated by conducting small scale ($1/4^{th}$) model tests of bridge deck link slabs (made with three ECCs and SCC) under static monotonic flexural loading in addition to pushout tests conducted to study the performance of shear stud embedded in ECC compared to SCC.

7.2 Conclusions

The following conclusions are drawn from this study:

Fresh Properties

- SL-ECC was more sensitive to high range water reducing admixture (HRWRA) content and prone to bleeding more rapidly than FA-ECC.

- Slump flow for class F FA-ECC was in the range of 530 mm to 550 mm where as it was in the range of 500 mm to 540 mm for class CI FA-ECC. It was clear that class F FA-ECC was more flowable than class CI FA-ECC.
- Over all, the fresh properties of all ECC mixes were satisfactory. All the mixes showed no signs of bleeding. As coarse aggregate was not present in the mix, so segregation is not applicable term for ECC. But sometimes balling of fibers was observed due to excessive addition of HRWRA and this phenomenon was considered as segregation for ECC.
- Significant effect of type and volume of supplementary cementitious material was observed on the hydration curves of ECC mixes. Higher CaO content was resulted in higher hydration peak of slag-ECC which was followed by class CI FA and lowest was observed for class F FA-ECC. Similar effect was observed in the case of setting time. Slag-ECC made the setting of ECC faster and resulted in lower setting time compared with FA-ECC. Fly ash F ECC showed highest setting time.
- The higher surface area and amorphous nature of the microsilica sand accelerated hydration of C3S, C2S, and C4AF and was responsible for higher heat of hydration and lower setting time compared with mixes with crushed sand as an aggregate.

Mechanical Properties

- All ECC mixtures, attained compressive strengths higher than 45 MPa at the age of 28 days which significantly exceeded that of normal concrete. Among FA-ECC, class CI FA-ECC obtained higher compressive strength compared with class F FA-ECC due to higher CaO content.
- Unlike conventional concrete, aggregate characteristics, such as the surface texture and maximum aggregate size, did not influence the compressive properties in the case ECC and at each SCM replacement level, crushed sand ECC obtained slightly lower compressive strength (in the range of 90% to 95%) than microsilica sand ECC.
- For all aggregate types (crushed sand or silica sand), ECC specimens with an SCM/cement (C) of 1.2 exhibit significantly higher ultimate flexural and compressive strengths, whereas the ECC specimens with higher SCM content exhibit more ductile behaviour.

- In this study, the FA-ECC mixtures irrespective of type of fly ash (CI or F), irrespective of the maximum aggregate sizes and aggregate type exhibited strain-hardening behaviour with deformation capacities better than the standard ECC mixtures.
- ECC mixtures with microsilica sand and crushed sand exhibited similar flexural strength and mid-span deflection capacity due to use of high volumes of FA which reduced the fiber/matrix interfacial chemical bond and lowered the matrix toughness.
- The average crack width on the surface of the specimen was lower than 90 μm for slag-ECC mixtures and 60 μm for FA-ECC mixtures. In slag ECC, cracks were also spaced further apart than in FA-ECC. On the other hand, the use of aggregate up to 1.19 mm maximum size did not influence the average residual crack width.

Durability Properties

- Compared to class CI FA-ECC with class F FA revealed slightly higher chloride ion penetration resistance and vaguely less drying shrinkage due to denser matrix arrangement because of fine particle size of class F FA. Nevertheless, the results of class CI FA-ECC were in the same range. No significant role of size of aggregate on the drying shrinkage and chloride ion penetration is observed for a given aggregate content. The ultimate drying shrinkage of ECC slightly decreases with increase in the size of aggregate from 0.4 mm to 1.19 mm.
- Test results of the freeze-thaw test results showed that apart from the slight reduction in mass, residual ultimate flexural strength and ductility remained intact, which confirmed that ECC provides excellent frost protection. Increase of aggregate size resulted into slightly higher loss in flexural strength (about 8% higher loss) but the deflection capacity was not affected. It is important to note that this superior durability performance of ECC under freezing and thawing cycles was achieved without deliberate air-entrainment. For this reason, it is expected that all developed ECCs will be suitable for long-term application under severe environmental conditions. Experimental evidence indicates that the excellent frost durability of ECC was due to the intrinsically high tensile ductility and strength attained as a result of micro-mechanically based design principles. The presence of micro-PVA fibers critically contributes to the higher crack

resistance and larger pore volume, and resulting pressure releasing effects under freeze-thaw conditions.

- The increase of aggregate size from 0.4 mm to 1.19 mm increased the absorption and sorptivity just by 3% to 5%. Change of fly ash type did not definitely affect the absorption and sorptivity. The absence of coarse aggregate, higher replacement of fly ash and lower water to binder ratio was responsible for lowering sorptivity and absorption values.
- All ECC specimens irrespective of aggregate type, size and type of SCM (class F of CI FA), exhibited superior corrosion resistance in terms of corrosion propagation time, tight crack width, lower weight loss, and higher retention of stiffness and flexural load which can be attributable to the high tensile strain capacity, strain hardening, and multiple-cracking behaviour. Crack widths (~0.1 mm) of ECC remained nearly constant with time as corrosion activity progressed, whereas the number of cracks on the surface of the ECC specimens increased. ECC also exhibited significant anti-spalling ability compared with conventional mortar. If a crack width of 0.3 mm (0.012 in.) is used to set a service time limit of reinforced concrete (RC) structures, the service life of reinforced ECC (R/ECC) will be at least 15 times higher than that of the reinforced mortar.
- The flexural capacity of ECC specimens decreased but retained over 45% that of the control specimen, even after 300 hours of accelerated corrosion exposure. There is no apparent difference in the corrosion resistance behaviour of the ECC specimens with different fly ash and different aggregate type and size. All the specimens showed the mass loss of the reinforcement in the same range (23 to 25%). Generally longitudinal cracks due to expansion of the corrosion products affect the failure mode of the under four-point bend test. The corrosion of steel bar in ECC specimens did not change the type of failure in ECC beams. These experimental findings suggest that the propagation period of corrosion could be safely included in estimating the service life of a structure when conventional concrete is replaced by ECC.

Structural Performance

- For all the link slabs (including LS-4, SCC), the cracks generally extended across the entire slab width and were spaced out at a regular spacing, indicating that the link slab

behaved as a flexural member. Crack formation only in debonding zone proved that the 5% debonding zone was sufficient to keep the stress concentration in the link slab only.

- Steady increase in deformation with the increase in load proved strain hardening behaviour of all ECC link slabs, which SCC failed to show by sudden drop of load followed by major crack formation in debonding zone. Ultimate flexural strength and mid-span deflection capacity of ECC link slab was marginally higher (about 275% and 400%) than that of SCC link slab.
- From the monotonic static testing, it was found that the maximum tensile strain in the ECC link slab measured at different loading level remained within the early strain-hardening regime. This confirmed the adequacy of the strain capacity of the ECC used in this study. Indeed, there is a room to employ an ECC with slightly lower tensile strain capacity, (which was evidenced by providing lower percentage of reinforcement) with potential material cost saving.
- While the control SCC pushout specimen failed by brittle fracture associated with a lower ultimate strength, ECC pushout specimen failed gradually by ductile yielding of ECC materials and plastic deformation of steel stud, resulting in a higher load-carrying capacity, even though fracture of the steel shank eventually led to a drastic load-drop. This significant enhancement of ductility suggests that the use of ECC material can be effective in redistributing loads among the shear studs and in improving composite action between steel girder and concrete bridge deck.
- The AASHTO LRFD bridge design equation for load carrying capacity of stud connection overestimates load carrying capacity in the case of higher strength concrete (SCC in this case) due to increased brittleness. Conversely, this equation was found to underestimates the load capacity of ECC/stud connections because it cannot take into account the actual failure mechanism of the ECC pushout specimens. A revised predictive equation governing strength of stud connectors accounting for ECC material ductility needs to be developed.

The results presented in this study demonstrates viability of producing greener sustainable ECC using locally available aggregates (crushed sand having relatively higher nominal aggregate size) instead of fine silica sand and fly ash (Class CI or F) of up to 70% cement replacement having

similar or better mechanical/ durability properties and structural performance. ECC mix designs proposed in this study can be used as guidelines for production of greener ECC for construction applications.

The experimental investigation also demonstrated the feasibility and advantages of ECC material in the construction of link slabs for joint free bridge decks. However, more investigations are needed on link slab applications and extensive research consisting of experimental and numerical investigations are now in progress at Ryerson University. Such research includes small scale/full scale testing of link slabs as well as complete bridge deck with link slab under static, fatigue and sustained (creep) loading conditions. The final aim of the research is to produce specifications for ECC design especially tailored for link slab as well to develop design guidelines for link slabs for jointless bridge construction. The results of the current study surely contributed to the overall research.

7.3 Recommendation for Future Research Studies

Based on the research described herein, it is recommended that:

Greener, sustainable and cost-effective ECC mixtures should be developed by incorporating locally available aggregate of different type and size other than studied under this research and their fresh, mechanical and durability properties should be studied.

Guidelines should be formulated for (i) ECC mix design; (ii) testing methods/protocol for ECC performance evaluation and (iii) identification of critical ECC properties for contract specifications.

Consideration can be given to use ECCs in the link slab to improve flexural properties of concrete, crack control and environmental loading resistance.

Further analysis and testing of link slab should be conducted using different ECC mixtures. Simultaneously, full-scale link slab for jointless bridge deck should be conducted using established mix designs under this research work.

Tests on full scale jointless bridge decks with simply supported girder should be conducted under repeated loading to evaluate the effect of fatigue on the behaviour of link slab. Simultaneously, test should be conducted under sustained loading to evaluate the effect of creep on the behaviour of link slab.

Numerical investigation should be carried out using finite element modelling for better understanding of link slab behaviour in a jointless bridge deck.

A revised predictive equation based on experimental and numerical investigation should be formulated for strength of stud connectors taking into account ECC material ductility.

The development of design guidelines should be carried out for ECC link slabs including development/modification of existing design equations for overall moment capacity based on experimental and theoretical/design oriented analyses.

APPENDIX A

The link slab design in this investigation was designed under American Association of State and Highway Transportation Officials LRFD Bridge Design Manual (2004) .

The full scale model dimensions were 3250 x 711x 229 mm (L x B x D) So the dimensions of ¼th scale model would be 902 mm x 177.75 mm x 57.25 mm. For the ease of calculation it was considered as 930 mm x 175 mm x 60 mm.

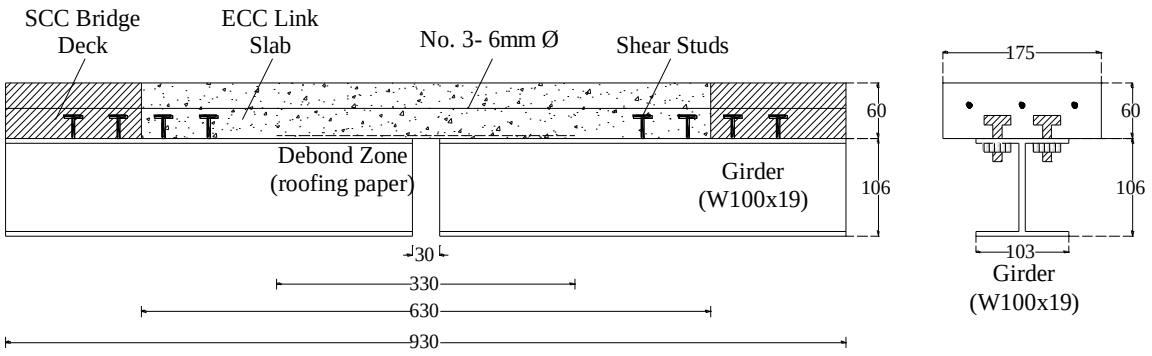

Figure A.1 Geometry of link slab specimen

The overall length of the link slab and the length of the link slab debond zone are calculated as per Eqs. 1 and 2, respectively. Based on the full scale model the length of link slab and debond zone was decided.

$$L_{ls} = 0.075(L_1 + L_2) + G_{1-2} \quad (1)$$

L_{ls} = 630 mm

$$L_{dz} = 0.05(L_1 + L_2) + G_{1-2} \quad (2)$$

L_{dz} = 330 mm

Where, L_{ls} is the overall length of the link slab in millimeters, L_1 and L_2 are the span lengths of the two adjacent bridge spans in millimeters, G_{1-2} is the length of any gap between the girders of the two adjacent spans in millimeters, and L_{dz} is the length of the link slab debond zone in millimeters. Zia et al. (1995) found that up to 5% of the adjacent deck may be debonded without affecting the composite action (between deck and girder) design assumption of the adjacent spans.

Outside of the debond zone on either end of the link slab are transition zones in which shear connection and composite action between girder and deck are re-established. Due to the high shear stresses within the region, the number of shear connectors required by the design code is increased by 50%. The design of shear connectors in concrete according to the AASHTO design code has been shown conservative for shear connectors in ECC material. It is recommended to use the standard AASHTO design procedure for design of shear connectors (Li et al., 2003).

As the reinforcement ratio of the concrete link slab was determined to satisfy the stress criterion ($\sigma_s < 0.40\sigma_y$) at a 0.0015 rad. end rotation angle. This is the expected rotation angle as derived by Caner and Zia (1998).

The uncracked moment of inertia I_{ls} is computed for the link slab per meter width of bridge deck in mm^4, as

$$I_{ls} = \frac{(1000\ mm)t_s^3}{12} \tag{3}$$

$$I_{ls} = \frac{1000\ x\ 60^3}{12}$$

$I_{ls} = 18 \times 10^6\ mm^4$

The moment M_{ls} developed in the uncracked concrete link slab is a function of the elastic modulus of concrete E_c and geometrical dimensions. It is proportional to the imposed end rotation angle θ as shown in Eq. 4.

$$M_{ls} = \frac{2E_{ECC}.I_{ls}.0.001}{L_{dz}}.\theta_{\max} \tag{4}$$

$$M_{ls} = \frac{2\ x\ 20\ x\ 18\ x\ 10^6\ x\ 0.001\ x\ 0.0015}{330}$$

$$M_{ls} = 3.273\ KN.m$$

where M_{ls} is the moment induced into the link slab per meter width of bridge deck in kN-m, E_{ECC} is the elastic modulus of ECC material in GPa, I_{ls} is the uncracked moment of inertia of the link slab in mm^4 (Eq. 3), L_{dz} is the length of the link slab debond zone in millimeters (Eq. 2), and θ_{max}

is the maximum end rotation angle of the adjacent spans in radians (0.0015). The elastic modulus of ECC material is typically assumed as 20 GPa.

The moment induced in the link slab by the rotation of adjacent bridge spans, M_{ls}, can be viewed as the ‘‘moment demand’’ placed on the ECC link slab. Therefore, the uncracked moment of inertia of the link slab, I_{ls}, is used in Eq. 4. While the ECC link slab is designed and intended to function in the microcracked state (with lower moment of inertia), this higher calculation of moment demand introduces additional conservatism and safety into the ECC link slab design. This also compensates for the slight increase in sectional stiffness which would be calculated if the stiffness contribution from steel reinforcement was included. Further calculations show that ignoring this contribution of steel reinforcements to M_{ls} leads to negligible error.

Viewing M_{ls} as the imposed ‘‘moment demand’’, the amount of steel reinforcement within the ECC link slab must be calculated to resist this moment. The amount of steel reinforcement within the link slab is based entirely on structural load capacity and not on any crack width serviceability requirements since large tensile cracks do not form in ECC under normal load conditions (Lepech et al., 2006). To calculate the moment capacity of the ECC link slab section, a non-linear sectional analysis is used based on the assumption that ECC material remains perfectly elastic-plastic in service. While ECC material typically does show some strain hardening characteristics after first cracking, this strength gain will not be relied upon to once again promote conservative design practice.

Based on the previous studies of application of ECC`s link slab application, the ‘‘yield strain’’ for the all these different ECC mixes is set at 0.02%. The ‘‘yield stress’’ of the ECC material is set at 3.45 MPa. While the actual ultimate strength is typically above this value, 3.45 MPa was again chosen as a statistically representative value from the pool of tensile test results. (Lepech & Li, 2009).

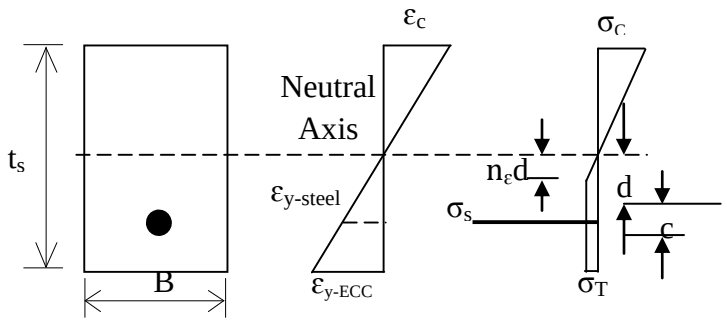

Figure A.2 Stress and strain distribution in the ECC link slab cross section carrying a negative moment

As proposed by Caner and Zia (1998), a conservative working stress of 40% of the yield strength, f_y, of the steel reinforcement is used for design. Unlike the design assumptions for concrete, in which no tensile force is carried by the concrete, a substantial stress of 3.45 MPa is assumed to be carried by the ECC up to failure between 2 and 3% strain. Using non-linear analysis and the assumption of a linear strain distribution within the section, shown in Figure A.2, the moment capacity of the section can be computed for any steel reinforcing ratio. The reinforcement ratio is then adjusted accordingly to resist the moment due to maximum end rotation computed earlier in Eq. 4. Figure A.2 also shows the cross sectional stress distribution of a reinforced ECC link slab (R/ECC).

To compute the moment capacity of the ECC link slab section, the location of the neutral axis of the section is determined through force equilibrium. However, prior to performing force equilibrium, the location of the stress ‘‘kink’’ in the tension region of the section, due to the elastic-plastic tensile response of ECC material, is calculated. As a result of the linear strain assumption within the section, this is done using geometry and the ratio of yield strains of steel and ECC, along with the assumption of 40% working stress in the reinforcing steel. This is shown in Eq. 5.

$$n_\varepsilon = \frac{\varepsilon_{y-ECC}}{0.4.\,\varepsilon_{y-steel}} \tag{5}$$

$$n_\varepsilon = \frac{0.02}{0.4\ x\ 0.08}$$

$$n_\varepsilon = 0.625$$

where n_ε is the yield strain ratio, $\varepsilon_{y\text{-}ECC}$ is the ‘‘yield strain’’ of the elastic-plastic ECC behaviour (0.02%), and $\varepsilon_{y\text{-}steel}$ is the yield strain of the reinforcing steel.

Equilibrium balance of the section is enforced to determine the location of the neutral axis. A preliminary reinforcement ratio is then selected for iterative design. In this case preliminary reinforcement ratio was chosen as ρ = 0.1 % (which is the minimum requirement of reinforcement ratio as per AASHTO). The moment capacity of the ECC link slab based on this reinforcement ratio is determined and this capacity is compared to the moment induced (i.e. demanded) in the slab the beam end rotation (from Eq. 4). If moment capacity for the selected reinforcement ratio is below the moment induced, a higher reinforcement ratio is chosen and a second design iteration is performed.

Equations 6a–d are used to calculate the force within the reinforcing steel, tensile portion of ECC material, and compressive portion of ECC material per meter width of bridge deck. Equilibrium balance is completed by solving a simple non-linear equation, shown in Eq. 6e. The goal of this calculation is the determination of the value for ‘‘d’’.

$$T_{steel} = \left(0.4.\, f_{y-steel}\right)\rho.\, t_s \qquad (6a)$$

$$T_{steel} = (0.4\ x\ 410)0.01x60$$

$$T_{steel} = 98.4\ KN$$

$$T_{ECC-1} = f_t'\left((1 - n_\varepsilon)d + c\right) \qquad (6b)$$

$$T_{ECC-1} = 3.45((1 - 0.625)d + 24)$$

$$T_{ECC-2} = \ 0.5.\, f_t'.\, n_\varepsilon.\, d \qquad (6c)$$

$$T_{ECC-2} = \ 0.5x\ 3.45\ x\ 0.625x\ d$$

$$T_{ECC-2} = 1.078125.\, d$$

$$C_{ECC} = 0.5.\, f_t'\left(\frac{1}{n_\varepsilon d}\right).\,(t_s - d - c)^2 \qquad (6d)$$

$$C_{ECC} = 0.5\ x\ 3.45\left(\frac{1}{0.625xd}\right)(60 - d - 24)^2$$

$$C_{ECC} = 0.5\ x\ 3.45\left(\frac{1}{0.625xd}\right)(60 - d - 24)^2$$

$$T_{ECC-1} + T_{ECC-2} + C_{ECC} = 0 \qquad (6e)$$

Now solving equation 6(a) to 6(e)

$$98.4 + 1.294d + 82.8 + 1.078d + \frac{3576.96}{d} - 198.72 + 2.76d = 0$$

$$181.2d + 2.372d^2 - 3576.96 + 198.72d - 2.76d^2 = 0$$

$$d^2 - 979.17d + 9218.96 = 0$$

By solving the above equation we get

$$d = 9.50\ mm$$

Replacing the same in equation (ii) to (iv)

$$T_{steel} = 98.4\ KN$$

$$T_{ECC-1} = 3.45\big((1 - 0.625)d + 24\big)$$

$$T_{ECC-1} = 95.09\ KN$$

$$T_{ECC-2} = 1.078125.d$$

$$T_{ECC-2} = 10.242\ KN$$

$$C_{ECC} = 0.5\ x\ 3.45\left(\frac{1}{0.625xd}\right)(60 - d - 24)^2$$

$$C_{ECC} = -204.02\ KN$$

where T_{steel} is the tension force in the reinforcing steel per meter width of bridge deck in kN, $f_{y\text{-}steel}$ is the yield strength of the steel in MPa, ρ is the steel reinforcement ratio, t_s is the deck slab thickness in millimeters, $T_{ECC\text{-}1}$ and $T_{ECC\text{-}2}$ are tension forces in the ECC per meter width of bridge deck in kN, f_t` is the assumed tensile strength of the ECC material in MPa, n_ε is the yield strain ratio computed using Eq. 5, d is the distance from the neutral axis to the centroid of reinforcing steel in millimeters, c is the distance from the tensile face of the slab to the centroid of the reinforcing steel in millimeters, C_{ECC} is the compressive force in the ECC slab per meter width of bridge deck in kN. Dimensions are shown graphically in Figure A.2.

Using the force in each portion of the section along with the location of the neutral axis, the moment resisting contribution of each portion is used to compute the overall moment capacity of the link slab, shown in Eq. 7.

$$M_{r-ls} = \left\{ T_{steel}.d + T_{ECC-1}\left(\frac{(1-n_\varepsilon).d + c}{2} + n_\varepsilon.d\right) + T_{ECC-2}.\left(\frac{2}{3}\right).n_\varepsilon.d + C_{ECC}\left(\frac{2}{3}\right).(t_s - d - c)\right\}\left(\frac{1}{1000}\right) \quad (7)$$

Where $M_{r\text{-}ls}$ is the resisting moment capacity provided by the link slab per meter width of bridge deck in kN-m. The moment resistance, $M_{r\text{-}ls}$, calculated from Eq. 7, is compared to the moment demand induced by the imposed end rotations, M_{ls}, from Eq. 4. Starting with an assumed value for ρ, if the resistance so determined is greater than the demand, the strength design is completed using the selected reinforcement ratio. Otherwise, a higher reinforcement ratio is selected and the process iterated.

$$M_{r-ls} = \left\{ 98.4\ x\ 9.50 + 95.09\left(\frac{(0.375x9.50) + 24}{2} + 0.625x9.50\right) + 204.02\left(\frac{2}{3}\right)x\ (60 - 9.50 - 24)\right\}\left(\frac{1}{1000}\right)$$

$$M_{r-ls} = 6.455\ KN.m$$

$$M_{ls} \leq M_{r-ls}$$

So OK.

Finally, a specific reinforcing steel bar is selected and the required bar spacing is calculated using Eq. 8. Where S is the spacing between the bars in millimeters, A_{bar} is the cross sectional area of the selected reinforcing steel bar size in mm^2, ρ is the finalized reinforcement ratio, and t_s is the deck slab thickness. In this design 6 mm ϕ bar was chosen and the spacing was calculated as per Eq. 8 So finalized reinforcement design was 3-6 mm ϕ bars. As per the nominal steel requirement transverse reinforcement was chosen as 6 mm ϕ bar (a) 150 mm c/c.

$$S = \frac{A_{bar}}{\rho t_s} \tag{8}$$

$$S = \frac{28.27}{0.1x60} x\ 100$$

$$S = 47.11\ mm\ \approx 50\ mm$$

To understand the effect of reinforcement ratio on the behaviour of link slab other higher reinforcement ratio was chosen and the same procedure was repeated. Due to higher reinforcement ratio the resisting moment of link slab was coming out to be $M_{r-ls} =\ 6.689\ KN.m$

And due to higher reinforcement ratio 4-6 mm ϕ bars with the same transverse reinforcement ratio was the detail for the link slab with ρ = 0.12 %. As mentioned earlier, design of shear stud was performed as per the guidelines of AASHTO LRFD bridge design code.

REFERNCES

AASHTO, 2004. *LRFD Bridge Design Specifications,* Washington, DC: AASHTO.

ACI Committee 116R, 1994. *Cement and Concrete Terminology.* Detroit, Michigan: ACI manual of concrete practice.

ACI Committee 224R, 2001. *Control of Cracking in Concrete Structures.* Farmington Hills, Michigan: American Concrete Institute.

ACI Committee 318, 1995. *Building Code Requirements for Structural Concrete (ACI 318-95) and Commentary (318R-95),* Famington Hills, MI: American Concrete Institute.

Alampalli, S. and Yannotti, A. P., 1998. In-Service Performance of Integral Bridges and Jointless Decks. *Transportation Research Record 1624,,* 1624(0540).

Andrade, C., Sanjuan, M. A. and Alonso, M. C., 1993. *Measurement of Chloride Diffusion Coefficient from Migration Tests.* Houston, Texas, NACE Corrosion '93.

ASTM C618, 2012. *Standard Specification for Coal Fly Ash and Raw or Calcined Natural Pozzolan for Use in Concrete.* West Conshohocken, PA: ASTM International.

ASTM Standard A615, 2012. *Standard Specification for Deformed and Plain Carbon-Steel Bars for Concrete Reinforcement.* West Conshohocken, PA: ASTM International.

ASTM Standard C 1017, 2007. *Standard Specification for Chemical Admixtures for Use in Producing Flowing Concrete.* West Conshohocken, PA: ASTM International.

ASTM Standard C109/C109M, 2011b. *Standard Test Method for Compressive Strength of Hydraulic Cement Mortars (Using 2-in. or [50-mm] Cube Specimens).* West Conshohocken, PA: ASTM Interntional.

ASTM Standard C117, 2004. *Standard Test Method for Materials Finer than 75-μm (No. 200) Sieve in Mineral Aggregates by Washing.* West Conshohocken, PA: ASTM International.

ASTM Standard C1202, 2012. *Standard Test Method for Electrical Indication of Concrete's Ability to Resist Chloride Ion Penetration.* West Conshohocken, PA: ASTM International.

ASTM Standard C1260-94, 1994. *Standard Test Method for Potential Alkali Reactivity of Aggregates (Mortar-bar method).* West Conshohocken, PA: ASTM International.

ASTM Standard C136, 2006. *Standard Test Method for Sieve Analysis of Fine and Coarse Aggregates.* West Conshohocken, PA: ASTM International.

ASTM Standard C157/C157M, 2008. *Standard Test Method for Length Change of Hardened Hydraulic-Cement Mortar and Concrete.* West Conshohocken, PA: ASTM International.

ASTM Standard C1585, 2011. *Standard Test Method for Measurement of Rate of Absorption of Water by Hydraulic-Cement Concretes.* West Conshohocken, PA: ASTM International.

ASTM Standard C1611, 2009. *Standard Test Method for Slump Flow of Self-Consolidating Concrete.* West Conshohocken, PA: ASTM International.

ASTM Standard C1679, 2009. *Measuring Hydration Kinetics of Hydraulic Cementitious Mixtures Using Isothermal Calorimetry.* West Conshohocken, PA: ASTM International.

ASTM Standard C403, 2008. *Standard Test Method for Time of Setting of Concrete Mixtures by Penetration Resistance*, West Conshohocken, PA: ASTM International.

ASTM Standard C494, 2011. *Standard Specification for Chemical Admixtures for Concrete.* West Conshohocken, PA: ASTM International.

ASTM Standard C642, 2006. *Standard Test Method for Density, Absorption, and Voids in Hardened Concrete.* West Conshohocken, PA: ASTM International.

ASTM Standard C666/C666M 2003, 2008. *Standard Test Method for Resistance of Concrete to Rapid Freezing and Thawing.* West Conshohocken, PA: ASTM International.

Baalbaki, W., Benmokrane, B., Challal, O. and Aitcin, P., 1991. Influence of Coarse Aggregate on Elastic Properties of High Performance Concrete. *ACI Materials Journal,* 88(5), pp. 499-503.

Bakker, R., 1988. Initiation period. In: P. Schiessl, ed. *Corrosion of Steel in Concrete.* London: Chapman and Hall, pp. 22-55.

Bazant, Z., 1979. Physical Model or Steel Corrosion in Concrete Sea Structures Part Theory Part Application. *Journal of the Structural Division ASCE,* 105(6), pp. 1137-1166.

Beeldens, A. and Vandewalle, L., 2001. *Durability of high strength concrete for highway pavement restoration.*. Vancouver, BC, Canada, CONSEC 01: Third International Conference on Concrete under Severe Conditions, pp. 1230-1238.

Bisaillon, A., Rivest, M. and Malhotra, V., 1994. Performance of High Volume Flyash Concrete In Large Experimental Monoliths. *ACI Materials Journal,* 91(2), pp. 178-187.

Bursi, O. S., and Gramola, G., 1999, Behaviour of Headed Stud Shear Connectors under Low-Cycle High Amplitude Displacements, *Materials and Structures*, 32(218), pp. 290-297.

Caner, A. and Zia, P., 1998. Behaviour and Design of Link Slabs for Jointless Bridge Decks. *Precast/ Prestressed Concrete Instutute Journal*, Issue 43, pp. 68-80.

Cetin, A. and Carrasquillo, R., 1998. High Performance Concrte: Influence of Coarse Aggregates on Mechanical Properties. *ACI Materials Journal,* 95(3), pp. 252-261.

Chang, P., Peng, Y. and Hwang, C., 2001. A Design Consideration for Durability of High-Performance Concrete. *Cement and Concrete Composites,* 23(4-5), pp. 375-380.

Driscoll, G. C., and Slutter, R. G., 1961, Research on Composite Design at Lehigh University, *Proceedings,* National Engineering Conference, AISC, pp. 18-24.

Evardsen, C., 1999. Water Permeability and Autogeneous Healing of Cracks in Concrete. *ACI Material Journal,* 96(4), pp. 448-454.

Federal Highway Administration (FHWA), 1992. *Corossion Detection in Reinforced Concrete Bridge Structures.* Washington, DC: Project 84.

Fischer, G. and Li, V., 2002. Influence of Matrix Ductility on Tension-Stiffening Behaviour of Steel Reinforced Engineered Cementitious Composites (ECC). *ACI Structural Journal,* 99(1), pp. 104-111.

Fischer, G. S. W. and Li, V., 2003. *Design of Engineered Cementitios Composites (ECC) for Processing and Workability Requirement.*. Poland, BMC 7, pp. 29-36.

Gerard, B., Reinhardt, H. and Breysse, D., 1997 . *Measured Transport In Cracked Concrete. Penetration and Permeability of Concrete,* s.l.: RILEM Report 16, Edited by H.W. Reinhardt.

Gilani, A. and Jansson, P., 2004. *Link Slabs for Simply Supported Bridges,* Michigan: Michigan Department of Transportation.

Gilani, A. and Juntunen, D., 2001. *Link Slabs for Simply Supported Bridges: Incorporating Engineered Cementitious Composites,* Michigan: Michigan Department of Transportation.

Glasser, F., 1991. Chemical, Mineralogical, and Microstructural Changes Occuring in Hyrated Slag-Cement Blends. The. *Materials Science of Concrete,* Volume II, pp. 41-81..

Hearn, N., 1999. Effect of Shrinkage and Load-Induced Cracking on Water Permeability of Concrete. *ACI Materials Journal,* 96(2), pp. 234-241.

Hossain, K., 2003. Blended Cement Using Volcanic Ash and Pumice. *Cement and Concrete Research- An International Journal,* 33(10), pp. 1601-1605.

Hossain, K., 2003. Chloride Diffusivity of Volcanic Ash Blended Hardened Cement Paste. *Advances in Cement Research,* 15(2), pp. 83-90.

Hossain, K., 2003. Effect of Volcanic Pumice on The Corrosion Resistance and Chloride Diffusivity of Blended Cement Mortars. *Journal of Advanced Concrete Technology,* 1(1), pp. 54-62.

Hossain, K., 2004. Properties of Volcanic Pumice Based Cement and Lightweight Concrete. *Cement and Concrete Research,* 34(2), pp. 283-291.

Hossain, K., 2005. Chloride Induced Corrosion of Reinforcement in Volcanic Ash and Pumice Based Blended Concrete. *Cement, Concrete and Composite,* 27(3), pp. 381-390.

Hossain, K., 2005. Correlations Between Porosity, Chloride Diffusivity and Electrical Resistivity in Volcanic Pumice-based Blended Cement Pastes. *Advances in Cement Research,* 17(1), pp. 29-37.

Hossain, K., 2005. Volcanic Ash and Pumice as Cement Additives: Pozzolanic, Alkali-silica Reaction and Autoclave Expansion Characteristics. *Cement and Concrete Research,* 35(6), pp. 1141-1144.

Hossain, K., 2012. Lightweight Concrete with Volcanic Materials. *Construction Materials Journal, ICE,* 165(CM2), pp. 111-120.

Hossain, K. and Lachemi, M., 2004. Corrosion Resistance and Chloride Diffusivity of Volcanic Ash Blended Cement Mortar. *Cement and Concrete Research,* 34(4), pp. 695-702.

Hossain, K., Mak, C. and Ametrano, D., 2012. GFRP Reinforced UHPC Composites for Sustainable Bridge Construction. *Canadian Civil Engineer,* 29(1), pp. 12-15.

Hussian, S. E. and Rasheeduzzafar, M., 1994. Corrosion Resistance Performance of Fly Ash Blended Cement Concrete. *ACI Materials Journal,* May- June, 91(3), pp. 264-272.

Hwang, C., Liu, J., Lee, L. and Lin, F., 1996. Densified Mixture Design Algorithm and Early Properties of High Performance Concrete.. *Chinese Institute of Civil and Hydraulic Engineering,* 8(2), pp. 217-229.

Inaguma, H., Seki, M., Suka, K. and Rokugo, K., 2005. *Experimental study on crack-bridging ability of ECC for repair under train loading.*. Honolulu, Hawaii, USA., Proc. of Int'l Workshop on HPFRCC in Structural Applications, pp. 499-508.

Kanda, T., Saito, T. and Sakata, N., 2003. Tensile and Anti-Spalling Properties of Direct Sprayed ECC. *Advanced Concrete Technology,* 1(3), pp. 269-282.

Karahan, O, Hossain, K.M.A., Ozbay, E., Lachemi, M., Sancak, E., 2012. Effect of Metakaolin Content on The Properties Self-consolidating Lightweight Concrete. *Construction and Building Materials,* 31(6), pp. 320-325.

Kim, J.-K., Kim, J.-S., Ha, G. J. and Kim, Y. Y., 2007. Tensile and Fiber Dispersion Performance of ECC (engineered cementitious composites) Produced with Ground Granulated Blast Furnace Slag. *Cement and Concrete Research,* 37(7), p. 1096–1105..

Kim, Y., Fischer, G. and Li, V., 2004. Performance of Bridge Deck Link Slabs Designed with Ductile ECC. *ACI Structural Journal,* 1(6), pp. 792-801.

Kim, Y.Y., Kim, J.S., Kim, H.S., Kim, J.K. and Ha, G.J.,2004. *Uniaxial Tensile Behaviour of High Ductile Fiber Reinforced Mortar Designed with Ground Granulated Blast Furnace Slag.*. s.l., KSCE Conference, pp. 546-551.

Kim, Y., Kong, H. and Li, V., 2003. Design of Engineered Cementitious Composite (ECC) Suitable For Wet-Mix Shotcreting. *ACI Materials Journal,* 100(6), pp. 511-518.

Kong, H., Bike, S. and Li, V., 2003b. Constitutive Rheological Control to Develop a Self-Consolidating Engineered Cementitious Composite Reinforced with Hydrophilic Poly(vinyl alcohol) Fibers. *Journal of Cement and Concrete Composites*, 25(3), pp. 333-341.

Kong, H. J., Bike, S. and Li, V. C., 2003a. Development of a Self-Consolidating Engineered Cementitious Composite Employing Electrosteric Dispersion/Stabilization. 25(3), pp. 301-309.

Kosmatka, S. and Panarese, W., 1988. *Design and control of concrete mixtures.* 13th ed. Skokie, IL: Portland Cement Association,205.

Kunieda, M. and Rokugo, K., 2006. Recent Progress on HPFRCC In Japan. *Journal of Advanced Concrete Technology*, 40(1), pp. 19-33.

Kurdowski, W. and Nocun-Wczelik, W., 1983. The Tricalcium Silicate Hydration in The Presence of Active Silica. *Cement Concrete Research*, 13(3), pp. 341-348.

Kuroda, M., Watanabe, T. and N., T., 2000. Increase of bond strength at interfacial transition zone by the use of fly ash. 30(2), pp. 253-258.

Lepech, M.D. and Li, V., 2006. Long Term Durability Performance of Engineered Cementitious Composites. *Journal of Restoration of Buildings and Monuments,* 12(2), pp. 119-132.

Lepech, M. D. and Li, V. C., 2009. Application of ECC For Bridge Deck Link Slabs. *RILEM Journal of Materials and Structures,* 42(9), pp. 1185-1195.

Lepech, M. D., Li, V. C., Robertson, R. E. and Keoleian, G. A., 2008. Design of Green Engineered Cementitious Composites for Improved Sustainability. *ACI Materials Journal,* 105(6), pp. 567-575.

Lepech, M. and Li, V., 2005a. *Water Permeability of Cracked Cementitious Composites.* Turin, Italy, ICF 11, pp. CD-ROM.

Lepech, M. and Li, V., 2005b. *Durability and Long Term Performance of Engineered Cementitious Composites.* Honolulu, Hawaii, In Proceedings of International RILEM Workshop on HPFRCC in Structural Applications, pp. 165-174..

Lepech, M. and Li, V., 2008. Large Scale Processing of Engineered Cementitious Composites. *ACI Materials Journal,*, 105(4), pp. 358-365.

Li, V.C. and Leung C.K.Y., 1992. Theory of steady state and multiple cracking of random discontinuous fiber reinforced brittle matrix composites.. *ASCE Journal of Engineering Mechanics,* 118(11), pp. 2246-2264.

Li, M., Sahmaran, M. and Li, V., 2007 . *Effect of Cracking and Healing on Durability of Engineered Cementitious Composites under Marine Environment.* Stuttgart,Germany, HPFRCC 5 - High Performance Fiber Reinforced Cement Composites, pp. 313-322.

Lin, Z., Kanda, T. and Li, V., 1999. On Interface Property Characterization and Performance of Fiber Reinforced Cementitious Composites. *Concrete Science and Engineering, RILEM,,* V(I), pp. 173- 184.

Li, S. and Roy, D. M., 1986. Investigation of Relations Between Porosity, Pore Structure and Chloride Diffusion of Fly Ash and Blended Cements. 16(5), pp. 749-759.

Li, V., 1997. Engineered Cementitious Composites Tailored Composites Through Micromechanical Modeling in Fiber Reinforced Concrete: Present and the Future. *Canadian Society for Civil Engineering,* pp. 64-97.

Li, V., 2003. on Engineered Cementitious Composites (ECC) - A Review of The Material and Its Applications. *Journal of Advanced Concrete Technology,* 1(3), pp. 215-230.

Li, V. C., 1998. Engineered Cementitious Composites for Structural Applications. 10(2), pp. 66-69.

Li, V. C., 2002. *Reflections on the Research and Development of Engineered Cementitious Composites (ECC).* Takayama, Japan, s.n., pp. 1-21.

Li, V. C., Wang, S. and Wu, C., 2001. Tensile Strain Hardening Behaviour of PVAECC. *ACI Material Journal,* 98(6), pp. 483-492.

Li, V. and Fischer, G., 2002. *Reinforced ECC - An Evolution from Materials to Structures.* Osaka, Japan, Proceedings of the First FIB Congress, 105-122.

Li, V.C., Fischer, G., Kim, Y.Y., Lepech, M., Qian, S., Weimann, M., and Wang, S., 2003. *Durable Link Slabs For Jointless Bridge Decks Based on Strain-Hardening Cementitious Composites,* : Report for Michigan Department of Transportation RC- 1438.

Li, V.C., Horikoshi, T., Ogawa, A., Torigoe, S., and Saito, T.,2004. Micromechanics-based Durability Study of Polyvinyl Alcohol Engineered Cementitious Composite (PVA-ECC). *ACI Materials Journal,* 101(3), pp. 242-248.

Li, V. and Kanda, T., 1998. Engineered Cementitious Composites for Structural Applications. *ASCE Journal of Materials in Civil Engineering,* 10(2), pp. 66-69.

Li, V. and Lepech, M., 2004. *Crack Resistant Concrete Material for Transportation Construction.* Washington, DC, In TRB 83rd Annual Meeting,Compendium of Papers CD ROM.

Li, V., Lepech, M. and Li, M., 2005. *Field Demonstration of Durable Link Slabs for Jointless Bridge Decks Based on Strain-Hardening Cementitious Composites*, s.l.: Michigan DOT report.

Li, V., Mishra, D. and Wu, H., 1995. Matrix Design for Pseudo Strain-Hardening Fiber Reinforced Cementitious Composites.. *RILEM Journal of Materials and Structures,* 28(183), pp. 586-595.

Li, V. and Stang, H., 2004. *Elevating FRC Material Ductility To Infrastructure Durability.* Varenna, Lake Como, Italy, Proceedings of BEFIB, pp. 171-186.

Li, V.C., Wu, C., Wang, S., Ogawa, A., and Saito., T., 2002. Interface Tailoring for Strain-Hardening PVA-ECC. *ACI Materials Journal,* 99(5), pp. 463-472.

Manning, D., 1996. Corrosion Performance of Epoxy-Coated Reinforcing Steel: North American Experience. *Construction and Building Materials,* 10(5), pp. 349-365.

Marshall, D. and Cox, B., 1988. A J-Integral Method For Calculating Steady-State Matrix Cracking Stresses In Composites. *Mechanics of Materials,* 7(2), pp. 127-133.

Martys, N. and Ferraris, C., 1997. Capillary Transport In Mortars and Concrete. *Cement and Concrete Research,* 27(5), pp. 747-760.

Maruta, M., Kanda, T., Nagai, S. and Yamamoto, Y., 2005. New high-rise RC Structure Using Pre-Cast ECC Coupling Beam. *Concrete Journal,* 43(11), pp. 18-26.

Maslehuddin, M., Saricimen, H. and Al-Mani, A., 1987. Effect of Fly Ash Addition on The Corrosion Resisting Characteristics of Concrete. *ACI Materials Journal,* 84(1), pp. 42-50.

Mehta, P., 1986. *Concrete: Structure, Properties, and Materials.* Englewood Cliffs New Jersey: Prentice-Hall..

Mehta, P. and Monteiro, P., 2006. *Concrete: Structure, Properties and Materials.* 3rd Edition ed. New York: McGraw Hill.

Michigan Department of Transportation, 2001. *Michigan Test Method 111 -Determining an Aggregate Wear Index (AWI) By Wear Track Polishing Tests,* Lansing, Michigan.: Michigan Department of Transportation.

Mihashi, H. and De Leite, J., 2004. State-of-the-Art Report on Control of Cracking in Early Age Concrete. *Advanced Concrete Technology,* 2(2), pp. 141-154.

Miyazato, S. and Hiraishi, Y., 2005. *Transport Properties and Steel Corrosion In Ductile Fiber Reinforced Cement Composites*. Turin, Italy, Proceedings of the Eleventh International Conference on Fracture, pp. 20-25.

Mora, J., Aguado, A. and Gettu, R., 2003. The Influence of Shrinkage Reducing Admixtures on Plastic Shrinkage.. *Materiales de Construccion*, 53(271-272), pp. 71-80.

Moranville-Regourd, M. ,. L., 1998. *Cements Made From Blastfurnace Slag, Lea`s Chemistry of Cement and Concrete*. 4th ed. Arnold, London: P. C. Hewlett Ed.,663-674..

Neville, A., 1996. *Properties of Concrete,*. 4th Edition ed. s.l.:John Wiley and Sons, New York.

Oehlers, D. J., and Foley, L., 1985, The Fatigue Strength of Stud Shear Connections in Composite Beams, *Proceedings of the Institute of Civil Engineering*, London, England, Part 2, 79, pp. 349-364.

Oh, B., Cha, S., Jang, B. and Jang, S., 2002. Development of High-Performance Concrete Having High Resistance To Chloride Penetration.. *Nuclear Engineering and Design*, 212(1-3), pp. 221-231.

Ollgaard, J. G.; Slutter, R. G.; and Fisher, J. W., 1971, Shear Strength of Stud Connectors in Lightweight and Normal-Weight Concrete, *AISC Engineering Journal*, pp. 55-64.

Ozkan, S. and Mehmet, A. T., 2009. Compressive Strength and Rapid Chloride Permeability of Concretes With Ground Fly Ash and Slag. *Journals of Materials in Civil Engineering*, 21(9).

Pigeon, M., Azzabi, M. and Pleau, R., 1996. Can Microfibers Prevent Frost Damage?. *Cement and Concrete Research*, 26(8), pp. 1163-1170.

Qian, S., Lepech, M. D., Kim, Y. Y. and Li, V. C., 2009. Introduction of Transition Zone Design for Bridge Deck Link Slabs Using Ductile Concrete. *ACI Stuctural Journal* , 106(1), pp. 96-105.

Qian, S. and Li, V., 2007. Simplified Inverse Method for Determining the Tensile Strain Capacity of Strain Hardening Cementitious Composites. *Advanced Concrete Technology*, 5(2), pp. 235-246.

Qian, S. and Li, V., 2008. Simplified Inverse Method For Determining The Tensile Properties of Strain Hardening Cementitious Composites. *Advanced Concrete Technology*, 6(2), pp. 353-363.

Qian, S. and Li, V. C., 2006. Influence of Concrete Material Ductility on Shear Response of STud Connections. 103(1), pp. 60-66.

Reinhardt, H. and Jooss, M., 2003. Permeability and Self-Healing of Cracked Concrete as a Function of Temprature and Crack Width. *Cement and Concrete Research*, 33(7), pp. 981-985.

Rokugo, K., Kunieda, M. and Lim, S., 2005. *Patching Repair With ECC on Cracked Concrete Surface.*, CONMAT 5.

Roy, D., 1992. *The Effect of Blast Furnace Slag and Related Materials on the Hydration and Durability of Concrete.* Detroit, Michigan,, G. M. Idorn International Symposium, ACI SP–131, pp. 195-208.

Sagues, A., Powers, R. and Locke, C., 1994. *Corrosion Processes and Field Performance of Epoxy-Coated Reinforcing Steel In Marine Structures.* Houston, TX: Corossion 94 .

Sahmaran, M. and Li, V., 2007. De-Icing Salt Scaling Resistance of Mechanically Loaded Engineered Cementitious Composites. *Cement and Concrete Research,* Issue 37, pp. 1035-1046.

Sahmaran, M. and Li, V., 2009b. Influence of Microcracking on Water Absorption and Sorptivity of ECC. 42(5), pp. 593-603.

Sahmaran, M. and Li, V. C., 2009a. Durability Properties of Micro-Cracked ECC Containing High Volume Flyash. *Cement and Concrete Researh,* 39(11), pp. 1033-1043.

Sahmaran, M., Li, V. and Li, M., 2007. Transport Properties of Engineered Cementitious Composites under Chloride Exposure. 104(6), pp. 604-611.

Sahmaran, M., Lachemi, M., Hossain, K. M. and Li, V., 2009. Influence of Aggregate Type and Size on Ductility and Mechanical Properties of Engineered Cementitious Composites. *ACI Material Journal,* May-June, 106(3), pp. 308-316.

Sahmaran, M. and Li, V., 2008. Durability of mechanically loaded Engineered Cementitious Composites under high alkaline environment. *Cement and Concrete Composites,* 30(2), pp. 72-81.

Sahmaran, M., Li, V. and Andrade, C., 2008. Corrosion Resistance Performance of Steel-Reinforced Engineered Cementitious Composite Beams. *ACI Material Journal,* 105(3), pp. 243-250.

Sahmaran, M. and Li, V. C., 2010. Engineered Cementitious Composites Can Composites Be Accepted as Crack-Free Concrete?. *Journal of the Transportation Research Board,* No.2164, pp. 1-8.

Sahmaran, M., Yaman, I. O. and Tokyay, M., 2009. Transport and Mechanical Properties of Self Consolidating Concrete With High Volume Flyash. *Cement and Concrete Composites,* 31(2), pp. 99-106.

Sakata, K., Kanda, T. and Hiraishi, M., 2004. Application of Direct Sprayed ECC For Retrofitting Dam Structure Surface-Application For Mitaka-Dam. *Japan Concrete Institute Concrete Journal,* 42(5), pp. 135-139.

SEAOC, 1995. *Vision 2000: A Framework for Performance Based Engineering of Builidngs.* Sacramento,CA, Structural Engineers Association of California.

Sengul, O., Tasdemir, C. and Tasdemir, M., 2002. Influence of Aggregate Type on Mechanical Behaviour of Normal and High Strength Concretes. *ACI materials journal,* 99(6), pp. 528-533.

Smith, K. M., Schokker, A. J. and Tikalsky, P. J., 2004. Performance of Supplementary Cementitious Materials in Concrete Resistivity and CorrosionMonitoring Evaluations. *ACI Materials Journal,* Sept.-Oct., 101(5), pp. 385-390.

Stang, H. a. L. V., 1999. Extrusion of ECC-material. In Proc. of High Performance Fiber Reinforced Cement Composites 3 (HPFRCC 3). pp. 203-212.

Stark, J. and Ludwig, H., 1997. Influence of Water Quality on the Frost Resistance of Concrete. In: J. Marchand, M. Pigeon and S. M., eds. *Freeze-Thaw Durability of Concrete.* London: E and FN Spon, pp. 157-164.

Sun, W., Zhang, Y. S., Liu, S. F. and Zhang, Y. M., 2004. The Influence of Mineral Admixtures on Resistance to Corrosion of Steel. *Journal of Cement and Concrete Research,* 34(10), pp. 1781-1785.

Suthiwarapirak, P., Matsumoto, T. and Kanda, T., 2002. Flexural fatigue failure characteristics of an Engineered Cementitious Composite and Polymer Cement Mortars.. *Journal of Materials, Conc. Struc. Pavements,* 718(57), pp. 121-134.

Taylor, H., 1997. *Cement Chemistry, Second Edition. Thomas Telford.* 2nd ed. London: Thomas Telford Publishing.

Tsivilis, S., Tsantilas, J., Kakali, G., Chaniotakis, E. and Sakellariou, A., 2003. The Permeability of Portland Limestone Cement Concrete. In: s.l.:Cement and Concrete Research, pp. 1465-1471.

Tuutti, K., 1982. Corrosion of Steel in Concrete. p. 159.

Uchikawa, H. and Uchida, S., 1980. *Influence of Pozzolans on The Hydration of C3A.* Paris, Seventh International Congress on the Chemistry of Cement, pp. IV-23–IV-29.

Viest, I. M., 1956a, Test of Stud Shear Connectors, Parts I, II, III and IV, Engineering, Test Data, Nelson Stud Welding, Lorain, Ohio, 32 pp.

Viest, I. M., 1956b, Investigation of Stud Shear Connectors for Composite Concrete and Steel T-Beams. *ACI Journal Proceedings* 53(8), pp. 875-891.

Viest, I. M., 1960, Review of Research on Composite Steel-Concrete Beams, *Journal of the Structural Division,* ASCE, 86(ST6), pp. 1-21.

Wang, K., Janen, D., Shah, S. and karr, A., 1997. Permeability Study of Cracked Concrete. *Cement and Concrete Research,* 27(3), pp. 381-393.

Wang, K., Jansen, D. and Shah, S., 1997. Permeability Study of Cracked Concrete. 27(3), pp. 381-393.

Wang, S. and Li, V., 2004. *Tailoring of Pre-Existing Flaws In ECC Matrix For Saturated Strain Hardening.* Vail, Colorado, USA, s.n., p. 1005–1012..

Wang, S. and Li, V., 2006. High-Early-Strength Engineered Cementitious Composites. *ACI Materials Journal,* 103(2), pp. 97-105.

Wang, S. and Li, V. C., 2007. Engineered Cementitious Composites with High-Volume Fly Ash. *ACI materials journal,* May-June, 104(3), pp. 233-241.

Weimann, M. and Li, V., 2003. Hygral Behaviour of Engineered Cementitious Composites (ECC).. *International Journal for Restoration of Buildings and Monuments, 9, 513-534.,* 9(5), pp. 513-534.

Weiss, W. and Shah, S., 2002. Restrained Shrinkage Cracking: The Role of Shrinkage Reducing Admixtures and Specimen Geometry. *Rilem Journal of Materials and Structures,* 35(246), pp. 85-91.

Wikipedia, 2007. *wikipedia.* [Online] Available at: http://en.wikipedia.org/wiki/Concrete

Wittmann, F., 2002. Crack Formation and Fracture Energy of Normal and High Strength Concrete. *Sadhana,* 27(4), pp. 413-423.

Wolde-Tinsae, A. and Klinger, J., 1987. *Integral Bridge Design and Construction, Report FHWA/MD-87/04,* : Maryland Department of Transportation.

Yang, E. and Li, V., 2006. *A Micromechanical Model for Fiber Cement Optimization and Component Tailoring.* San Paulo, Brazil, Proceedings of 10th International Inorganic-Bonded Fiber Composites Conference, pp. CD-ROM.

Yang, E., Yang, Y. and Li, V., 2007. Use of High Volumes of Fly Ash To Improve ECC Mechanical Properties and Material Greenness. *ACI Materials Journal,* 104(6), pp. 620-628.

Yang, Y., Lepech, M., Yang, E. and Li, V., 2009. Autogeneous Healing of Engineering Cementitious Composites under Wet-Dry Cycles. 39(5), pp. 382-390.

Zhang, J. and Li, V., 2002. Monotonic and Fatigue Performance In Bending of Fiber Reinforced Engineered Cementitious Composite In Overlay System. *Cement and Concrete Research,* 32(3), pp. 415-423.

Zhang, M., 1995. Microstructure, Crack Propogation and Mechanical Properties of Cement Pastes Containing High Volumes of Flyashes. *Cement and concrete research,* 25(6), pp. 1165-1178.

Zhang, M. H., Bilodeau, A., Malholtra, V. M., Kim, K. S., Kim, J. C., 1999. Concrete Incorporating Supplementary Cementing Materials: Effect on Compressive Strength and Resistance To Chloride Ion Penetration. *ACI Materials Journal,* 96(2), p. 181–189.

Zhou, J., Qian, S., Beltran, M.G.M., Ye, G., VanBreugel, K., Li, V.C., 2009. Development of Engineered Cementitious Composites with Limestone Powder and Blast Furnance Slag. *Rilem Journal of Materials and Structures,* 46(3), pp. 803-814.

Zia, P., Caner, A. and El-Safte, A., 1995. Jointless bridge decks Research project 23241-94-4.. *Center for Transportation Engineering Studies, North Carolina State,* pp. 1-117.